LIGHTWEIGHT MECHANICAL METAMATERIALS BASED ON HOLLOW LATTICES AND TRIPLY PERIODIC MINIMAL SURFACES

by

Biwei Deng

A Dissertation

Submitted to the Faculty of Purdue University

In Partial Fulfillment of the Requirements for the degree of

Doctor of Philosophy

School of Industrial Engineering

West Lafayette, Indiana

December 2019

THE PURDUE UNIVERSITY GRADUATE SCHOOL
STATEMENT OF COMMITTEE APPROVAL

Dr. Gary J. Cheng, Chair
School of Industrial Engineering

Dr. Kejie Zhao
School of Mechanical Engineering

Dr. Wenbin Yu
School of Aeronautics and Astronautics

Dr. Ramses Martinez
School of Industrial Engineering

Approved by:

Dr. Abhijit Deshmukh
Head of the Graduate Program

To my beloved family

ACKNOWLEDGMENTS

Throughout the working and writing of this dissertation I have received many kind supports from many amazing people. I would first give my deepest gratitude to my PhD advisor, Prof. Gary J. Cheng. Without the strong support, ample trust and warm encouragement from him, this dissertation could not be possible. I have benefited from his guidance and expertise in multiple research frontiers. These knowledges are invaluable for me in the past, present and future.

I would also thank my committee members Prof. Kejie Zhao, Prof. Wenbin Yu and Prof. Ramses Martinez for their kind supports. Thank you for your valuable inputs which eventually made this work possible. I would also thank Prof. Yongfeng Lu, Dr. Sabayasachi Ganguli and Prof. Weinong Chen for providing the experimental tools for my work.

I would like to thank my colleagues and friends Dr. Rong Xu, Dr. Yaowu Hu, Dr. Shengyu Jin, Jin Xu, Xingtao Liu, Sen Xiang, Licong An, Maithilee Motlag and Danilo de Camargo Branco for their generous discussion over my research topics and help in the lab.

Lastly, I want to thank my parents. If it is not for their raising and teaching for years, I could never reach the point where I am right now. I am forever grateful that I have my family supporting me unconditionally.

TABLE OF CONTENTS

LIST OF TABLES

LIST OF FIGURES

ABSTRACT

Author: Deng, Biwei. PhD
Institution: Purdue University
Degree Received: December 2019
Title: Lightweight Mechanical Metamaterials Based on Hollow Lattices and Triply Periodic Minimal Surfaces.
Committee Chair: Gary J. Cheng

Lightweight mechanical metamaterials with exception specific stiffness and strength are useful in many applications, such as transportation, aerospace, architectures and etc. These materials show great potential in mechanical tasks where weight of the material is restrained due to economy or energy reasons. To achieve both the lightweight and the high specific mechanical properties, the metamaterials are often in form of periodic cellular structures with well-designed unit cells. The strategies in designing and improving such cellular structures become the key in the studies of such mechanical metamaterials. In this work, we use both experimental and numerical approaches while probing three types of mechanical metamaterials: i) composite bending dominated hollow lattices (HLs); ii) triply periodic minimal surfaces (TPMSs) and extended TPMSs (eTPMSs); iii) corrugated TPMSs. We have demonstrated a few strategies in designing and improving the specific stiffness or strength via these examples of mechanical metamaterials. Using carbon/ceramic composite in the bending dominated HLs, we prove that using the composite layered material against the single layer ceramic is effective in improving the specific mechanical performances of the mechanical metamaterials. Next, while studying the nature of TPMS, we discover that under isotropic deformation TPMSs are stretch dominated with no stress concentrations within the shell structure. They also have an optimal specific bulk modulus approaching the H-S upper bound. Furthermore, we establish a strategy to smoothly connect the zero-mean-curvature surfaces in TPMSs with the extension of zero-Gaussion-curvature surfaces, forming new ‘eTPMSs”. These new shellular structures trade off its isotropy and have improved specific Young’s modulus along their stiffest orientation compared to their TPMS base structures. Lastly, we introduce corrugated sub-structures to existing TPMSs to improve their mechanical properties, such as Young’s modulus, yield strength and failure strength in compression. It is found that the corrugated sub-structure can effectively suppress the local bending behavior and redirect crack propagation while such structures were under uniaxial compression.

1. INTRODUCTION

1.1 Motivation

Metamaterials are artificial materials that exhibit properties which are not found in natural materials (Kshetrimayum 2004). Such unique properties of metamaterials are not directly originated from the intrinsic properties of the materials but are realized by the spatial arrangement of the materials. Thus, the actual properties of metamaterials are dominated by the artificial spatial structure. The idea of metamaterials has enabled many research fields on engineering the structures, either in nanoscale or in microscale, towards desired properties. The concept of metamaterials was first raised in optical applications (Smith, Pendry, and Wiltshire 2004). The earliest optical metamaterial was able to refract light in unnatural directions. In the 1980s, it was discovered that periodically arranged structures could be designed to respond to mechanical forces in unnatural manners (Lakes 1987). Such mechanical metamaterials are called 'auxetic materials' (K. E. Evans 1991). They have negative Poisson's ratio, which means that when they are stretched in one direction, they are also expanding along other directions that is perpendicular to the stretched direction. From then, mechanical metamaterials of many kinds have been theoretically invented and experimentally validated. A few examples aside from auxetic materials are acoustic metamaterials of many kinds (Fang et al. 2006; J. Li et al. 2009; Liu et al. 2000; Zigoneanu, Popa, and Cummer 2014), in which the acoustic waves can be manipulated; multi-stable materials(Norman, Seffen, and Guest 2008; Shan et al. 2015; Silverberg et al. 2014), which are particularly useful in deployable devices(Zhai, Wang, and Jiang 2018); pentamode lattices(Milton and Cherkaev 1995), which can be used for acoustic cloaking(T. Bückmann et al. 2014), and foldable origami structures(T. A. Evans et al. 2015; Schenk and Guest 2013). The idea of altering spatial design of existing materials to realize novel, tunable mechanical properties has been widely recognized and exercised.

Among the many types of mechanical metamaterials, ones with low mass density yet high stiffness or strength have attracted interest from many researchers in recent years (Zadpoor 2016). Such mechanical metamaterials with unusual specific stiffness or strength can potentially replace existing light-weight materials in many mechanical parts. The exceptional mechanical property of these metamaterials come from their interior cellular structures by design. Unlike light-weight

foams, which are consisted of random interior structures, the state-of-the-art mechanical metamaterials are often made up with periodic structures in three dimensions. On the mechanical metamaterials with low density and high stiffness or strength, the grand challenge is to push the specific properties to the extreme. Despite that the records are pushed higher and higher, it is still unknown if the upper limit is reached or not. As the race goes on, the understanding in designing these mechanical metamaterials is rapidly promoted.

1.2 Scope of Study

This thesis presents a series of works concerning low density mechanical metamaterials with exceptional specific stiffness and strength. The range of mechanical metamaterial designs stretches from hollow lattices (HLs) to various triply periodic minimal surfaces (TPMSs) and their derivatives. The key insights here are i) understanding why structures like HLs and TPMSs exhibit high specific stiffness and strength and ii) what type of further improvements can be made on the basis of the current designs.

1.2.1 HLs and TPMSs

HLs are structures that are constructed based on lattices of various crystallographic symmetries. Each point in a lattice represent a node in a HL structure, while each nearest pair of points is bridged with a cylindrical strut. All nodes and struts are hollow, and the inner space is interconnected in a HL. A few examples of HLs are the simple cubic (SC) HL, diamond HL, body-centered cubic (BCC) HL, face-centered cubic (FCC) HL and hexagonal closest packed (HCP) HL.

TPMSs are triply periodic surfaces which has zero mean curvature at every point on the surface. They are originated from the study of a soap film (Karcher and Polthier 1996). The force balance within the soap film requires zero mean curvature, given that the tension in a soap film is equal everywhere. It is worth to point out that unlike its name, a TPMS is not necessarily globally minimal given a fixed boundary. The mathematical definition of a minimal surface only requires the local zero mean curvature. A few examples of TPMSs are Schwarz' P (SP) surface, Schwarz' D (SD) surface, gyroid, Scheon's I-graph-Wrapped Package graph (IWP) surface and Scheon's F-graph-Rhombic dodecahedra graph (FRD) surface.

Figure 1.1 Local surface elements of a hill, basin or saddle. Surfaces with mean zero curvature are saddles if not flat planes.

Knowing the geometries of various HLs and TPMSs, we constructed the digital files of these structures and probed them with both numerical and experimental approaches. The numerical modelling of the mechanical metamaterials not only gives predictions of the mechanical behaviors, but also provides detailed data such as interior strain distribution, which can be useful is often difficult to obtain through experimental methods. The experimental testing of the mechanical metamaterials validates the numerical results. At the same time, the manufacturability of the mechanical metamaterials could also be evaluated while experimental samples are fabricated.

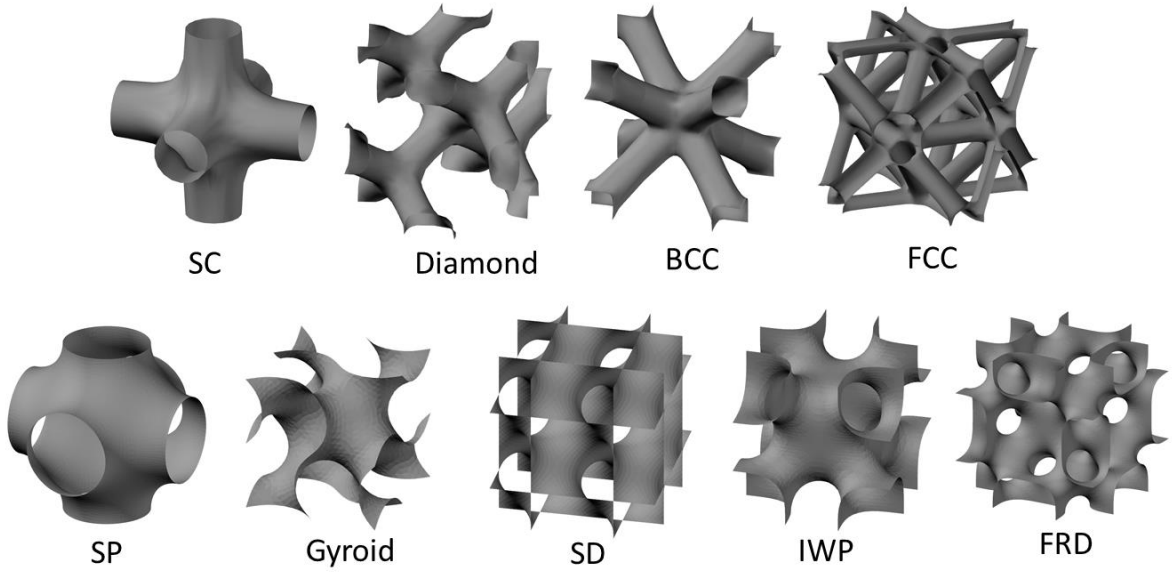

Figure 1.2 Unit cells of different types of HLs and TPMSs. First row: HLs; second row: TPMSs.

1.2.2 Measures for Improved Mechanical Performances

The most straight forward way to improve the mechanical performances of a mechanical metamaterial is to substitute the base material with a better one. Current base materials choices are metals, carbon, ceramics, thermoplastics, photo resins and elastomers. These materials have various distinct properties, such as ductile property, brittle property or hyperelasticity. Researchers not only choose from one of these candidate materials to realize desired properties, but also combine two or more materials to fabricate composites (Munch et al. 2008). These composites could exhibit a new performance, which neither component could reach alone.

On the other hand, it is also an extensively studied approach to seek for mechanical performance improvement in mechanical metamaterials from the angle of structure design. For example, one can modify or combine existing structure designs, like lattices, to realize certain properties, such as perfect isotropy or large elastic limit. These approaches can be similar to the process of topology optimization except that the periodicity of the structure is usually remained. Although these methods are effective, they are largely limited by the existing structure designs. Another way of creating new mechanical metamaterials is inventing new structures of distinct features. In 1970s, Schoen discovered new TPMSs, among which gyroid is a well-known example (Schoen 2012). The TPMS family has been enriched significantly since his discovery. These structures are now used as one of the most promising structures to reach the theoretical limit for stiffness.

1.3 Organization

This dissertation presents the research in fabricating the state-of-the-art mechanical metamaterials with exceptional mechanical properties and in understanding the relationship between the mechanical performances and the design factors. Chapter 2 is a literature review section which highlights the recent theoretical and experimental efforts on the topic of low density, high stiffness and strength mechanical metamaterials. Chapter 3 describes a type of novel mechanical metamaterials in form of composite bending-dominated HLs. The base materials are ceramic (Al_2O_3) and carbon. It is discovered that despite the bending-dominated lattice design, the metamaterial is still showing high stiffness and strength profiles. Chapter 4 consists of a fundamental study of the elastic behavior of TPMSs via numerical methods and associated

experimental validation. Five types of commonly-used TPMSs are investigated regarding the bulk modulus, Young's modulus and elastic an-isotropy. HLs of identical symmetries are also measured as references. A mixing strategy of zero-curvature surfaces based on TPMSs is proposed for improvement of Young's modulus along the stiffest orientation. Chapter 5 demonstrates a structural strategy to improve the specific stiffness and strength of mechanical metamaterials with TPMS geometries. To be more specific, shellular structures of TPMS are enriched with corrugated sub-structures, which significantly enhanced the mechanical properties of the metamaterials. Chapter 6 summarizes the work in this dissertation and sketches a few potentially promising researches directions in the future.

2. BACKGROUND REVIEW

2.1 Mechanical Metamaterials

The study of mechanical metamaterials with low density and high specific stiffness and strength has been taken by both theoretical and experimental approaches. Comprehensive understandings of the mechanical metamaterials can be obtained by numerical simulations or experimental measurements of a finite sample constructed with a number of unit cells. This is practical thanks to the periodic nature of the mechanical metamaterials. Aside from the numerical and experimental analysis, a theoretical guideline is in need before any structure is proposed.

The cases of cellular materials are often seen in nature (Wegst et al. 2015). Some of them have evolved over several million years into their optimized forms while surviving the environment. The interior structures in plant stems (Speck and Burgert 2011), leaves (Kobayashi, Kresling, and Vincent 1998), bones (Launey, Buehler, and Ritchie 2010), nacres (Tang et al. 2003), feathers (Sullivan et al. 2017) and many other nature materials have served as the guidelines for artificial materials. These structures have been summarized and categorized, while analytical models (Gibson 2005) are used in explanations and predictions of their mechanical behaviors.

2.2 Scaling Laws by Mass Density

Scaling laws of mechanical metamaterials describes the correlation between certain mechanical properties and the effective mass densities of materials. Typically, mechanical properties such as the elastic modulus and the yield strength, increase as the density of a cellular material goes up, or in another word, as the porosity of a material goes down. Meanwhile, as the interior structure of a material changes, the correlation between the mechanical property and the mass density could vary.

The scaling laws of cellular materials, such as foams or lattices, were first generalized and summarized by Ashby (Ashby 2006). Based on Maxwell's stability criterion (Maxwell 1864), lattices can be divided into two categories: bending-dominated and stretch-dominated. Simply speaking, lattices are constructed by connected nodes and struts. When a structure is rigidly or overly connected, this structure is stretch-dominated; otherwise if a structure is less connected, this

structure is bending-dominated. A simple beam model was used to determine the scaling laws of lattice materials, and resulted as follows for the modulus E:

$$\frac{E}{E_s} \propto \left(\frac{\rho}{\rho_s}\right)^2 \text{ (Bending)}$$

$$\frac{E}{E_s} \propto \frac{\rho}{\rho_s} \text{ (Stretching)}$$

Similarly, the scaling laws for the strength σ were as follows:

$$\frac{\sigma}{\sigma_s} \propto \left(\frac{\rho}{\rho_s}\right)^{3/2} \text{ (Bending)}$$

$$\frac{\sigma}{\sigma_s} \propto \frac{\rho}{\rho_s} \text{ (Stretching)}$$

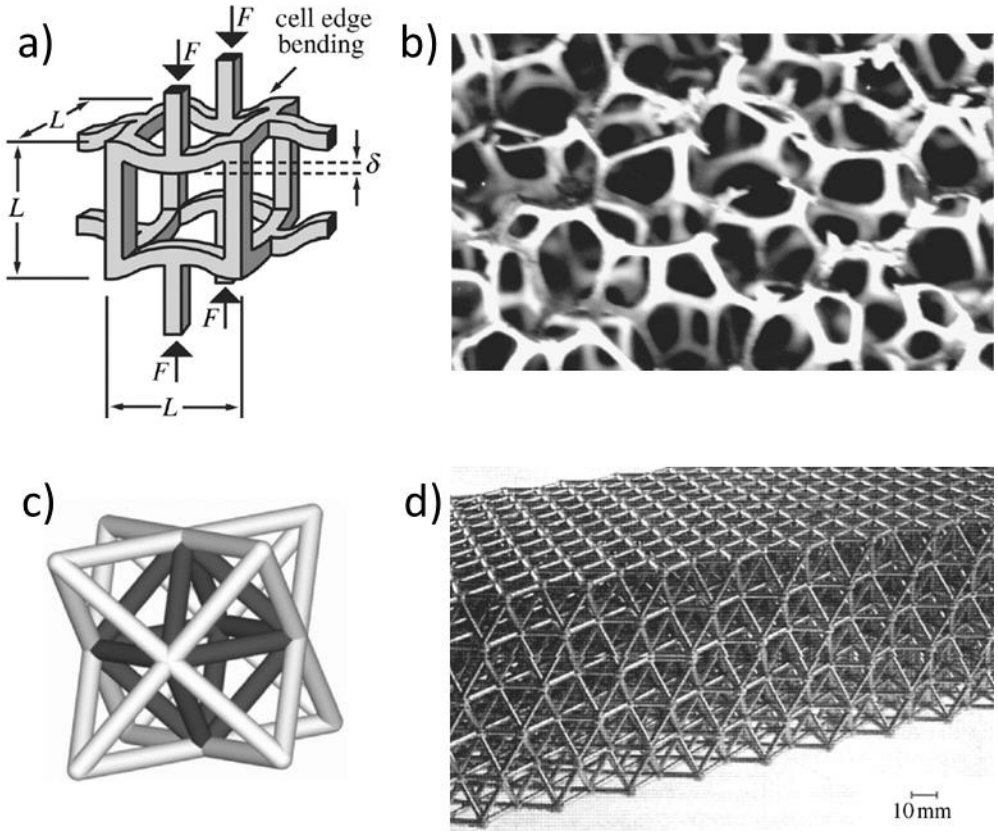

Figure 2.1 a) An idealized cell of bending-dominated structure; b) A typical cellular structure examples of bending-dominated mechanical properties; c) A unit cell of an FCC truss structure; d) A typical example of the stretch-dominated lattice material. (Ashby 2006)

These scaling laws generally point to stretch-dominated lattices when high stiffness and strength at low densities are desired. This guideline has acted meaningfully for many designs of mechanical metamaterials. However, such relationship based on beam theory falls short when bending and stretching are both active during the deformation of a material. Although an upper and lower bound can be provided, these scaling laws are less useful when the scaling relationship need to be precisely depicted.

2.3 Hashin-Shtrikman Bounds

In the 1960s, the upper and lower bounds were derived for the elastic properties of multiphase materials via a variational approach (Hashin and Shtrikman 1963). The multiphase material described was a mixture of several different isotropic elastic phases. The obtained upper and lower bounds have improvement over the Reuss-Voigt bounds. It has been claimed that the Hashin-Shtrikman (H-S) bounds for the effective bulk modulus of a two-phase material cannot be improved further.

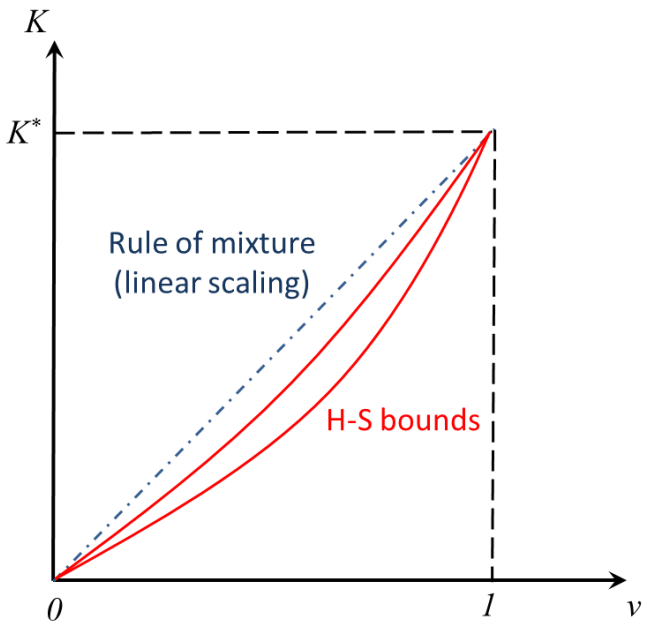

Figure 2.2 Schematic plot showing the comparison between rule of mixture (linear scaling) and H-S bounds regarding the bulk modulus of a cellular material. It shows that according to H-S bounds, a linear scaling across the full density range is not possible.

Particularly, when a two-phase material is consisted of a solid phase and a void phase, in another word, is a porous phase of a single material. The H-S upper bound for bulk modulus can be simplified as follows:

$$K_{HS+} = K + \frac{1 - v}{\frac{1}{-K} + \frac{3v}{3K + 4K}}$$

When we use the H-S bounds as references for low density high modulus mechanical metamaterials, it is natural to compare the H-S bounds with the scaling laws mentioned in the last section. It is clear that the H-S bounds are the improved bounds compared to the scaling laws. Therefore, the H-S bounds provide a better reference over a large mass density range. Because that the derivation of the H-S bounds does not use any phase distribution information, these bounds suit a wider range of mechanical metamaterials, like those which are not constructed with beam-like elements. However, it is for the same reason that the theory of Hashin and Shtrikman provides less clue on the spatial design of a mechanical metamaterial which high or low specific modulus is aimed.

2.4 3D Printing and Lattice Materials

Structural engineers have built architectures with lattices-like structures for decades (Lakes 1993). These architectures either need to be simple so that mass production is possible or need to be assembled with lower-order elements connected by joints or welds. Thanks to the rapid development of 3D printing technology, various of methods have been exercised to make periodic cellular materials with metals, ceramics and polymers in one step. This gives rise to the development of mechanical metamaterials where complex interior structures or ultra-fine features are produced in aim of exceptional mechanical properties. Among all the metamaterial designs, lattices with solid or hollow struts are the common ones (Jens Bauer et al. 2017).

The fabrication methods for lattice materials are diverse. One of the commonly-used, low cost solution of 3D printing is the fused deposition modeling (FDM) method (Masood 1996). FDM 3D printers typically use one or multiple heated nozzles to deposit thermoplastics or thermoplastic based composites in a layer by layer manner. Either the nozzle or the build bed is equipped with step motors. Limited by the diameter of the nozzle and accuracy of the step motors, the resolution of a typical commercial FDM 3D printer is around a few tens of microns. Another commercially available 3D printing solution is powder-based selective laser sintering (SLS). SLS methods can

deal with a variety of materials, among which the most attractive ones are ceramics and metals regarding high performance mechanical materials. Despite some drawbacks on the resolution, porosity, microstructure and surface finishing, SLS printers are the most competitive 3D printing solution if large engineering parts are desired (Yap et al. 2015). The 3D printing solution with the highest precision is through photopolymerization. The most precise photopolymerization process, namely the two-photon polymerization process, pushes the resolution of 3D printing to as low as 100 nm (Geng et al. 2019). As a result, nanoscale mechanical metamaterials can be made with either photopolymers or other materials that templated from them. The size-effect in nanoscale mechanical metamaterials have been reported as well (Greer and De Hosson 2011). All three types of 3D printing methods mentioned here have been commonly used in producing lattices materials in pursuit of mechanical metamaterials.

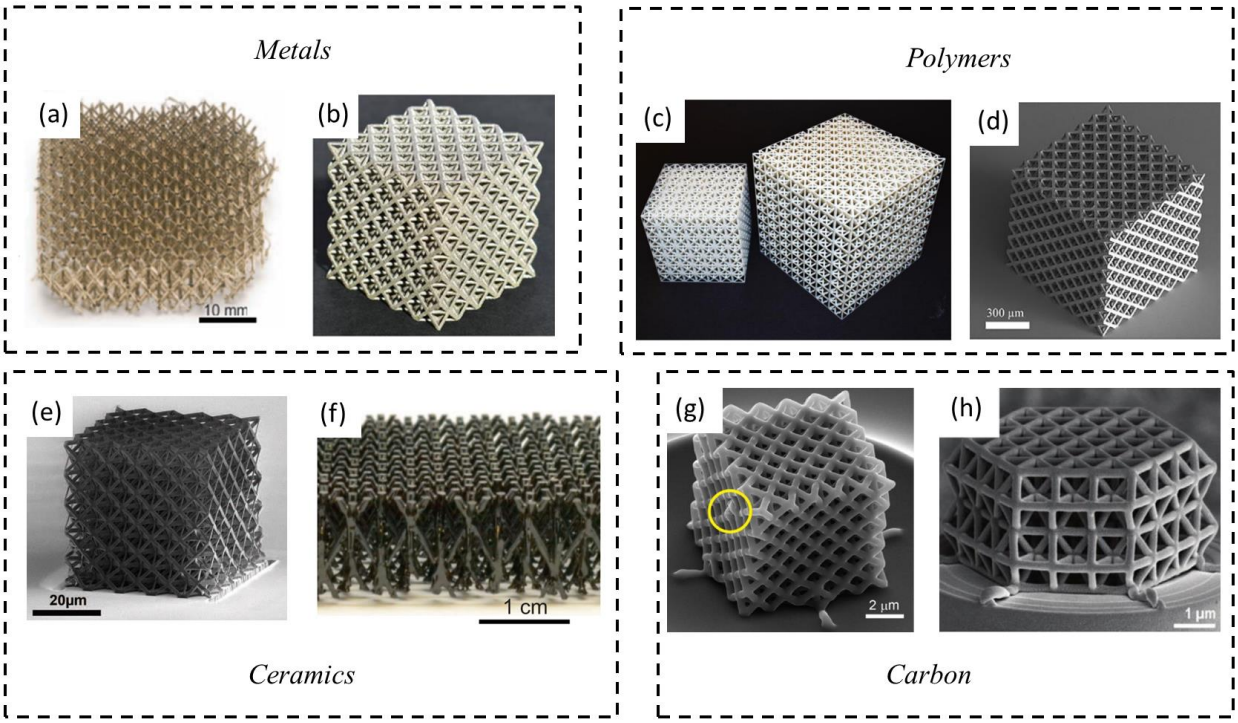

Figure 2.3 Various lattice materials made with a) electroless plated nickel on a 3D printed template (T. A. Schaedler et al. 2011a); b) SLS stainless steel (Bonatti and Mohr 2017); c) stereolithography resin (Tancogne-Dejean and Mohr 2018a); d) IP-dip resin via TPP method (Al-Ketan et al. 2018); e) templated ALD ceramic(Meza, Das, and Greer 2014); f) polymer-derived ceramic (Eckel et al. 2016); g&h) pyrolytic carbon from photoresin (J. Bauer et al. 2016; X. Zhang, Vyatskikh, et al. 2019).

Despite that lattice materials can be made to be compliant using bending-dominated designs and elastomeric base materials (Y. Jiang and Wang 2016), the discussion here mainly focuses on lattices materials with high stiffness or strength. Lattices materials with solid struts have been fabricated with various materials, such as metals (Meza, Das, and Greer 2014; Tancogne-Dejean and Mohr 2018b), ceramics(Eckel et al. 2016; Muth et al. 2017) and polymers (Tiemo Bückmann et al. 2012; Krödel and Daraio 2016). Out of all the lattice structures, which exclusively correspond to one crystallographic type (SC, Diamond, BCC, FCC, HCP, etc.), the FCC and HCP lattices are proven to produce the highest specific stiffness and strength (J. Bauer et al. 2016; Meza et al. 2017; Xu et al. 2019; Zheng et al. 2014). Each node in these lattices connects to 12 other ones, presenting the highest connectivity and stability. However, while reducing the effective mass density of a lattice with solid struts, the slenderness of the strut comes into play, making these structures susceptible to buckling (X. Zhang et al. 2018). On the other hand, lattice materials with hollow struts are produced with metals and ceramics, thanks to the intricate deposition methods on solid lattices templates. These lattice materials are generally much lighter than their solid templates and are among the representatives holding records for the world's lightest materials. Although these hollow lattice materials exhibit extraordinary specific stiffness and strength, shell buckling restrains the design parameters, such as strut length, diameter and the tube wall thickness. And the limitation of material choice refrains hollow lattice materials in the competition for the stiffest material. The current best record for stiffness and strength for lattices is presented by amorphous carbon solid lattices, fabricated from carbonization of photopolymer in size of nanoscale (X. Zhang, Zhong, et al. 2019).

2.5 Shellular Materials and TPMSs

Although significant progress has been made while pushing the specific stiffness or strength of lattice materials towards higher standards. It is not the only structure design that has excellent potentials. Cellular materials constructed with flat or bent surfaces are called 'shellular materials' (S. C. Han, Lee, and Kang 2015). Despite being considered stretch-dominated (Al-Ketan et al. 2018; S. C. Han and Kang 2019), these materials are no longer subject to the theory of stretching or bending mechanism, since the deformation in shellular structures is not dominated by the deformation of beams. Instead, the H-S upper bound are used often as a reference while evaluating shellular materials. An important question remains elusive: what kind of shellular structures can

be proven as an optimal one regarding reaching the H-S upper bound? Recently study shows that closed-cell cellular structures constructed with intersected polygons has been numerically examined to be a candidate (Berger, Wadley, and McMeeking 2017). These structures are showing a higher theoretical potential to reach the H-S upper bound compared to solid lattices (Tancogne-Dejean et al. 2018).

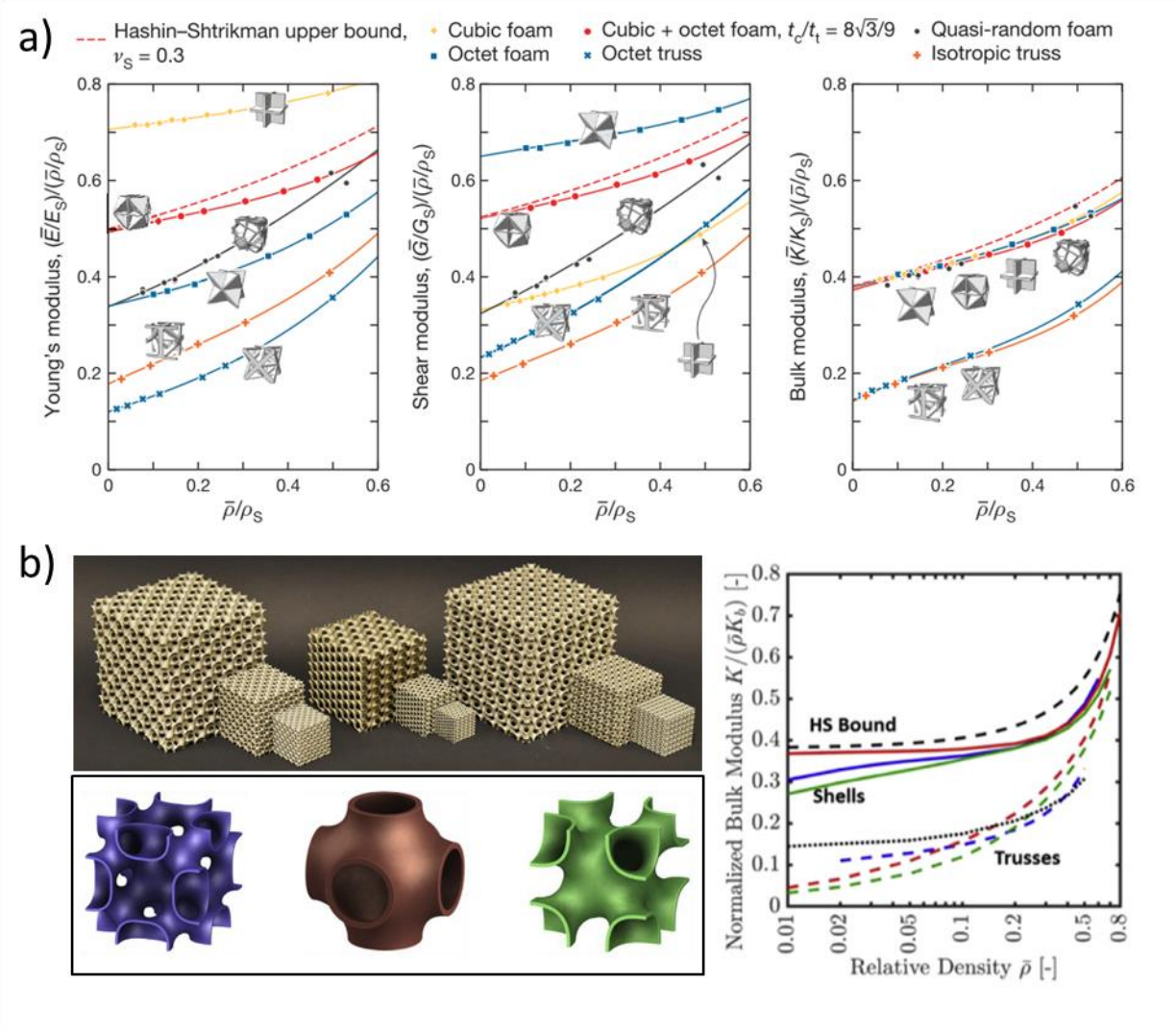

Figure 2.4 a) Numerical calculation showing that the closed-cell plate materials outperforming the truss lattices in terms of approaching the H-S upper bound (Berger, Wadley, and McMeeking 2017); b) Experimental approach via SLS metal printing showing superior mechanical performances of TPMSs (Bonatti and Mohr 2019b).

Triply periodic minimal surface (TPMS) is another example of metamaterial structure that has the potential to reach H-S upper bounds. A TPMS is a triply periodic surface which has zero

mean curvature at every point on the surface. Unlike closed-cell structures, TPMSs have no self-intersections, or are noted as embedded surfaces. A typical TPMS separate the infinite space into two parts, which means that a TPMS is an open-cell structures. An open-cell structure is easier adapted to 3D printing technologies than a closed-cell structure, since the closed space could trap raw materials like liquid resins or unsintered powders. TPMSs have been made with various materials such as metals (Al-Ketan, Rowshan, and Abu Al-Rub 2018), ceramics (Restrepo et al. 2017) and polymers(Abueidda et al. 2017; Al-Ketan et al. 2018). Both experimental and numerical results are showing that various TPMSs are promising candidates as metamaterial structures, while their mechanical performances are comparable to the H-S upper bounds (Bonatti and Mohr 2019a). Their potentials in other mechanical applications, such as energy absorption, has also been explored (Bonatti and Mohr 2019b).

It is also interesting to examine hollow lattices from the angle of shellular materials. Technically, hollow lattices are shellular designs, since a hollow lattice is constructed with embedded surfaces as well. The difference between a hollow lattice and a TPMS is that, a hollow lattice has strut regions with zero Gaussian curvature and node regions where either a sharp edge is present or a smoothening strategy is used, while a TPMS has zero mean curvature at every point. From a crystallography perspective, each hollow lattice has its TPMS counterpart, of which the symmetry is the same. It has been reported that the smoothening at the node regions is important for the mechanical properties of hollow lattices (Portela, Greer, and Kochmann 2018). The purpose of such smoothening should lie in reduction of stress concentrations.

2.6 Hierarchical Design of Metamaterials

Hierarchical design in mechanical metamaterials is adding secondary repetitive structures on the base of an existing metamaterial design. For example, a hierarchical lattice design is replacing the solid strut with hollow frames that are made of connected secondary strut. The first and secondary structures are often several orders of magnitude apart in feature length. This type of design is proven to be effective in improving the mechanical properties of the mechanical metamaterials such as stiffness and strength (Meza et al. 2015; Zheng et al. 2016). The theoretical basis of the multiscale hierarchy strategy is established using honeycomb structure in which the buckling failure is suppressed as the scaling law for strength is iteratively calculated. (Lakes 1993).

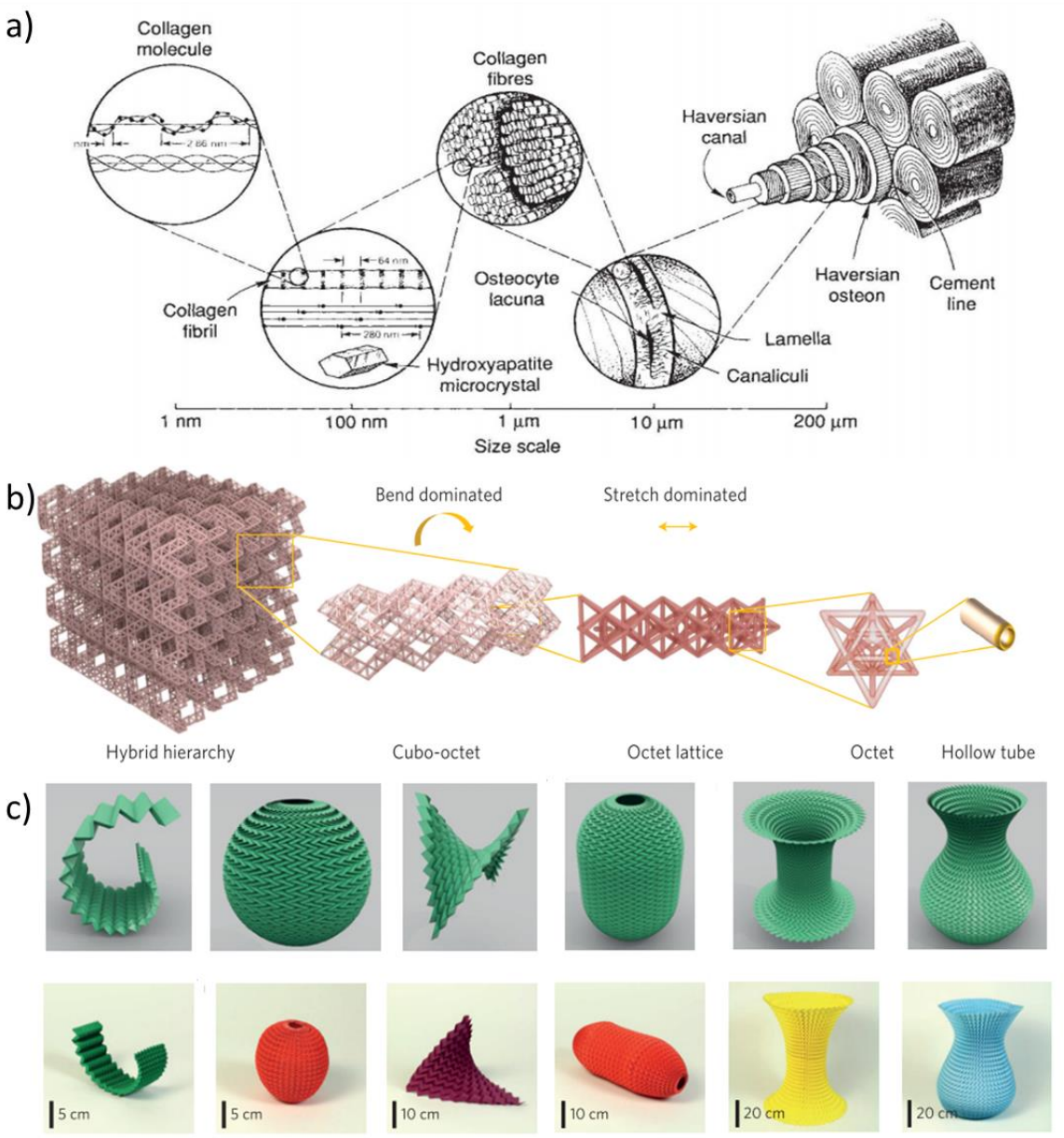

Figure 2.5 a) Hierarchical structure in human compact bone (Lakes 1993); b) A hierarchical hollow lattice metamaterials consisted of first-order bending dominated structures and second-order stretch dominated structures (Zheng et al. 2016); c) Programmed origami tessellation on curved surfaces, creating multi-order foldable structures (Dudte et al. 2016).

The hierarchical design of surfaces is analogously different. A flat thin shell usually has a low bending stiffness. Making the shell corrugated can significantly change the mechanical property of the shell. It has been reported by many that corrugated shells can be designed to be compliant and morphable (Bertoldi et al. 2017; Dias et al. 2012; Dudte et al. 2016; Lebée 2015;

Norman, Seffen, and Guest 2009; Seffen 2012). A famous example is the origami structure with a collapsing mechanism which usually take little energy. On the other hand, the mechanism in a corrugated structure usually only has one degree of freedom. In another word, a corrugated structure can turn stiff in it is bounded by external forces or simple boundary conditions. It is very often that the corrugated shells are used as the core of a sandwiched panel for packing purposes (Dayyani et al. 2015).These corrugated panels have shown outstanding mechanical performance in terms of resisting bending. However, a hierarchically designed shellular mechanical metamaterials with periodic structures is rarely seen.

3. COMPOSITE BENDING DOMINATED HOLLOW LATTICES WITH EXCEPTIONAL CYCLABILITY

3.1 Introduction

Nature has inspired people to incorporate multiple materials with distinct mechanical properties into a new category of materials: composite. It has affected human's life in numerous applications, such as structural materials (Veedu et al. 2006), heat dissipation (Yu et al. 2007), medical tools (Moutos, Freed, and Guilak 2007), energy storage (Jin et al. 2008), electronic devices (Ramamurthy et al. 2003), smart robotics (Kim et al. 2005), etc. Specifically, from mechanical perspective, when two different materials are organized in a periodic manner, such as lamellar or brick/mortar, their mechanical properties, such as strength, stiffness and toughness can be significantly boosted, overcoming the 'rule of mixtures' (Bouville et al. 2014; Dimas and Buehler 2013; Munch et al. 2008). Yet nature materials are internally dense as a bulk. For example, trabecular bone and wood have their unique micro or nano scale architectures, which improves their property/mass efficiency, i.e specific mechanical performance by reducing their weight (N. A. Fleck, Deshpande, and Ashby 2010; Gibson 2005; Wegst et al. 2015). Manufacturing of complex micro/nano architectures with composite materials with the least possible mass has been a challenge towards the best reproduction of nature's materials.

The advancement of 3D printing shed light on the impossible (Truby and Lewis 2016). Many complex micro/nano architectures have been achieved by both composite materials' design and nanoscale 3D architecture tailoring (Meza et al. 2015; Meza, Das, and Greer 2014; Tobias A. Schaedler and Carter 2016). Metal-based (e.g. Ni, Cu) microstructure via electroless plating (T. A. Schaedler et al. 2011b; Zheng et al. 2014), and ceramics (e.g. TiN and Al2O3) nanostructures via atomic layer deposition, were fabricated on 3D truss structures (Meza, Das, and Greer 2014; Meza and Greer 2014). 3D hollow architectures are featured with properties like ultra-light, ultra-stiff and recoverable, which opened new horizons for 'mechanical metamaterials' (Davami et al. 2015; J. H. Lee, Singer, and Thomas 2012). There are two major categories of truss structure designs: stretching dominated lattices (S-Lattice) and bending dominated lattices (B-Lattice) (Ashby 2006; N. a Fleck 2004). S-Lattices stand out for their high stiffness (J. Bauer et al. 2016), as the struts in the structure do not have freedom to rotate or bend due to the high nodal connectivity. However, most S-Lattices are faced with inevitable local buckling under large compressive strains.

Buckling in lattice materials, although plays a role in recovery of lattices, significantly affects the strength and cyclability of the structure. Contrary to S-Lattices, B-Lattices allow their struts to rotate or bend depending on whether the node is pin-joint or welded. Thus B-Lattices usually feature with compliance and resistance to impact damage under large strains (A. G. Evans et al. 2010; Y. Jiang and Wang 2016). However, compared with S-Lattices, the stiffness and strength of B-Lattices are lacking for critical structural components. Multiscale hierarchical 3D structures have been fabricated combining bending dominated design with stretching dominated structured beams in order to achieve both tensile stability and stiffness, however buckling still exists in the system causing unstable local damages.

In addition, due to the challenge of printing multiple materials on complex 3D geometries, material choices of aforementioned 3D architectures are limited. In many cases, only a single type of material can be applied when constructing multiscale 3D structures. Recently, composite material designs have been attempted to incorporate nanoscale architectures. Ceramic nanolayer reinforced graphene aerogels have been demonstrated with enhanced stiffness and superelasticity (Xu et al. 2019; Q. Zhang et al. 2017). However, as aerogels are constructed randomly, the potential to design their mechanical property and other functionalities is limited. On the other hand, ordered core-shell composite architectures have been fabricated by depositing ceramic or metal nanolayers on the surface of the 3D printed resin template (Jens Bauer et al. 2014; Mieszala et al. 2017). In these structures, buckling can be greatly inhibited as the core and the shell have different buckling behaviors and restrain each other through their interface. As a result, composite core-shell structures are often brittle and fracture before any buckling is shown. However, since the core diameter (~200-300 nm) is much larger than the shell thickness (~5-20 nm) in these structures, the size effect of the ultrathin shell layer and the coupling effect between the core and the shell, which could significantly enhance the strength, haven't been pushed to the optimum.

Herein, we demonstrate a bending dominated hollow nanolattice material (B-H-Lattice) with nanolayered struts to realize ultra-low density, high-strength, good recoverability and cyclability. The deformation mode of the fabricated nanolattices has been engineered through the unique material design and architecture tailoring. The hollow nodes in the B-H-Lattice are bendable, rendering the overall lattice recoverable. Meanwhile, a carbonized polymer nanolayer is deposited coherently on a ceramic nanolayer to enable non-buckling struts during deformation, resulting in better scaling factors and strength/density ratio than the current B-Lattices and carbon-based

cellulose materials. Unlike the current ceramic lattices, this B-H-Lattice exhibits good recoverability without any buckling behavior. Meanwhile, the composite B-H-Lattices have comparable stiffness and strength to existing S-Lattices with similar mass densities while with better cyclability and reliability. This approach provides a new way to scalable fabrication of advanced ceramic nanocomposites with engineered mechanical property that is comparable to nature produced materials.

3.2 Methodology

3.2.1 Fabrication of hollow ceramic/composite lattices

The fabrication of the hollow ceramic/composite B-H-Lattices starts with the fabrication of the 3D photoresist template. The 3D template is first modelled in AutoCAD and output as STL file. Then the STL file is written by Nanoscribe Photonic Professional GT with the laser power of 30 mW and the scan rate of 10000 μm/s. The photoresist is IP-dip from Nanoscribe GmbH. After the 3D templates are written on a glass substrate, the substrate is transferred to Fiji atomic layer deposition (ALD) system and are coated with amorphous Al_2O_3. The ALD process is conducted at 200°C with trimethylaluminum and oxygen plasma as the Al and O sources. The ALD deposition rate is 1 Å/cycle. Following the Al_2O_3 deposition, the substrate is immersed into the solution of 10 mM tris and 2 g/L with stirring for polydopamine (PDA) deposition. PDA deposition duration is 1.5 h. Finally, the substrate is annealed at 500°C for 1 h under Ar protection to remove the polymeric templates and obtain composite B-H-Lattices.

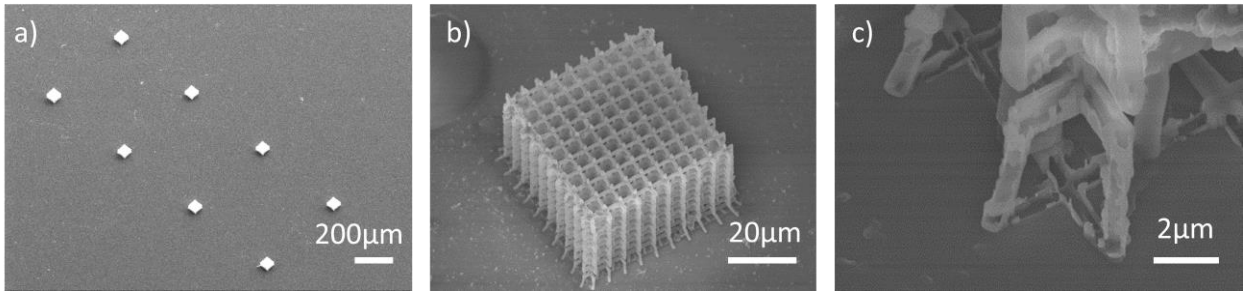

Figure 3.1 a) Composite hollow structures as prepared on a piece of glass slide; b) magnified view of a composite hollow structure; c) bottom corner of the composite hollow structure, milled by focus ion beam to expose the hollowness inside.

Fig. 3.1a shows a glass slide with 8 distinct lattices in a 2 by 4 array. To examine the hollowness of the lattices, focused ion beam is used to mill the bottom corner of the lattice in Fig. 3.1b. As shown in Fig. 3.1c, the resin template inside is completely removed by the furnace annealing process. We also discover that the struts in a pure alumina lattice (tube wall thickness = 15 nm) could easily flatten or distort during the thermal removal of the template, since the thermal evaporation or decomposition of the polymeric template could cause pressure difference between inside and outside the hollow struts. Introducing the extra carbon coating could greatly help the struts to resist the excessive shape change during of the template removal process. A typical example of pure alumina structure with flattened struts is shown in Fig. 3.2b&c. Rarely any composite lattice shows compromised shapes after the furnace annealing when the alumina thickness is still 15 nm, see Fig. 3.2d&e. Therefore, to fabricate the ceramic lattices with least shape changes, we took another air annealing step on the basis of successfully prepared composite lattices. During the air annealing at 500°C for 1 h, the carbonized PDA (C-PDA) layer is completely removed.

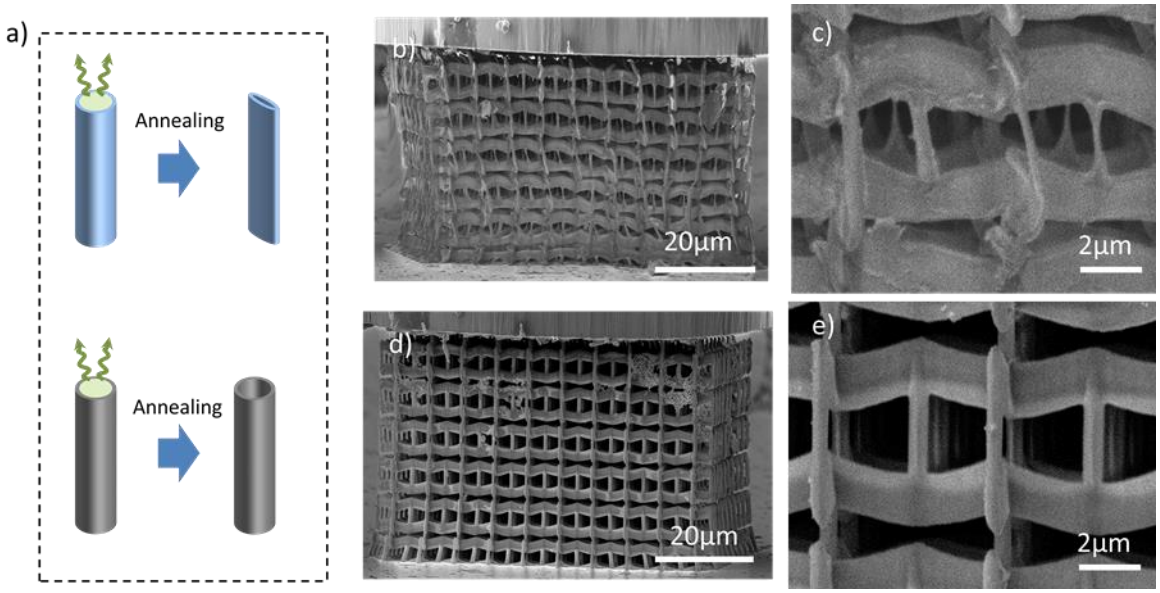

Figure 3.2 a) schematic figure to show that pure ceramic hollow tubes flatten out during thermal removal of the inner resin, but composite tubes withstand thermal degradation of inner resin; b) a pure ceramic hollow structure as prepared with c) flattened struts; d) a composite hollow structure as prepared with e) tubular shaped struts. The thicknesses of alumina for structures in b) & d) are both 15 nm.

3.2.2 Film composition and surface morphology

We used AFM to test the surface morphology of the film as well. Unlike an ultra-smooth surface from ALD, the surface of the film has a roughness around 3-4 nm, shown in Fig. 3.3. This was because when self-polymerizing in aqueous solution, the precursor PDA tended to form in particle-shape along the surface. This result also confirms the thickness of the ceramic layer and the C-PDA layer.

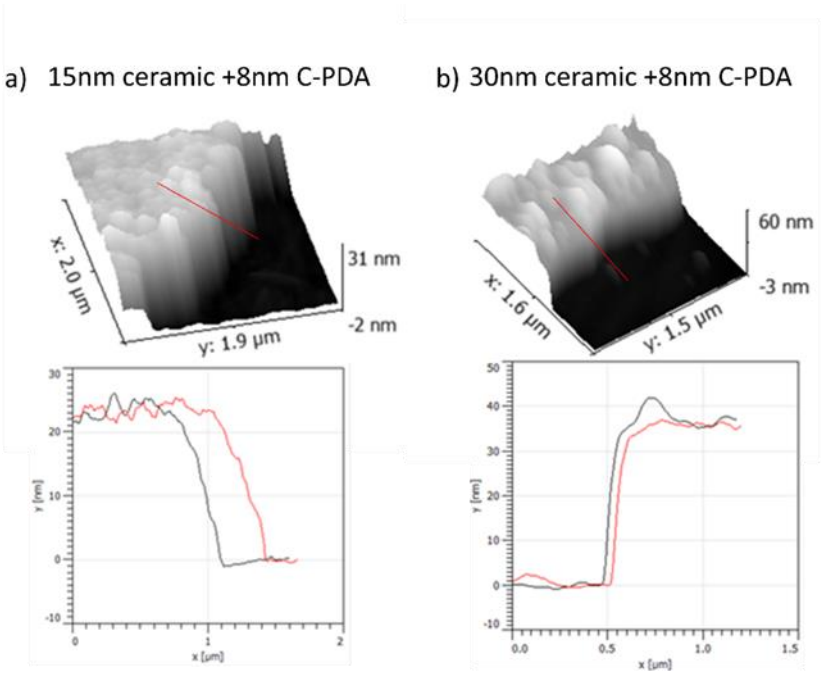

Figure 3.3 AFM image of the edge of two different composite film on top of a glass slide. Red lines in the upper AFM images indicate the measured paths, of which the results are shown in the lower graphs. The composition of the films is: a) 15 nm alumina + 8 nm C-PDA; b) 30 nm alumina + 8 nm C-PDA.

3.2.3 Crack propagation on composite thin film

In order to observe the crack propagation of the ceramic and composite film. The 15 nm ceramic film and 15 nm ceramic plus 8 nm C-PDA composite film were tested via nanoindentation on soft substrate PDMS. Both coatings were dented by Vickers indenter in depth of 1 um than the morphologies of the coatings were investigated by AFM. As shown in Fig. 3.4, At the dent of pure ceramic coating, the cracks were visible, and edge of the crack tilted up 20 nm from the flat surface. This was because accompanied with the crack generation, the yielding of the ceramic was also

severe, hence the broken edges couldn't match when the soft substrate pushed them to recover. In contrast, for the dent on the ceramic/carbon composite coating, open cracks were not visible. There were ridge-like lines which was probably caused by the failure in the ceramic layer, yet the cracks didn't show up since the carbon layer could hold the possible broken edges together. The height of the ridge was 10 nm, lower than the 20-nm tilt caused in the pure ceramic coating.

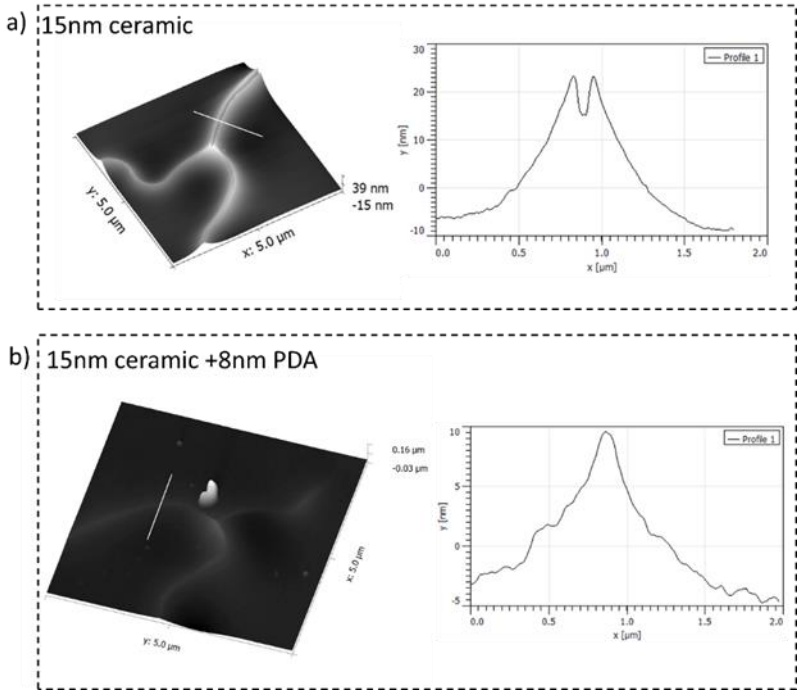

Figure 3.4 AFM image of the dents generated by nanoindentation on a) 15 nm alumina; b) 15 nm alumina + 8 nm PDA. White lines in the AFM images indicates the measured paths, of which the results are shown in graphs on the right. Nanoindentation was performed respectively on each film on a soft substrate, the indentation depth is 1 μm.

3.2.4 Theoretical calculation for modulus

If we consider the effective stress and strain in a lattice dominated by ideal beam bending deformation, the relationship is

$$\varepsilon \propto \frac{\sigma L^4}{E_s I}$$

here, L is the average beam length, E_s is the material's intrinsic Young's modulus, and I is the area moment of inertia of the beam.

When the beam is a thin cylindrical shell with diameter D and thickness t, we have

$$I \propto D^3 t$$

Then,

$$\frac{E}{E_s} = \frac{\sigma}{E_s \varepsilon} \propto \frac{D^3 t}{L^4}$$

Set $\alpha = \frac{t}{D}$ and $\beta = \frac{D}{L}$,

$$\frac{\rho}{\rho_s} \propto \frac{Dt}{L^2} = \alpha\beta^2$$

$$\frac{E}{E_s} \propto \frac{L^4}{D^3 t} = \alpha\beta^4$$

So, for the scaling factor k in

$$\frac{E}{E_s} \propto \left(\frac{\rho}{\rho_s}\right)^k$$

if the mass scaling strategy is by increasing the thickness while the aspect ratio of the structure remains constant, which means β is fixed, we should have k = 1.

3.2.5 Calculation for failure modes preference

Here we examine the plastic failure on the horizontally aligned hollow struts when the structure is compressive vertically. As we have the yielding moment

$$M_f = \frac{\pi \sigma_{y,s} D^2 t}{4}$$

This moment is transferred from both ends of the horizontal strut where connected to vertical struts that carry compressive loads. So

$$M = \sigma \cdot \frac{\pi D t L}{4}$$

The factor of ¼ come from the four-fold structure nature, splitting the compressive load into 4 equal slices.

So, when shell buckling happens ($\sigma = \frac{E_s}{\sqrt{3(1-\upsilon^2)}} \cdot \frac{2t}{D}$), we have

$$M_{sb} = \left(\frac{E_s}{\sqrt{3(1-\upsilon^2)}} \cdot \frac{2t}{D}\right) \cdot \frac{\pi D t L}{4}$$

Let M_{sb} equal M_f, we have

$$PL = \left(\frac{tL}{D^2}\right)_{cr} = \frac{\sigma_{y,s}\sqrt{3(1-\upsilon^2)}}{2E_s} \approx 0.02$$

Here for both our ceramic and composite lattices, we have PL>0.1, which means plastic yielding will occur before shell buckling when the structure failure first initiates.

3.2.6 Numerical Simulation

Finite element modelling (FEM) via Abaqus were performed to study the deformation of the ceramic/composite B-H-Lattices. The outer shell of the CAD model was output as the geometry used in FEM. The simulation was conducted in Abaqus dynamic/explicit mode. The materials properties were set to be linear elastic: 1) alumina, E = 180 GPa, v = 0.22; 2) C-PDA, E = 100 GPa, v =0.2. Composite plies were set to simulate the composite situation. FEM results of the elastic deformation of the B-H-Lattice suggests that the stress is concentrated at the nodes of the lattice.

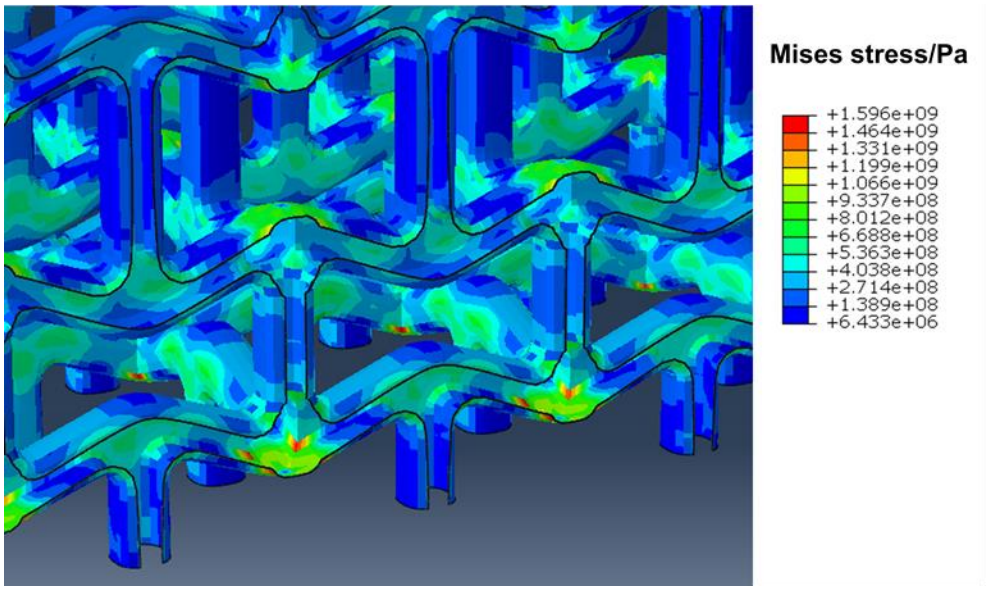

Figure 3.5 Finite element modelling (FEM) of uniaxial compression of a hollow composite lattice shows that the stress is concentrated at the nodes of the lattice.

3.3 Results and discussion

3.3.1 Hierarchical metamaterials design with 4th dimensional control of nanolayers

The fabricated B-H-Lattice consists of 8 stacks of four-fold symmetrical bow-tie units supported and interconnected by vertical struts, as shown in Fig. 3.6.

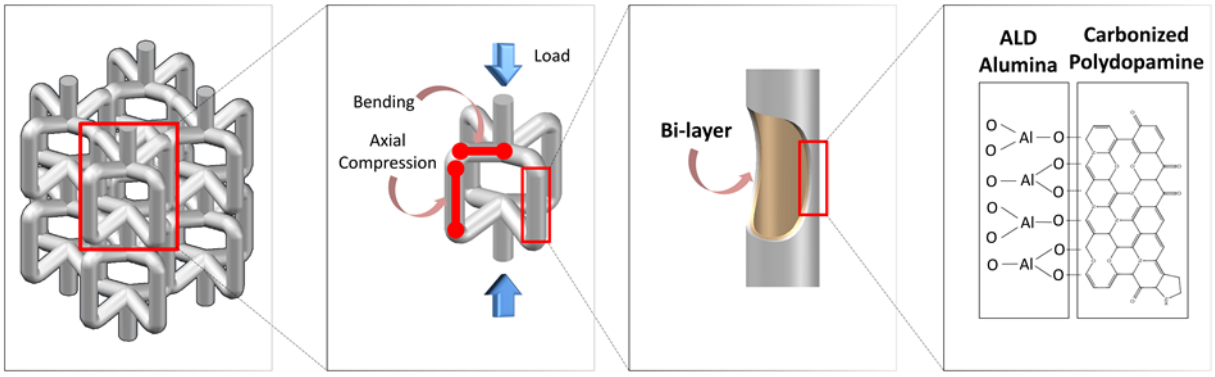

Figure 3.6 Illustration of multiscale design of the composite hollow lattice.

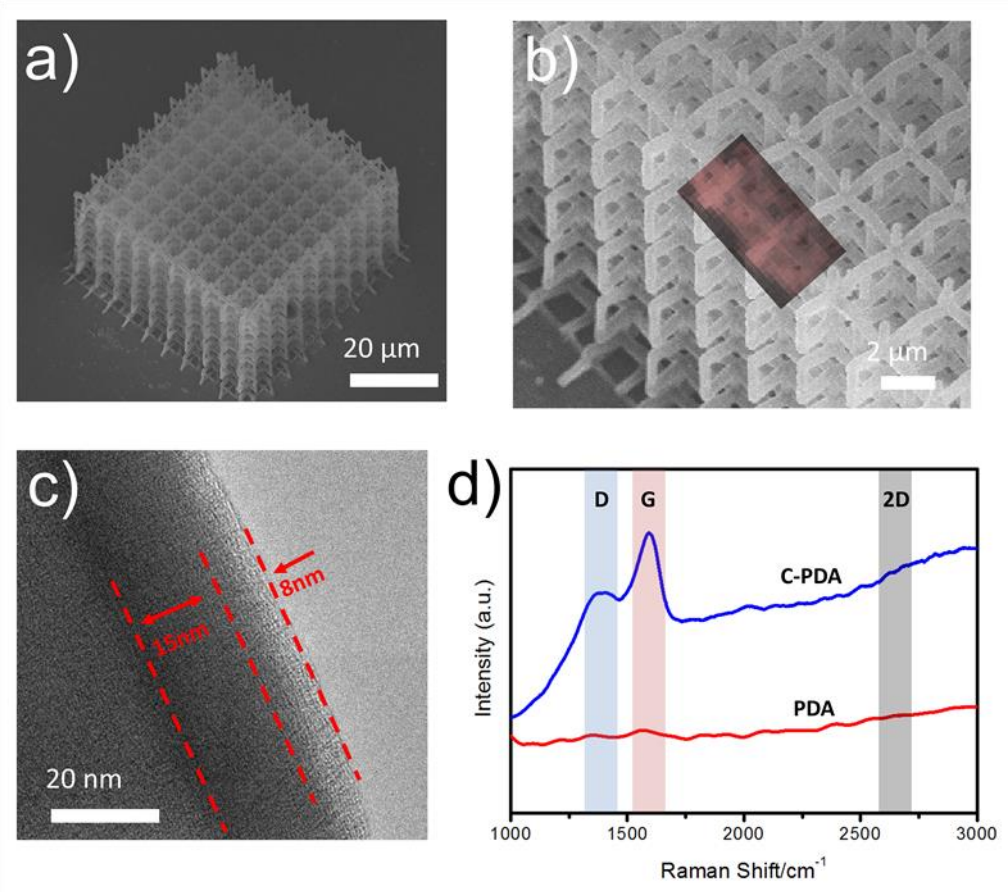

Figure 3.7 a) SEM image from a tilted view of a composite hollow lattice; b) Zoomed SEM image of a composite hollow lattice, with an inserted heatmap of Raman signals from G peak of carbonized polydopamine (C-PDA); c) TEM image of the tube wall of a hollow strut from the composite hollow lattice, showing that the thickness of alumina nanolayer is 15 nm and that the thickness of C-PDA nanolayer is 8 nm; d) Raman spectrum of the as-coated polydopamine (PDA) and C-PDA;

The lattice templates are fabricated by interference lithography with UV curable resin. An interior nanolayer of alumina and an exterior nanolayer of carbonized polydopamine (C-PDA) are subsequently deposited on the 3D templates. Polydopamine (PDA) is a mussel-inspired bio-polymer, which can be deposited with aqueous chemical reaction (H. Lee et al. 2007). We choose PDA as the precursor of our coating since it forms a nanolayer conformally on arbitrary surface geometries and its thickness is controllable down to sub-10 nm (Ball et al. 2012). Also, since PDA was first used for an adhesion layer (B. P. Lee et al. 2011), the interface between PDA and substrate is robustly bonded, which could prevent the composite nano-layers from potential delamination (B. Li et al. 2009; Ou et al. 2011). After the deposition, the resin template was removed by thermal decomposition at 500°C for one hour. A hollow architecture with nanolayered walls then remains on the glass substrate. The C-PDA nanolayer is characterized by Raman spectroscopy and X-ray photoelectron spectroscopy (XPS). The Raman spectrum of the nanolayered wall before the furnace carbonization shows no distinct peaks. As a comparison, D peak (~1300 cm-1) and G peak (~1600 cm-1) are present on the Raman spectrum of the thermal processed nanolayered wall. Raman signal of the G peak is mapped on the nanolayered lattice (Fig. 3.7b), showing that C-PDA layer is conformally deposited on the 3D geometry. TEM inspection indicates that the nanolayered wall consists of 15 nm of alumina and 8 nm of C-PDA. The TEM image (Fig. 3.7c) also confirms the tight attachment between the C-PDA and alumina nanolayers. We also examined the energy-dispersive X-ray spectroscopy (EDS) mapping on the lattice to confirm the successful deposition of Al_2O_3 and C-PDA, as shown in Fig. 3.8.

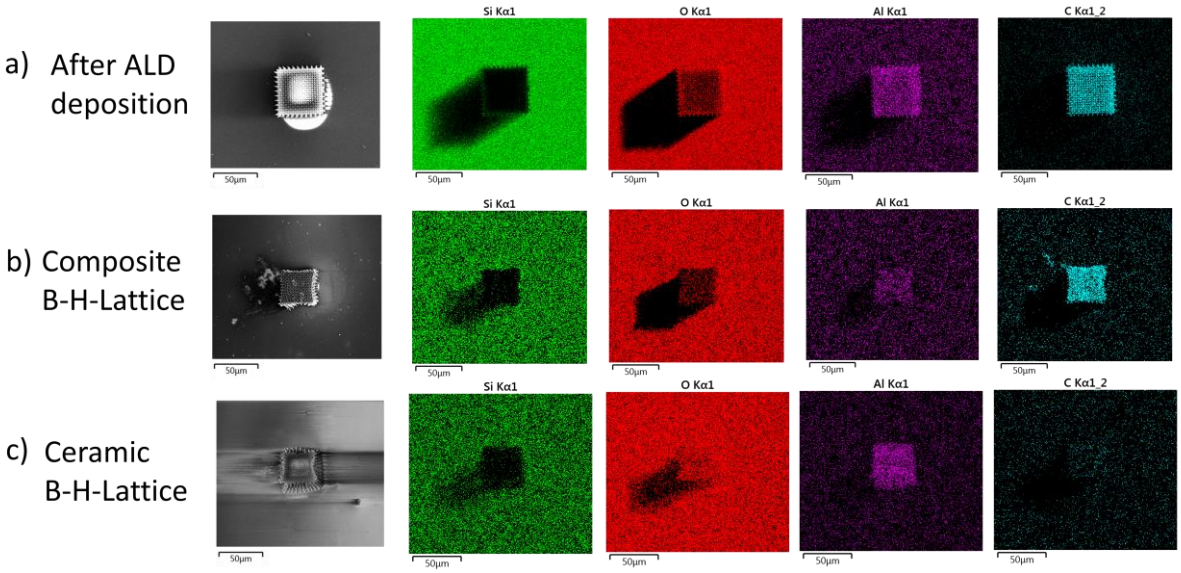

Figure 3.8 EDS mapping data of the lattices. a) The lattice after ALD deposition, with elemental maps showing successful deposition of Al_2O_3; b) the composite B-H-Lattice, with elemental maps showing both Al_2O_3 and C-PDA; c) the ceramic B-H-Lattice, with elemental maps showing only Al_2O_3 and no carbon.

XPS spectra (Fig. 3.9) of the annealed film were obtained on a flat glass substrate. The fabrication process of the composite film is the same as the process to produce composite 3D structure. XPS data shows the impurities of nitrogen and oxygen in the C-PDA layer. C 1s (spectrum can be deconvoluted into four peaks at 284.8eV (C-C, C-H), 286.2eV (C-O-C, C-N), 287.5eV (C=O) and 288.85eV (O-C=O) respectively. N 1s spectrum showed nitrogen atoms in C-PDA of 3 states: N1 at 398.53eV for pyridinic nitrogen, N2 at 400.58eV for pyrrolic nitrogen and N3 at 403.13eV for pyridinic nitrogen oxide. N4 at 405.63eV is a π-satellite peak and N5 at 407.23eV is from $NaNO_3$ in glass substrate. No graphitic carbon or nitrogen was detected. Al 2p spectrum showed a single peak at 74.6eV from aluminum oxide, meaning the chemical state of aluminum was not altered by the high temperature annealing. Interestingly, we didn't find peak for Al-O-C, which is typically around 75.5eV. This means although ALD aluminum oxide layer and C-PDA layer were tightly attached with each other, there was no chemical bonds in between. The major force between the two layers could be solely van der Waals force.

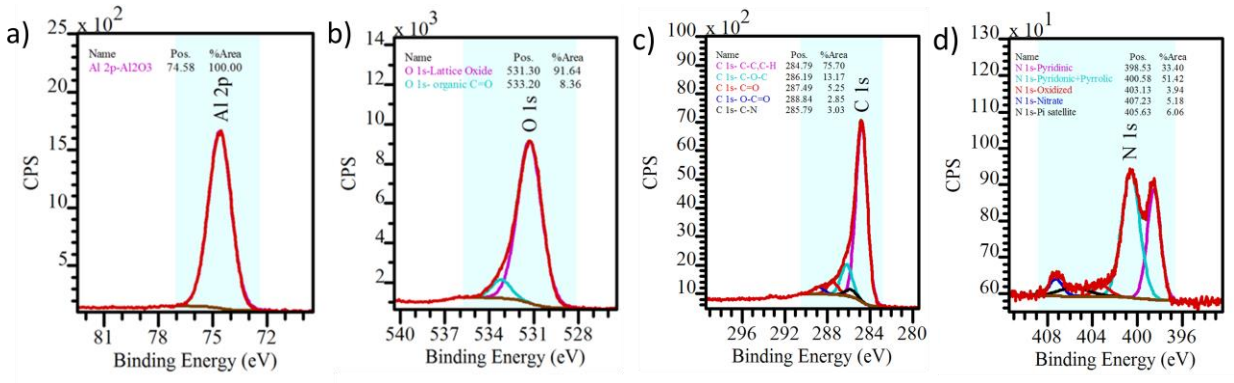

Figure 3.9 XPS spectra for alumina/C-PDA composite film: a) Al 2p; b) O 1s; c) C 1s and d) N 1s. Calibration of the XPS peak positions was conducted by setting main C 1s peak to 284.8 eV.

The functional groups in C-PDA, such as C-O, C-O-C and C-N, have been reported to enhance the interfacial attachment between the two nanolayers through the formation of hydrogen bonding (Y. S. Lee et al. 2016; Parnell et al. 2016). Even when the nanolayers are bound merely by Van der Waals force, the friction between the nanolayers can ramp up dramatically if the contact is conformal (S. Li et al. 2016). As a result, no delamination is observed between alumina and C-PDA during mechanical tests in this study. It is worth noting that the delamination in core-shell components is a problem in several reported 3D composite lattices (Jens Bauer et al. 2014; Mieszala et al. 2017).

3.3.2 Recoverability and cyclability of the B-H-Lattice metamaterials

We studied the deformation of the two types of B-H-Lattices, ones with 15-nm alumina nanolayer and ones with 15-nm alumina/8-nm C-PDA nanolayers. The recoverability and cyclability are compared using in-situ SEM compression test (displacement rate: 100 nm/s) and flat punch indentation test (displacement rate: 20 nm/s). In the case of pure alumina B-H-Lattices, as in the SEM images in Fig. 3.10a, when the strain goes beyond elastic range, local "necking" appears near the bottom of the structure. This is caused by the "node bending", which will be discussed in the next section, in bow-tie units, leading to a decrease of horizontal dimensions of the overall lattice. The effective strain of the lattice is concentrated at the bottom right of the lattice where the necking started to develop, as shown in the strain map in Fig. 3.10a. From the displacement vectors in the strain map, the upper part of the lattice, where the effective strain is close to 0, is moving down along Z direction. Notably, the buckling of the individual hollow strut is predominant in the

necking part of the lattice. Because of the severe local buckling, the ceramic structure cannot fully recover under 45% compressive strain (true strain), as in the stress-strain curve of the recovery cycle of the ceramic lattice in Fig. 3.10c. During unloading, the stress/strain curve shows several sharp spikes, indicating structure suffers from mechanical instabilities that could affect the stress response. Such mechanical instabilities could be caused by progressive failure, either elastic buckling or cracks, from deformed areas to connected nodes or struts, especially when the SEM imaging requires stalling of the loading process in an in-situ SEM test.

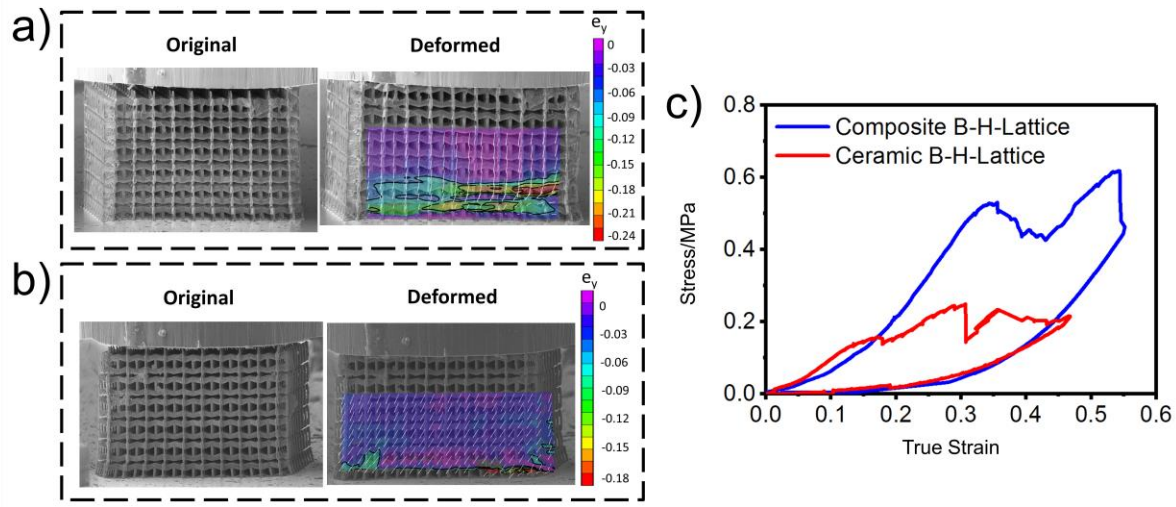

Figure 3.10 Comparison of the side views of hollow lattices comprising of a) a 15-nm alumina nanolayer and b) 15-nm alumina and 8-nm C-PDA nanolayers. The image on the left shows the lattice before compression; the image on the right shows the lattice during compression. Colored contour is the accumulated strain map for the compressed lattice, obtained by tracking the pixels from consecutive SEM images. c) Stress-strain responses of the two types of hollow lattices.

In contrast, the ceramic/C-PDA B-H-Lattices can recover from a compressive strain of 55%. After unloading, the structure returns to its original position with a smooth stress-strain curve (Fig. 3.10c). No necking or buckling is observed, as shown in Fig. 3.10b. As shown in the strain map, strain concentration only occurs between the bottom two stacks of bow-tie units. The effective strain at the bow-tie units is close to 0, while most of the deformation is on the nodes that are mostly hidden in the SEM image. And this is the reason that our digital image correlation software is only able to map the nodes with high strain concentration partially (bottom right). During compression, adjacent stacks of the unit cells snaps to a mismatched position while compressed vertically, as shown by the displacement vectors in the strain map where the upper

part of the lattice is moving towards bottom left. The reason for the snap happening is that buckling, as a way of accommodating compressive deformation, is prohibited due to the enhanced buckling strength of the hollow composite struts. The same snapping process occurs between several stacks along the vertical direction, when the lattice is compressed further. Thus, the ceramic/C-PDA nanolayered B-H-Lattice shows zigzag pattern along Z-axis but no distortion in the X-Y dimensions during severe compression. Notably, such snapping process is often introducing sharp drops in stress response during in-situ SEM compression (Fig. 3.11a). However, such stress drops would not significantly affect the recoverability. Before collecting the stress-strain curves of the recovery cycles, lattices have been preloaded so that the recovery behavior can be best captured.

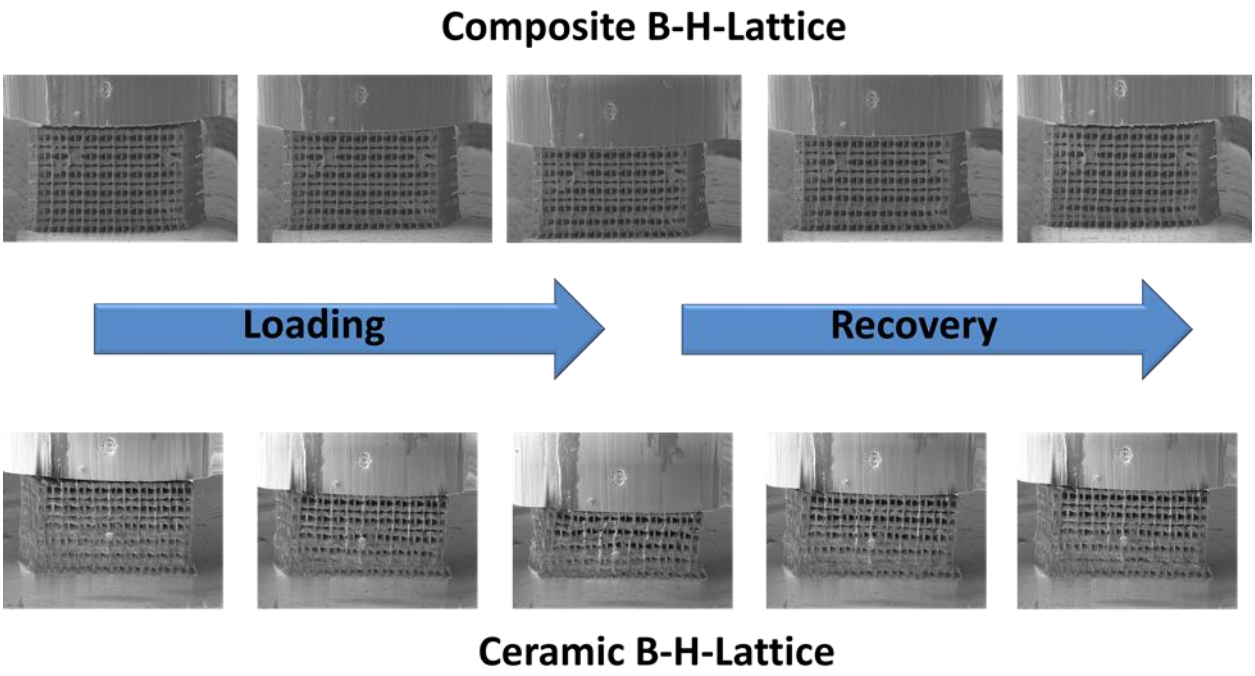

Figure 3.11 Comparison of the recoveries of the pure ceramic lattice and the composite hollow lattice.

For the current recoverable microlattices, elastic buckling of the hollow struts is the main mechanism of recovery. Apparently, in the composite B-H lattices presented here, elastic buckling and recovering on hollow struts are no longer the mechanisms for the shape recovery. The elastic deformation mainly resides on the nodes during compression. As the load is released, the lattice will recover with strut rotations. Such deformation mechanism change also affects the stiffness values of the microlattice during loading and unloading. It turns out that the pure ceramic B-H-

Lattice has a 'softening' behavior, that after being loaded beyond elastic range, the unloading stiffness of the lattice decreases by 23%, as calculated from the slopes of the stress-strain curves. The phenomenon of stiffness loss upon the second loading cycle has also been reported in other truss structures and tubular graphene foams (Bi et al. 2015). The deformation of these cellular structures is all dominated by buckling. On the contrary, in ceramic/C-PDA nanolayered B-H-Lattice, the 'softening' behavior is absent. The stiffness upon unloading even increased 12% compared to loading stiffness, indicating simultaneous elastic and plastic deformations during loading. The loss of stiffness during loading/unloading in pure ceramic B-H-Lattice can be explained by irreversible buckling of the hollow struts. In the ceramic/C-PDA nanolayered B-H-Lattice, because the buckling of the tubular struts is mostly inhibited, the 'softening' effect is thus suppressed.

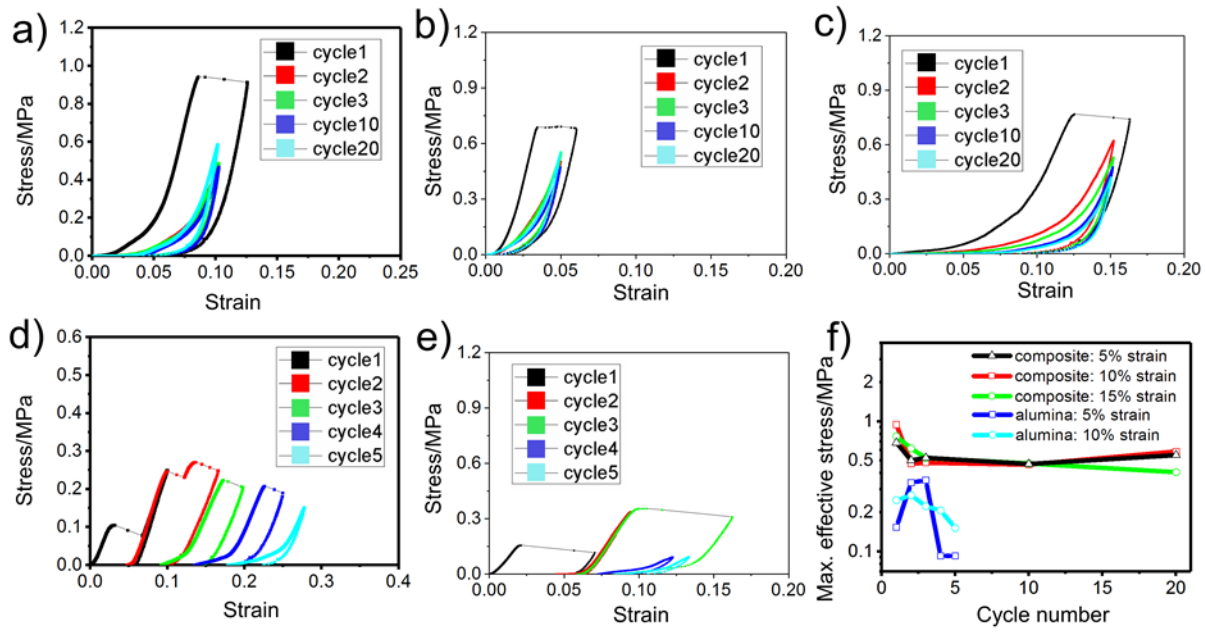

Figure 3.12 a-c)Stress-strain relationship of the composite hollow lattice for 20 cycles at the strain of a) 10%, b) 5% and c) 15%; d&e) Stress-strain relationship of ceramic hollow lattice for 5 cycles at the strain of d) 10% and e) 5%; f) Maximum effective stress of the ceramic and composite lattices during cycling tests.

The cyclability of the ceramic/C-PDA B-H-lattice is compared with that of the pure ceramic B-H-lattice with the same alumina layer thickness, i.e., 15 nm, via dynamic flat punch indentation, the displacement rate of the punch is 20 nm/s. For the compression of the pure ceramic B-H-lattice, the peak stress drops significantly from 0.35 MPa to 0.09 MPa after 4 cycles at 5%

cyclic strain. While at 10 % cyclic strain, the peak stress drops from 0.27 MPa to 0.22 MPa, 0.21 MPa, and 0.15 MPa after 2, 3, 4 cycles respectively, as shown in Fig. 3.12. In addition, the stiffness loss occurs after 3 cycles at the cyclic strain of 5% and after 2 cycles at the cyclic strain of 10%. While several abrupt stress drops occur during the compression, the ceramic lattice fails to recover from each compression cycles and eventually is crushed progressively. At the compression of 15% strain, the ceramic B-H-lattice catastrophically fails at the first cycle. In contrast, the ceramic/C-PDA B-H-lattice shows stable cyclic behavior with significantly higher peak stress level up to 20 cycles of compression at the strain of 5%, 10% and 15% respectively. In the meantime, the peak stress from the second compressive cycles at 5% and 10% strains shows no sign of reduction in our experiments. It can be seen that simultaneous elastic and plastic deformations occur in the loading process, which is consistent with our findings that that the stiffness value during unloading would increases compared to that of loading. Under strain of 15%, the stress drops slightly from the second cycle to the 20th cycle, and the lattice shows full recovery and no sign of failure. Typically, the stress-strain curve of the first cycle of the ceramic/C-PDA B-H-Lattice has a plateau after the peak stress is reached. Based on the observation in the in-situ SEM compression test, the plateau corresponds to the lattice snapping process triggered by a critical compressive load. It is notable that in the flat punch indentation test, the stress level recorded during the lattice snapping is stable (Fig. 3.12f), while in a SEM compression test, such lattice snapping often is associated with stress drops. The reason is likely to be the different displacement control mechanism in these two tests. For an indenter, the tip transducer displacement is controlled in a load-dependent way, while for a micro-tester compression device inside the SEM, the displacement is controlled by a 3-axis positioning stage as the tip and the load cell is kept static.

3.3.3 Size effect on deformation/failure of B-H-Lattice metamaterials

As shown in the previous section, the ceramic/C-PDA B-H-Lattice has a different deformation mechanism from the pure ceramic B-H-Lattice. The failure of the pure ceramic B-H-lattice is dominated by buckling of the hollow struts. When the buckling occurs, the lattice tends to lose their stiffness quickly resulting in mechanical ruptures. In contrast, struts buckling is suppressed during compression of ceramic/C-PDA B-H-Lattices, while the deformation is localized at the lattice nodes. In the meantime, the C-PDA nanolayer can stabilize the cracks in the alumina nanolayer during propagation as previously stated, this will help the hollow nodes withstand large

deformation. To better understand the local deformations of the B-H-Lattices and further study the size effect of the ceramic/C-PDA nanolayers, we categorized the deformation within the lattice into 3 types: beam stretching, beam bending and node bending, as shown in Fig. 3.13. A similar categorization can be found in the study of general elastic networks (Gurtner and Durand 2014).

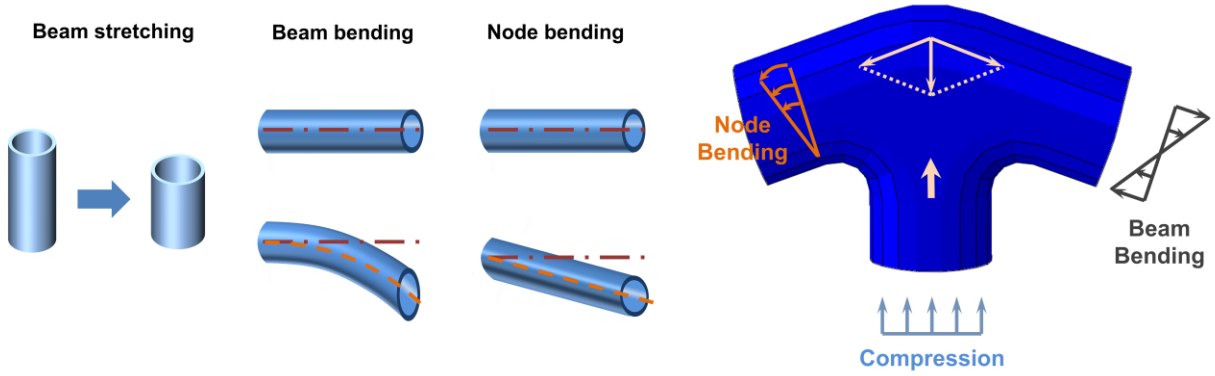

Figure 3.13 The deformation induced by uniaxial compression test at the nodes of a lattice can be divided into: beam stretching, beam bending and node bending.

It is often observed in hollow microlattices compression that the deformation and failure occur at the nodes of the lattice. However, the node bending mode is often comprised of complex deformation of the shells around the hollow nodes, whose scaling factor couldn't be generalized by simple analytical calculation. Therefore, finite element modelling (FEM) is conducted to simulate the deformation of the B-H lattices. To verify our numerical results, the moduli of the lattices of i) 15 nm Al_2O_3, ii) 15 nm Al_2O_3 + 8 nm C-PDA and iii) 30 nm Al_2O_3 + 8 nm C-PDA, are probed. The three simulated cases were compared to their experimental counterparts. As shown in Fig. 3.14, the FEM predicts the elastic behavior of the lattices well.

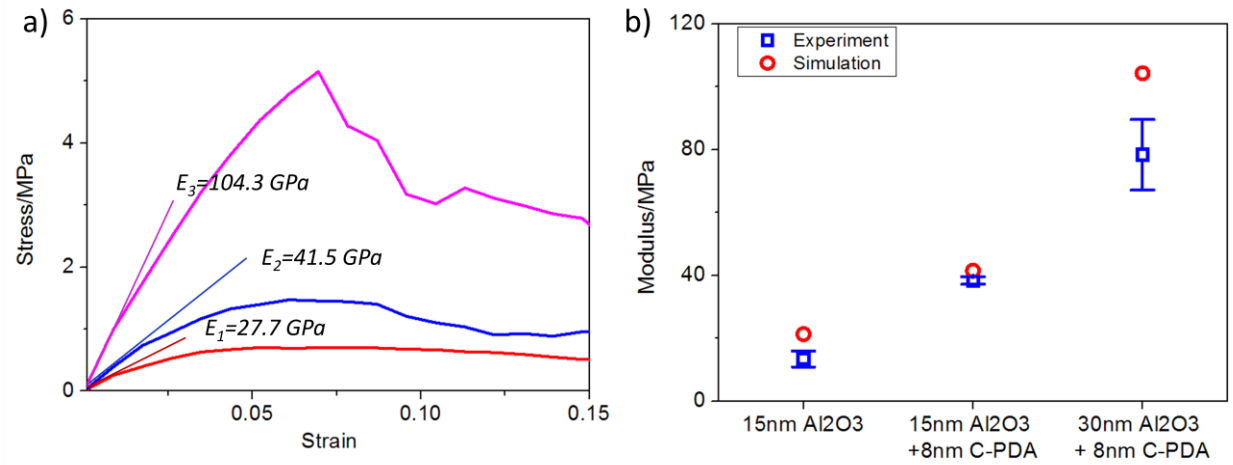

Figure 3.14 a) Calculated stress-stress curves and corresponding moduli for different lattices. b) Comparison between the experimental and simulated moduli of different lattices.

Further, the FEM results are used to reveal the differences of the three simulated lattices regarding bending modes. As shown in Fig. 3.15a, the beam bending mode and node bending mode will have different rotational displacement (UR) distributions along a vertical strut. Typically, the beam bending mode will cause the UR to peak in the middle of the strut (triangular distribution), while the UR in the node bending mode will have a steady value along the strut (rectangular distribution). The x-axis component of the UR is tracked along the top of a vertical strut in the center of the lattice (Fig. 3.15b) up to a compressive strain of 2.61%. Fig. 3.15c shows the different UR distribution in the lattices of i) 15 nm Al_2O_3, ii) 15 nm Al_2O_3 + 8 nm C-PDA and iii) 30 nm Al_2O_3 + 8 nm C-PDA, under 2.61% compression. All three curves show a combination of triangular and rectangular distributions, meaning that both beam bending and node bending exist. Here, the peak UR value in the triangular distribution is then used to represent the extent of beam bending, while the plateau UR value in the uniform distribution is used to represent the extent of node bending. Further the evolution of the UR distribution as the strain increases is plotted in Fig. 3.15d-f.

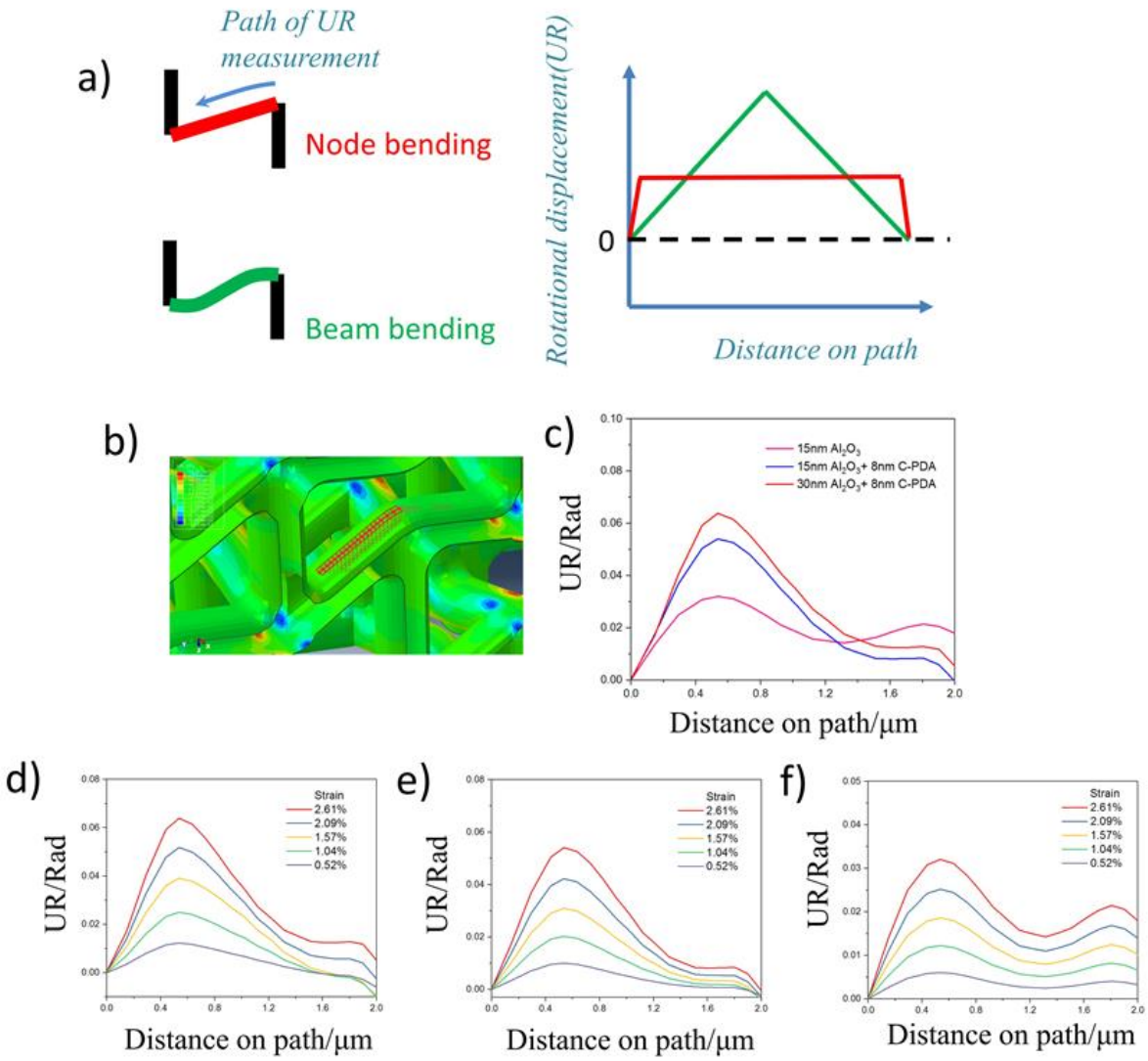

Figure 3.15 a) A schematic showing the different rotational distribution (UR) on a vertical strut between beam bending and node bending. b) The path where the x-axis component of the UR is tracked. c) UR distribution for 3 types of lattices along the path at the compressive strain of 2.61%; d) UR distribution evolution for the 15 nm Al_2O_3 lattice; e) UR distribution evolution for the 15 nm Al_2O_3 +8 nm C-PDA lattice; f) UR distribution evolution for the 30 nm Al_2O_3 +8 nm C-PDA lattice.

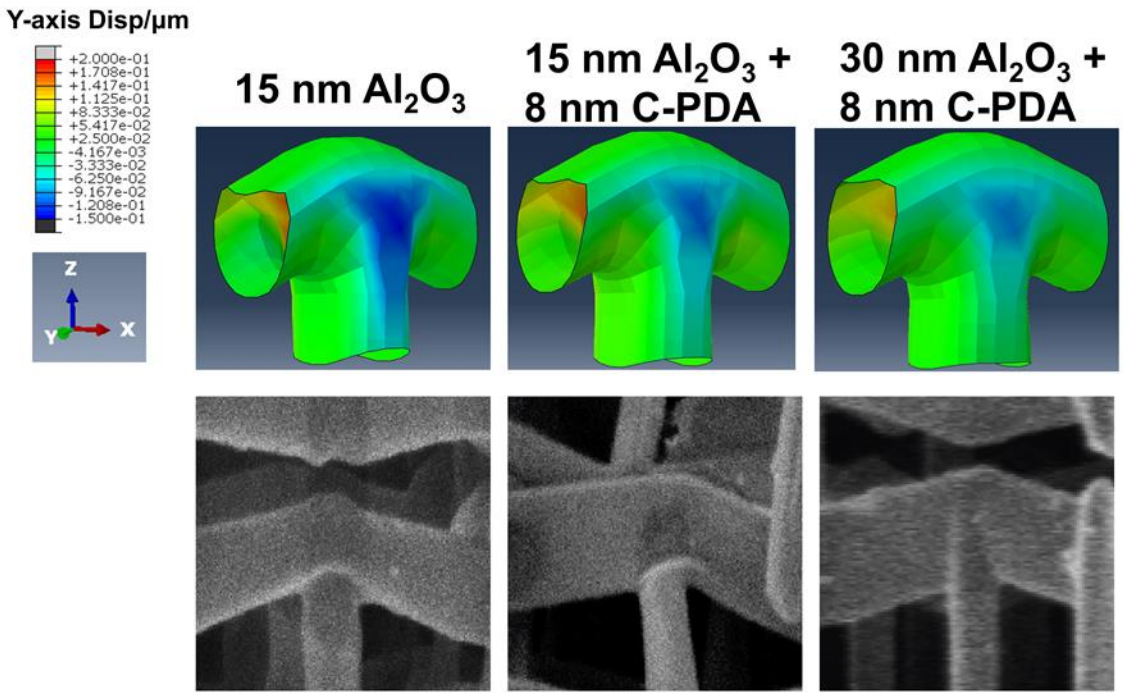

Figure 3.16 The bulging hollow nodes from different lattices are shown. The FEM visualizations are taken from a compression at the strain of 2.61%. Below the FEM results are the corresponding experimental observations of the nodes from different lattices. The SEM images are taken at the compressive strain of 33%.

In Fig. 3.16, the deformation at lattice nodes of B-H-Lattices with three different material configurations are compared with the FEM results. The node bending causes the nodes to bulge in Y-direction, which is perpendicular to the side wall of the nodes. Moreover, comparing the three material configurations (15 nm Al_2O_3, 15 nm Al_2O_3 + 8 nm C-PDA and 30 nm Al_2O_3 + 8 nm C-PDA), the bulging displacement values and the bulged areas of the ceramic/C-PDA composite nodes are significantly smaller than those of the pure ceramic node. For the case of 15 nm Al_2O_3, the ovalized node is obvious. Whereas, in the case of 15 nm Al_2O_3 + 8 nm C-PDA, the deformation at the lattice node is restricted to the end of the inclined vertical strut. In the case of 30 nm Al_2O_3 + 8 nm C-PDA, no deformation at the lattice node is visible. The experimental observation and the FEM results are consistent regarding the extents of node bending across the three material configurations.

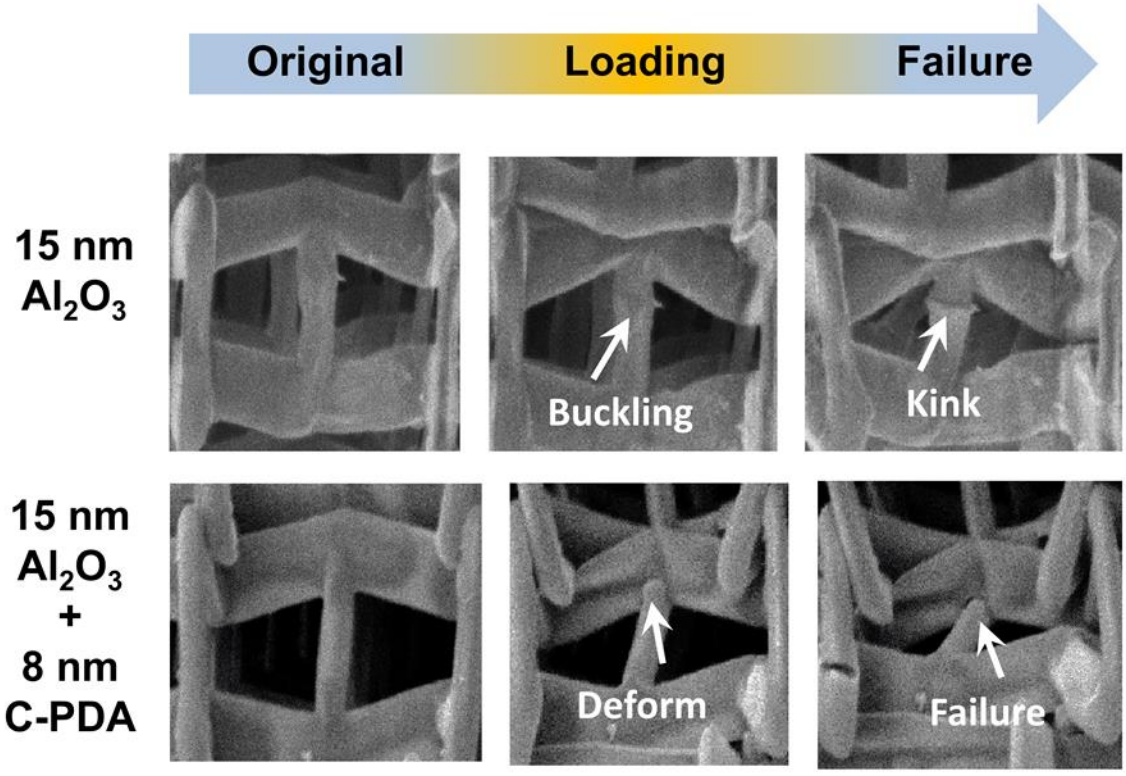

Figure 3.17 Failure at the vertical struts in different lattices are compared. The strut of a ceramic lattice shows bucking and kinking in the middle; while the strut of a composite lattice merely inclines with a crack finally initiated at the spot where the strut is joined with horizontal ones.

Although the bending at the nodes greatly affects the deformation of the lattice, it is not the primary mechanism of the lattice failure. The major failure occurs on the vertical hollow struts, which is parallel to the compression direction. As shown in Fig. 3.17, the failure of the vertical struts from pure ceramic and ceramic/C-PDA B-H-Lattices are compared. In the 15-nm pure ceramic B-H-Lattice, the compressed hollow strut exhibits buckling failure in the middle position initially. With further compression, a kink develops at the buckled position of the strut. This phenomenon is similar to the previously reported stretching dominated hollow alumina structures. In contrast, the hollow strut of the ceramic/C-PDA composite B-H-Lattices does not buckle till the end of the compression. The large compression along Z-direction is accommodated by inclination of the strut. As a result, the failure spots are localized at the joint where vertical struts are connected to horizontal ones. The different failure mechanisms of the ceramic and ceramic/C-PDA B-H-Lattices are caused by their respective mechanical behavior during compression. The

shell buckling of the hollow strut, which is the main failure mechanism of ceramic B-H-Lattices, is suppressed in ceramic/C-PDA B-H-Lattices.

The failure of ceramic/C-PDA B-H-Lattices with thicker (30nm) ceramic nanolayer is not comparable to the aforementioned two types of lattices. The fracture of such lattices occurs at rather random spots. Cracks initiate without any visible local elastic deformations, indicating a typical brittle failure. A through crack is developed along the direction of 45° from the substrate. The SEM observation of the crack development and stress-strain response are shown in Fig. 3.18. Interestingly, at the very early stage of the compression, the lattice can elastically deform by inclination of the vertical struts at the bottom of the lattice. This has never been observed in any ceramic lattices whose hollow struts are made of nanolayers that are thicker than 20 nm. It can be inferred that the C-PDA nanolayer is still playing a role in toughening the 30-nm alumina nanolayer.

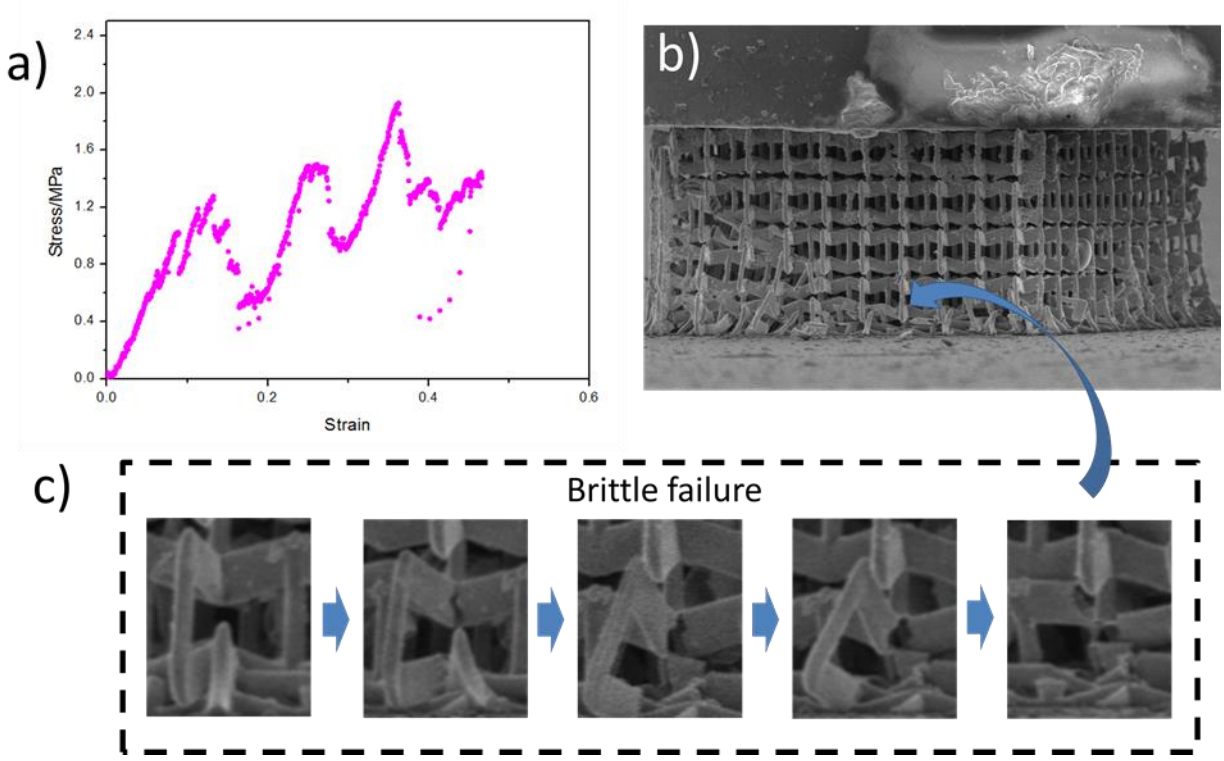

Figure 3.18 Stress-strain curve and failure behavior for 30 nm Al_2O_3 + 8 nm C-PDA lattice. a) Stress-strain of such composite lattice during in-situ SEM compression; b) Overview of the lattice failing in a brittle manner; a through shear plane of failure can be observed; c) evolution of local failure at a node.

3.3.4 Scaling factor in the composite hollow metamaterials

For bending-dominated lattice materials, the modulus is often predicted by the scaling factor of 2:

$$\frac{E}{E_s} \propto \left(\frac{\rho}{\rho_s}\right)^2$$

Such scaling relationship is relying on several assumptions. Firstly, the constituting struts are solid, rendering the relative density of the lattice dictated by the aspect ratio of the struts. Secondly, ideal bending is the only way of deformation in the bending dominated lattices. These assumptions are no longer practical in hollow lattices. Therefore, the scaling relationship should be reconsidered. If we only consider ideal bending in B-H-Lattices with varied wall thicknesses, the effective modulus will follow

$$\frac{E}{E_s} \propto \frac{\rho}{\rho_s}$$

Similar relationship of strength over density has been reported in the case of hollow lattices yielding (Valdevit et al. 2013). However, linear scaling in single-order hollow lattices has not been achieved so far in any report. This means that factors such as node bending followed by node deformation are deteriorating the overall scaling factor of the microlattice materials.

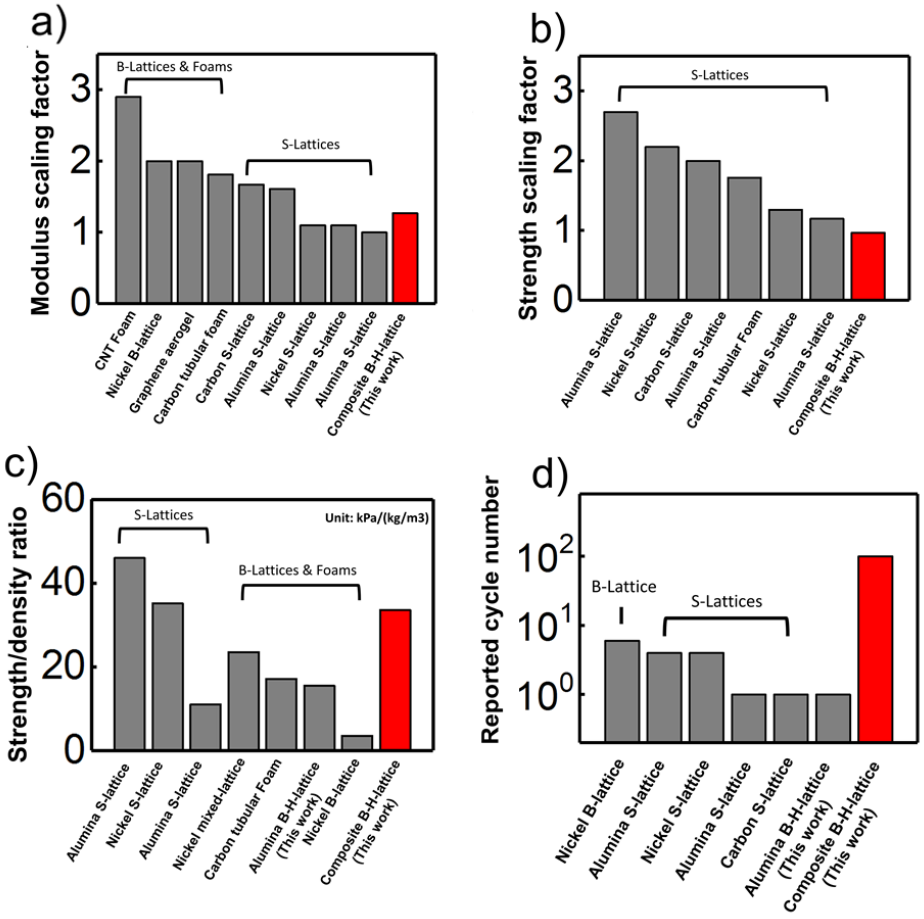

Figure 3.19 a) The histogram is showing the modulus scaling factors of different cellular materials. b) The histogram is showing the strength scaling factors of different cellular materials. c) The histogram is showing the strength over mass density ratio of different cellular materials. d) The histogram is showing the reported cyclic ability of different cellular materials. The density range is chosen as 10-100 kg/m^3.

The modulus scaling factor and strength/density ratio of the ceramic/C-PDA B-H-Lattices are delineated from the stress-strain relationship during flat punch indentation. Based on the measured modulus and strength values of the lattices, the modulus scaling factor is 1.27, the strength scaling factor is 0.97 and the strength/density ratio is 33.6 kPa·kg-1·m3. Such close-to-ideal scaling factor and high strength/density ratio have only been previously reported in stretching dominated materials, but not in any bending dominated materials. The superior property in the B-H-Lattices is mainly due to and coupling of ceramic and C-PDA nanolayers, which suppress the node bending and strut buckling during deformation. In Fig. 3.19, the modulus/strength scaling

factor, strength/density ratio of the composite B-H-Lattices, are compared with other lattices and cellulose materials. The modulus/strength scaling factor of the ceramic/C-PDA B-H-Lattices are the closest to 1 among all of the structures, and comparable with the stretching dominated lattices S-Lattices. In the density range of 10-100 kg/m3, the strength/density ratio of the ceramic/C-PDA B-H-Lattice is also reaching the values of the best S-Lattices, higher than foams, B-lattices and stretching-bending mixed mode lattices. In the meantime, the cyclability of the ceramic/C-PDA B-H-Lattices in this work is highest among all the current nanolattices. While most the of the nano-lattices survives for only 1-4 cycles, including S-Lattices (alumina, nickel, carbon) and B-Lattices (nickel and alumina-B-H-Lattice in this study), the ceramic/C-PDA B-H-Lattices shows much superior recoverability after 100 of cycles under 5-15% strains. The reported cycling numbers of the composite B-H-Lattices here are not as high as that of carbon foams, the modulus and strength of these B-H-lattices, their scaling factors and strength/density are much superior due to the structure and materials design. In Fig. 3.20a, the effective modulus of the composite B-H-Lattices is compared to the existing highly recoverable carbon-based foams (Bi et al. 2015; Worsley et al. 2009; Q. Zhang et al. 2016; Zhu et al. 2015). By introducing a strongly coupled ceramic/C-PDA nanolayers to B-H-Lattices, the modulus/mass efficiency is elevated above 106 Pa/(kg·m-3), which is much superior to the pure carbon-based foams. It is worth noting that the recoverability of such carbon foams come from planar or shell buckling, while the recovery of the composite B-H-Lattices comes from elastic deformation of the composite hollow lattice nodes. Such difference results in a difference in the scaling factors. For most carbon-based foams, their modulus scaling factors are larger than 2, while for the composite B-H-Lattice it is near to 1.

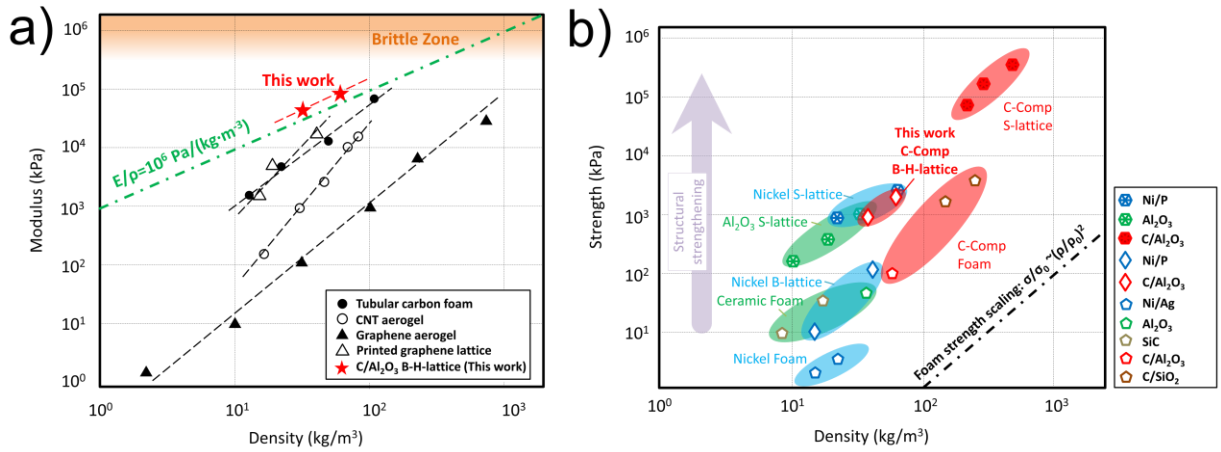

Figure 3.20 a) Compared to other carbon-based cellular foams, the composite hollow lattices in this work have a modulus to density ratio over 10^6 Pa/(kg·m^{-3}); b) Ceramic, metal, carbon composite cellular materials are summarized into three categories: i) foams; ii) bending dominated lattices (B-lattices); iii) stretching dominated lattices (S-lattices). The sequence of strength is typically 'Foam < B-lattices < S-lattices'. The composite B-lattices in this work are nearly matching metal or ceramic S-lattices from in strength at similar mass densities.

In Fig. 3.20b, the most typical cellular structures made of ceramic, metal and carbon composite reported so far are compared regarding their strength. The trend of structural strengthening effect can be clearly seen for metal, ceramic, carbon composite cellular materials respectively. Three main types of cellular structure are included in this Ashby plot: foams, B-lattices and S-lattices. Generally, at a certain mass density (10-100 kg/m3 in this paper), strengths of ceramic and metal cellular materials follow: Foam (Chabi et al. 2016; B. Jiang et al. 2015; Poco, Satcher, and Hrubesh 2001) < B-Lattice < S-Lattice. This is due to the structural strengthening effect, which is the baseline of all the currently designed ultra-strong lattice materials. It can be seen from the plot that the composite B-H-Lattice in this work nearly matches the strength of S-Lattice of metal and ceramic at similar mass densities. On the other hand, carbon composite cellular structures in such light-weight regime come with interior strength. Although existing carbon composite foams (Moner-Girona et al. 2002) and solid lattices already exhibit outstanding mechanical strength, their mass density is approximately an order higher, and they are faced with brittle failure. In this work, by making ceramic/C-PDA composite B-H-Lattices, node bending and strut buckling can be suppressed. This non-buckling B-H-Lattices provide a path-finding concept for the next generation reliable and robust mechanical metamaterials.

3.4 Conclusion

A unique ceramic/C-PDA nanolayered composite bending dominated hollow lattice (B-H-lattice) is developed for the first time, with recoverability, high strength/weight ratio, zero Poisson ratio, optimal scaling factor and good cyclic performance. The deformation behavior of the ceramic hollow lattices is changed significantly by coherently depositing a few nanometers of carbonized mussel-inspired bio-polymer (C-PDA). While the deformation of the pure ceramic lattice is dominated by buckling, such failure mechanism is significantly suppressed in the composite B-H-lattice. In the meantime, despite the buckling-recovery behavior of the pure ceramic lattices, the composite B-H-lattices have a new recovery mechanism of elastic node deformation while node bending is suppressed. The recoverable strain reaches 55%. Furthermore, the composite B-H-lattice shows stable cyclic loading behavior under up to 15% strain. Such non-localized deformation/recovery/cyclability have not been observed before in any B-Lattices or S-Lattices ceramic metamaterials. In terms of scaling factors and strength/density ratio, the ceramic/C-PDA B-H-Lattice outperform most of the nano-carbon based cellulose structures and B-Lattice metamaterials, and comparable to those of the S-Lattice metamaterials. This suggests that suppressing node bending and strut buckling in composite B-H-Lattice are the key factors to improve the mechanical performances of nanolattice metamaterials. This metamaterial concept can be extended to many mechanical systems that demand reliable and robust metamaterials, leading to a variety of devices with properties previously considered impossible.

4. MECHANICAL PROPERTIES OF TRIPLY PERIODIC MINIMAL SURFACES AND THEIR EXTENDED DERIVITIVES

4.1 Introduction

Triply periodic minimal surfaces (TPMSs) are surfaces which are periodic in all XYZ directions and have minimized areas under a certain bounding rule. In fact, the early mathematic problem concerning minimal surfaces, the '*Plateau Problem*', is named after the Belgian physicist J.A.F. Plateau who studied the problem experimentally through observing soap films during the 19th century (Plateau 1873). This problem is asking to find or prove the existence of a minimal surface with a given boundary curve. Another version of minimal surface problem is '*free-boundary problem*', in which the boundary curve is restricted to lie on a given plane while being able to move if the surface area is not minimized. While these mathematical problems can be extremely complicated to solve for analytical solutions, introducing symmetry to minimal surfaces make them much accessible to be constructed and studied. After the pioneer studies (Schoen 1970) in 1970s, discovering many types of TPMSs based on their corresponded crystallographic symmetry, the existence of Schoen's surfaces was proven using a conjugate surface method (Karcher and Polthier 1996). This method provided means for computational discrete methods to construct surfaces in the '*free-boundary problem*' with planar symmetry. The discovery and studies of TPMSs, which have high symmetry throughout the 3D space, have drawn more and more attention while researchers are finding their counterparts in nature materials and exploring their applications in many fields (L. Han and Che 2018).

In recent years, as the 3D printing technology advances, light-weight periodic porous structures are becoming easier to realize (Surjadi et al. 2019). With metals, ceramics or polymers, researchers are designing architected materials with exceptional mechanical properties. Many of these designs are categorized as new mechanical metamaterials (Zadpoor 2016), since it fills the blank areas in an Ashby plot, where various materials are coordinated with their mass density and modulus/strength (Ashby 2006). Some outstanding examples are solid lattice materials, hollow lattice material and shellular materials. Interestingly, solid lattice materials and shellular materials have been compared for their potential to reach Hashin-Shtrikman upper bounds of elastic stiffness (Berger, Wadley, and McMeeking 2017). Shellular materials, which are composed of membranes, are the more promising candidates. In the meantime, hollow lattices exhibit outstanding and

unconventional properties like high stiffness with high recovery under large loading. This significantly distinguish hollow lattice materials from solid lattice materials despite their similar shapes or symmetries. Although novel structured materials are designed, fabricated and proven to have promising capabilities, the optimal strategies to build light-weight yet stiff mechanical metamaterials remain elusive. In many recent works, TPMSs are introduced as one of the promising candidates for providing high stiffness, strength and energy absorbing capability. These TPMS structures have been made in metals and polymeric resins. However, little has been provided to link their geometrical uniqueness to their outstanding mechanical properties.

Speaking from a mathematical perspective, TPMSs has many unique properties. The first and most identifying geometrical feature is the mean zero curvature across the entire surface. As shown below, κ_1 and κ_2 are the maximum and minimal of the curvatures at a given location.

$$H = \kappa_1 + \kappa_2 = 0$$

When we are assigning a solid shell to the TPMS geometry, it is natural to think that it has a unique mechanical property that is directly related to the mean zero curvature. For an arbitrary small element surface under (biaxial) tension, the mean curvature is tending to decrease. In the case of TPMSs, their mean curvature is already zero. Therefore, it is reasonable to argue that the TPMSs will retain their local curvature under isotropic tension. In light of this guess, the first purpose of this chapter is to sort out these geometry-determined mechanical behaviors, and further present the accurate description for which the TPMSs are optimal with respect to a given mechanical property. Then we will compare the TPMSs to the hollow lattices, which is also bounded by crystallographic symmetries and unique local curvatures as 3D periodic structures constructed by merely thin shells. Such comparison will be discussed towards a better understanding of the principles on designing shell-dominated mechanical metamaterials.

4.2 Methodology

4.2.1 Construction of TPMS

The accurate construction of TPMS is potentially difficult despite its simple local mean zero curvature definition. Although some TPMSs can be approximated by certain trigonometrical forms, for example, gyroid is similar to the surface described by $sinxcosy + sinycosz + sinzcosx = 0$; the rest can be very difficult to parameterize. It becomes a crucial matter to have

the necessarily accurate geometry, when we either run numerical simulations or conduct 3D printing jobs, to further probe the connections between the mechanical behaviors or TPMS shells and their geometrical characteristics, such as local mean zero curvatures.

Here, we use the software Surface Evolver to solve for TPMSs with different crystallographic symmetries. Typically, only the irreducible unit surface of the TPMS, instead of the entire unit cell of the TPMS is solved. Due to the high symmetry of TPMSs, the irreducible unit surface can be down to 1/96 of the entire unit cell. The output surface from Surface Evolver is divided into many connected triangles. The arrangement of these triangles can be optimized. As mentioned in the introduction, a conjugate surface method can be used to transform the construction of TPMS, a *free-boundary problem* usually bounded by faces of a cube, into a corresponding '*Plateau problem*', which can be approached by discrete computational methods. The optimally arranged triangles either construct the TPMS directly or can be transformed to the targeted TPMS by the conjugate method algorism. The derived surfaces can then be exported to Autocad, and readily used in further numerical simulations or 3D printing models.

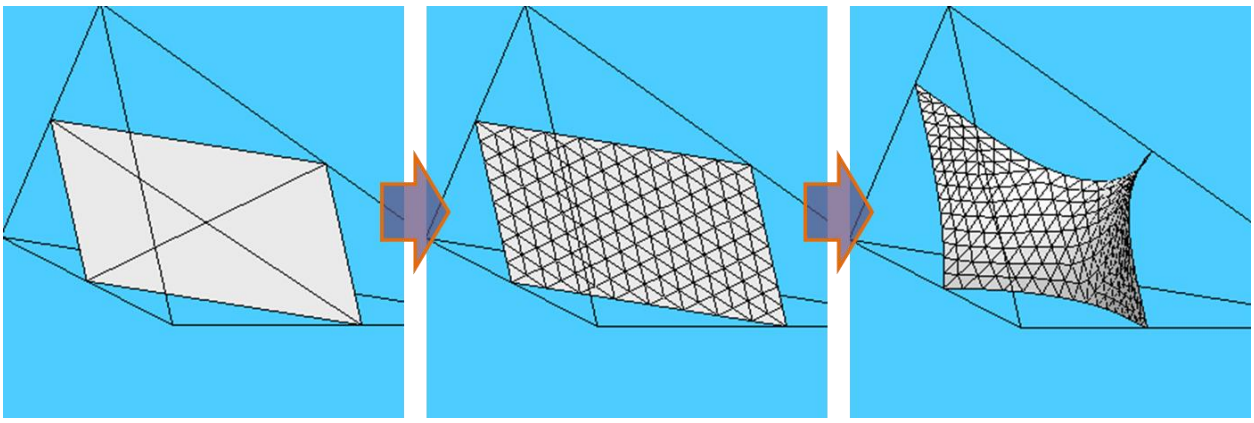

Figure 4.1 Schematic of the optimization process of Surface Evolver for the irreducible unit surface of targeted TPMS (IWP surface).

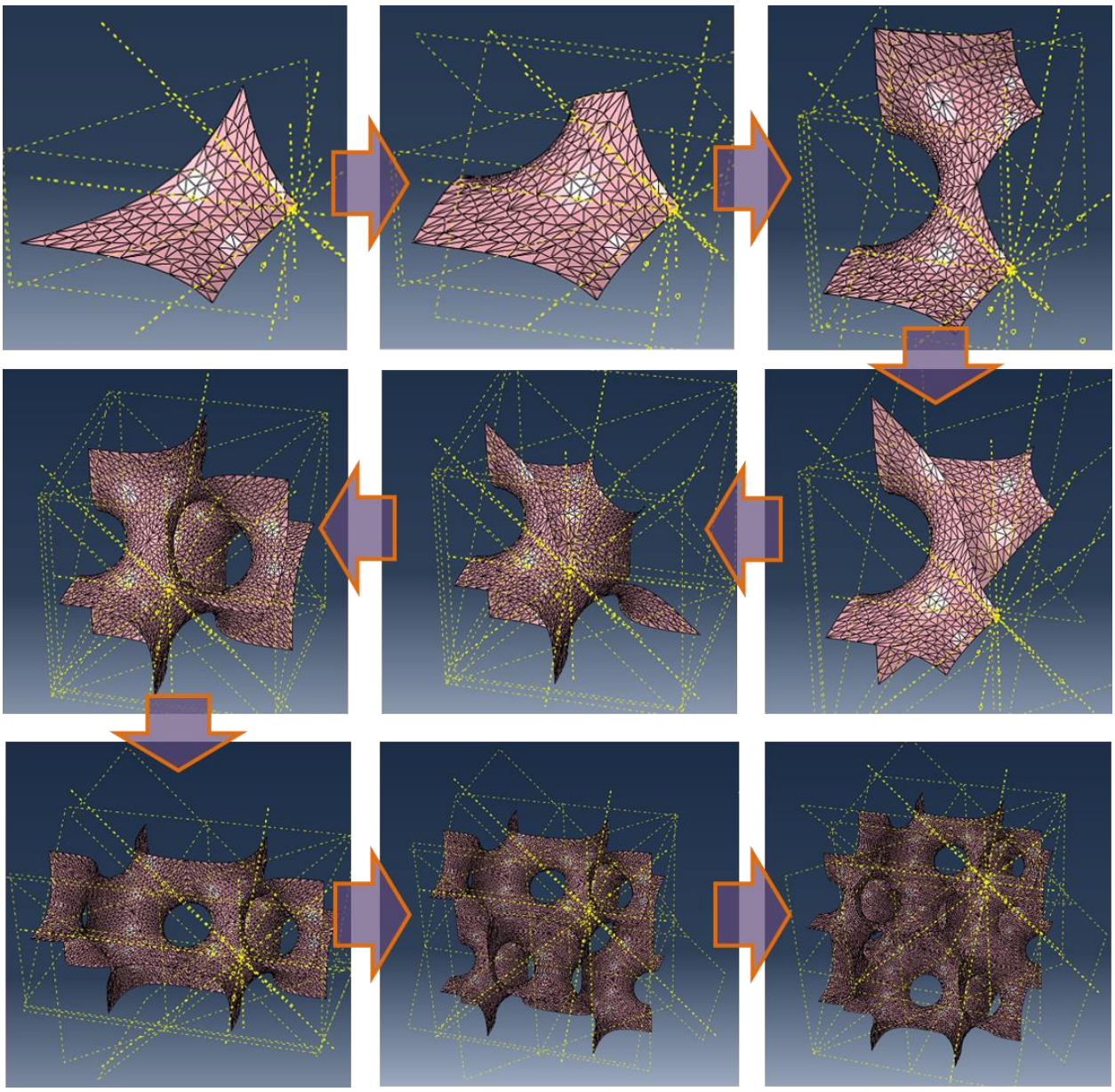

Figure 4.2 Expanding the irreducible element surface of the TPMS (FRD surface) to a full unit cell by mirroring operation in a selected sequence.

4.2.2 Numerical simulation

Numerical simulation is conducted to study the static via TPMS shells. Commercial FEM software Abaqus is used. The geometrical data of the irreducible unit surface of the TPMS derived from Surface Evolver is imported and expanded to a full unit cell by translation, rotation and mirroring operations. Typically, we use conventional shell elements (S4R or S8R) to simulation the TPMS

shell. We choose shell elements for two reasons. Firstly, the thickness to unit-cell length ratios of the TPMSs of interests are set to be 1/20. With such low aspect ratio, shell bending is the predominant behavior. Secondly, using solid elements could render the computation extremely costly, since a necessary number of element layers need to be established throughout the thickness. The material used in the simulation is from 3D printing resins. Their mechanical property is set to be ideally elastic. Since the interested mechanical properties, such as the stiffness and wave propagation properties do not concern the ultimate yielding or failure of these structures. Also, since the thickness to unit-cell length ratio is very low, a significant deformation mechanism is shell bending or buckling, which can be adequately described within the elastic range of 3D printed polymers. In the static or dynamic model, periodic boundary conditions are typically implemented. The intrinsic Poisson's ratio of the materials is set to be 0.24. For each of the TPMS shell models, we applied different types of deformations to probe their bulk modulus *K*, shear modulus *G* and Young's modulus *E*.

For any structure with cubic symmetry placed in the orientation where the xyz axes is parallel to the [100], [010] and [001] direction, their compliance tensors should follow the form below:

$$\begin{pmatrix} S_{11} & S_{12} & S_{12} & 0 & 0 & 0 \\ S_{12} & S_{11} & S_{12} & 0 & 0 & 0 \\ S_{12} & S_{12} & S_{11} & 0 & 0 & 0 \\ 0 & 0 & 0 & S_{44} & 0 & 0 \\ 0 & 0 & 0 & 0 & S_{44} & 0 \\ 0 & 0 & 0 & 0 & 0 & S_{44} \end{pmatrix}$$

Here, we should have

$$S_{11} = \frac{1}{E}$$

$$S_{12} = -\frac{3K - E}{6KE}$$

$$S_{44} = \frac{1}{G}$$

With the 3 mechanical responses we probe from the numerical model, we can calculate the complete compliance tensor of a properly orientated TPMS shells. Furthermore, we will be able to obtain the full information of the mechanical an-isotropy of the TPMS shells.

4.2.3 3D printing and mechanical measurement

The TPMS shells are printed by an FDM 3D printer, Prusa i3 MK3 with MMU2. The parts are printed with standard PLA filament of 1.75 diameter. The nozzle size is 0.4 mm. The 3D model is comprised in STL file and sliced to layers of 2D shapes (thickness: 0.2 mm) along the height of the part. These 2D shapes consisted of perimeters and fills are converted to vectors that can be realized by the step motors in the printer. During printing, the filament is fed to a heated nozzle at a constant speed, which is controlled by a motorized gear. The nozzle temperature is 205 °C and the build bed is heated to 60 °C. Eventually, the completed TPMS samples will be removed from the build bed by flexing the removable steel build bed.

The parts produced in this work is derived from thickening the TPMSs. The thickness of the shell for all samples are fixed to 0.75 mm. This thickness setup ensures at least two layers of perimeters to be generated for a standalone shell. The length of the unit cell is fixed to 20 mm. Each sample consists of 18 unit cells arranged in 2 stacks of 3x3 arrays. Therefore, the samples is 60 mm in length and width, 40 mm in height. In order to stably print out the samples, four outer walls of the same thickness are added to the left, right, front and back of the TPMS as supports at the side boundaries. Without the supporting walls, messy side edges would be generated, which eventually will cause the failure of the printing. The top and bottom of the sample do not need support. Typical build time of each samples is 4-8 hours depending on the complexity and density of the sample.

The mechanical property of 3D printed TPMS shell samples are measured by the compression tests via an MTS uniaxial tester with maximum load of 22000 N. The loading rate of the compression test is set to 0.4 mm/s and the cutoff displacement is set to 3 mm. The elastic stiffness of the structure is then obtained through the output force-displacement data.

4.3 Results and discussion

4.3.1 TPMSs and their symmetry

Before we start to probe the mechanical properties of TPMSs, it is necessary to select different types of TPMSs in the scope of this work and summarize them based on their symmetries. For a better demonstration of the mechanical uniqueness of TPMS shells, we also include hollow lattice structures of the same symmetries as the contrast group of TPMS shells. As shown in Fig. 4.3, we

put together five types of TPMSs and their corresponding hollow lattices with varied aspect ratios. The selected TPMSs are gyroid surface, Schwarz P (SP) surface, Schwarz D (SD) surface, Scheon's I-graph-Wrapped Package graph (IWP) surface and Scheon's F-graph-Rhombic dodecahedra graph (FRD) surface. Among these TPMSs, SP surface corresponds to simple cubic symmetry; SD surface corresponds to diamond symmetry; IWP surface corresponds to body-centered cubic (BCC) symmetry; and FRD surface corresponds to face-centered cubic (FCC) symmetry. Gyroid surface does not have planes of symmetry; but it has C3 axes and 4-fold rotoinversion axes. The varied aspect ratios of the corresponding hollow lattices, to be more specific, their strut diameter to unit cell length ratios, provide different surface area per volume for these structures, listed in **Tab. 4.1**. These values are further used in calculation of the specific mechanical properties to provide a more accurate contrast.

Table 4.1 Area per volume for each of the shell models. Unit cell length: 2 m; Unit: m^{-1}

	TPMS	*HL-1*	*HL-2*	*HL-3*	*HL-4*	*HL-5*
Gyroid	1.550	0.805	1.100	1.365	1.516	1.552
SP	1.173	0.987	1.131	1.197	1.174	1.084
SD	1.921	1.274	1.544	1.742	1.878	1.925
IWP	1.735	1.099	1.595	1.841	1.742	1.420
FRD	2.421	1.877	2.354	2.644	2.660	2.413

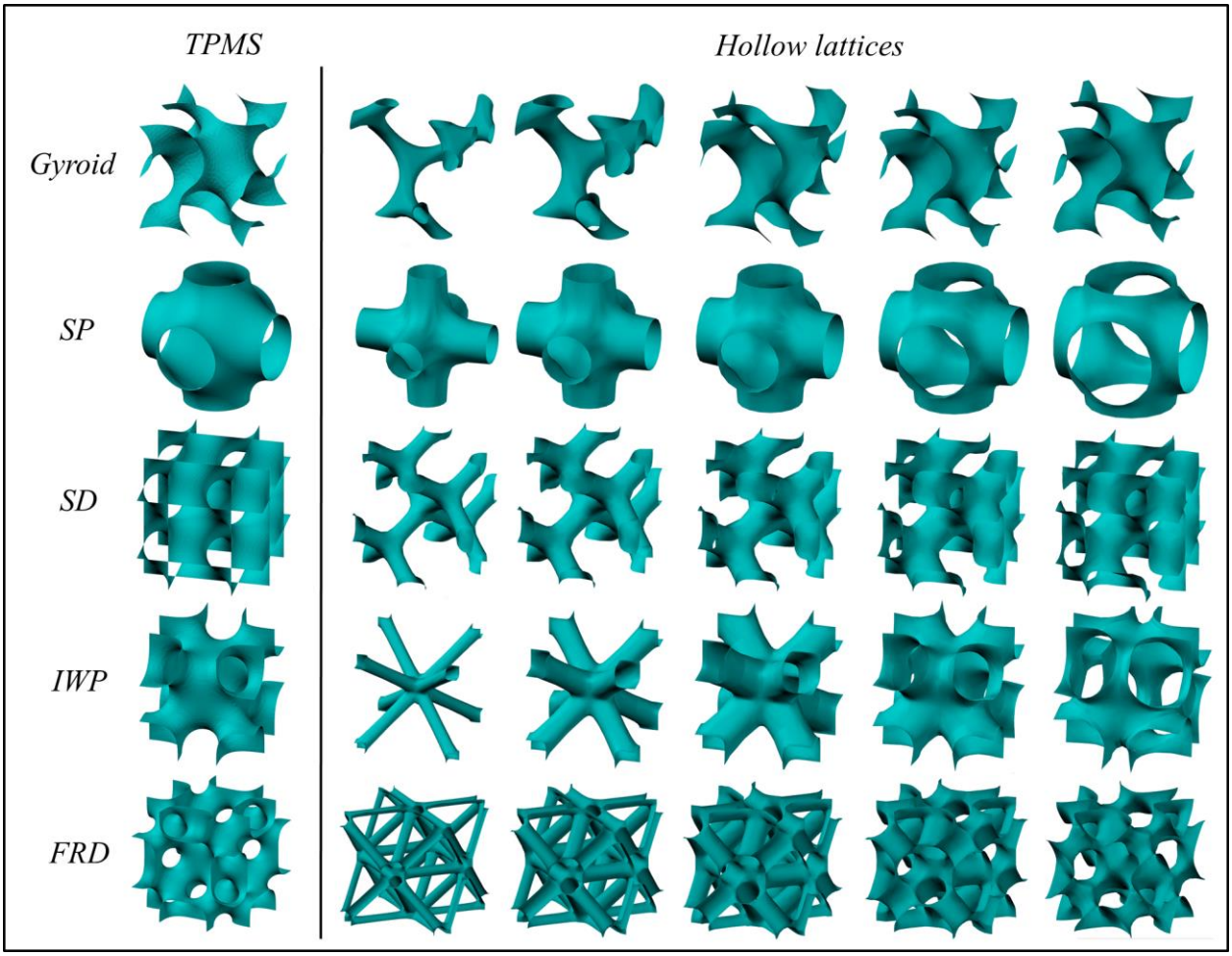

Figure 4.3 Five types of TPMS shells and their corresponding hollow lattices of the same symmetry with varied aspect ratios.

4.3.2 Bulk modulus of TPMS shells

The upper limit of the effective bulk modulus of multiphase materials was derived as the Hashin-Shtrikman upper bound in the 1960s. The derivation involved the calculation of the maximum elastic energy via a variational approach. Meanwhile, it was not directly specified what strain energy distribution should be required in order to reach the upper bound of the effective bulk modulus of multiphase materials, or to be more specific, two-phase materials. Many researchers proposed periodic structures that reach or approach the Hashin-Shtrikman upper bound. Yet the strain energy distribution of these proposed structures has not been discussed thoroughly or linked to their superior mechanical behavior.

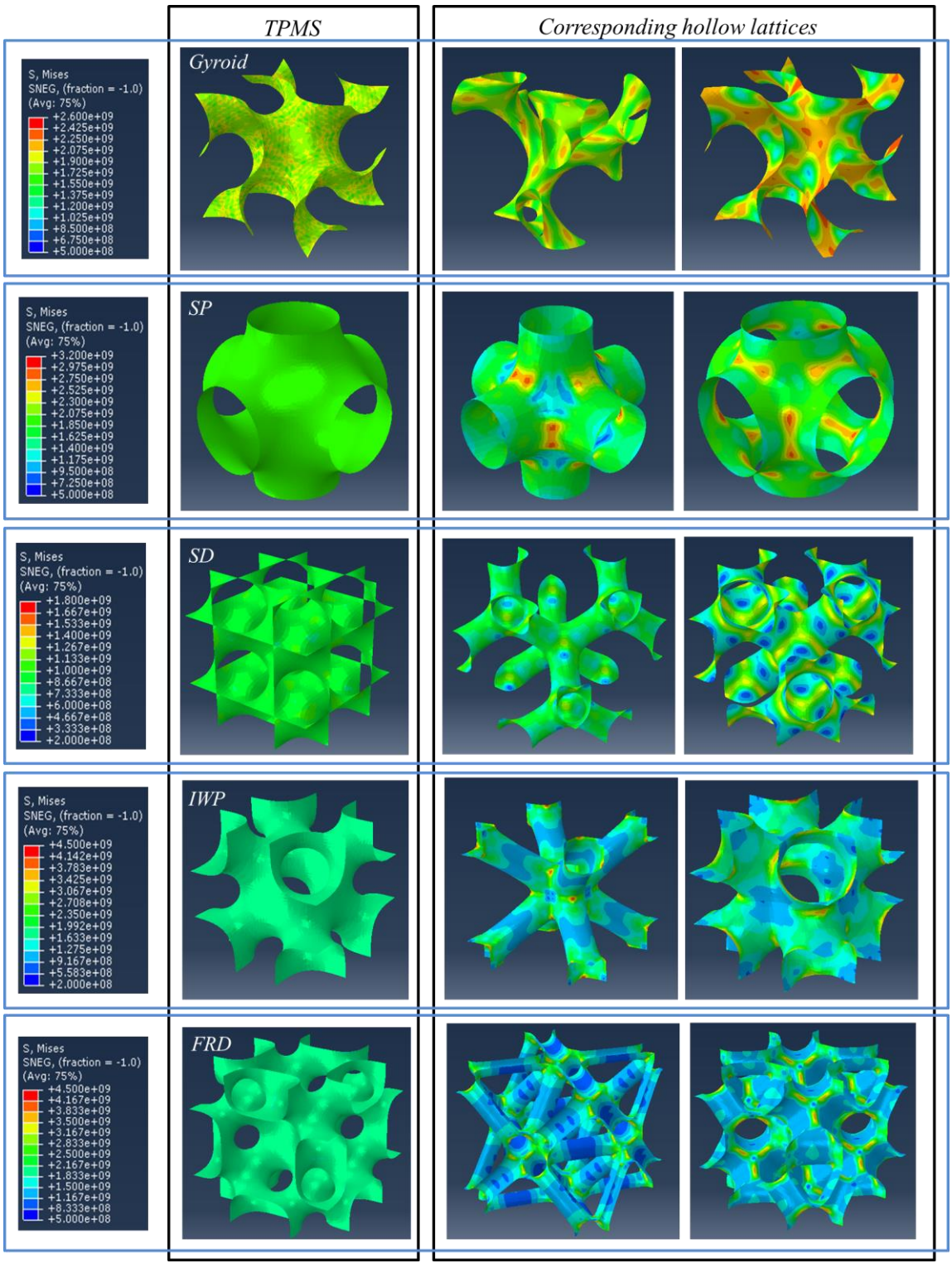

Figure 4.4 Comparison of the stress concentration extents between various TPMS shells and their corresponding hollow lattices of the same symmetries under the deformation of hydrostatic tension. The strains over xyz directions are 0.8% respectively.

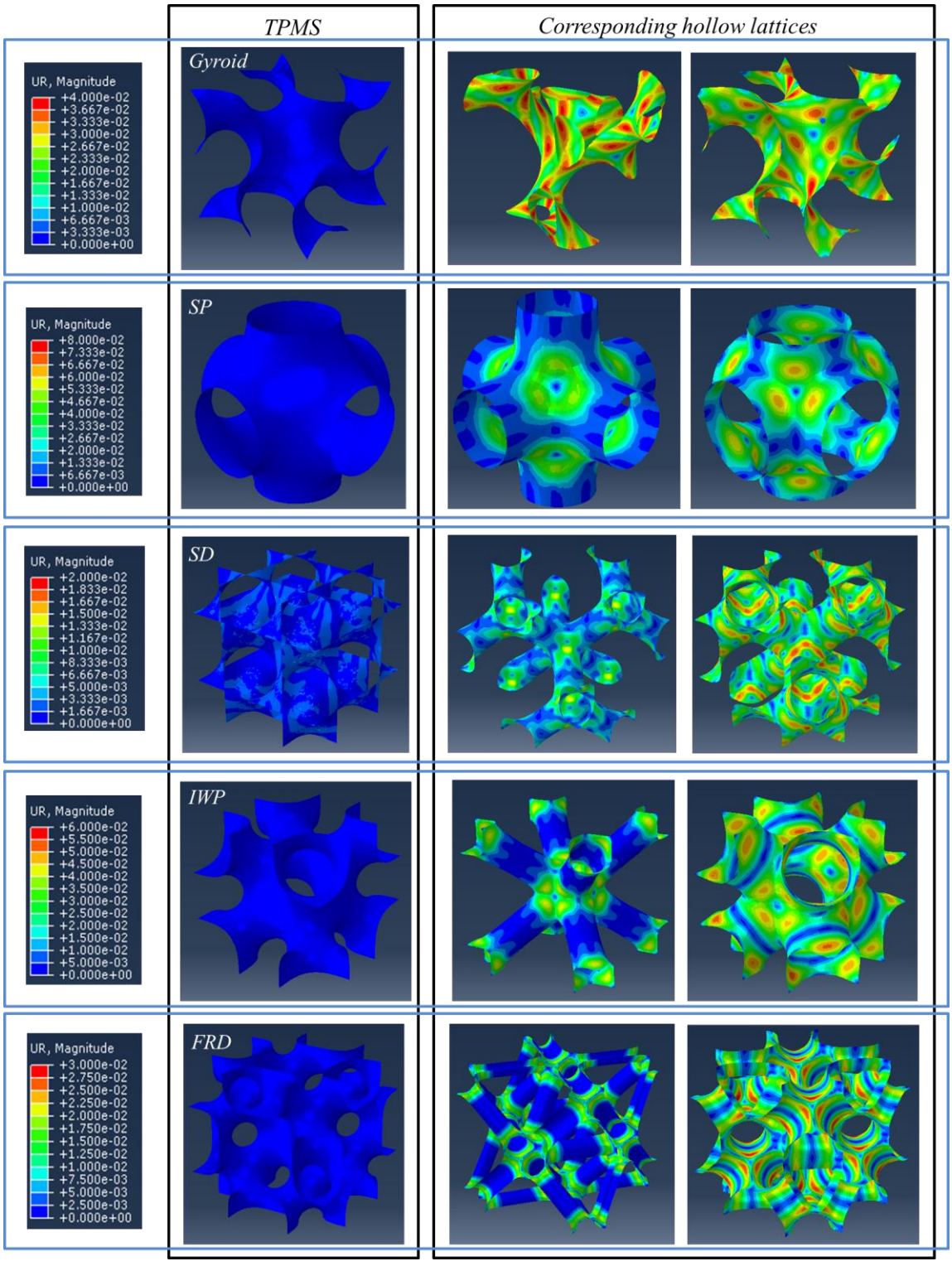

Figure 4.5 Comparison of the rotational displacement (bending) between various TPMS shells and their corresponding hollow lattices of the same symmetries under the deformation of hydrostatic tension. The strains over xyz directions are 0.8% respectively.

Here, we will first examine the hypothesis that the crucial geometrical feature, the local curvatures, of TPMS shells will retain under the deformation of hydrostatic tension. Such hydrostatic tension is concurrently the simulated deformation for the measurement of bulk modulus. Fig. 4.4 and Fig. 4.5 show the stress and rotational displacement distributions of various TPMS shells under hydrostatic tension and compare them with their corresponding hollow lattices with the same symmetries. It can be seen that on the TPMS shells, the Mises stress is globally uniform across the unit cell of the TPMS shells. Some minor stress concentrations are observed if the scale range narrows to smaller numbers. The minor stress concentrations can be attributed to the geometrical error introduced when the TPMS model is expanded by the mirroring and stitching operation in the numerical software. Because the locations of the stress concentrations are well aligned with the intersections of the TPMS and its mirror planes. Also, the rotational displacement field during the hydrostatic tension shows that, at every location on the TPMS shells, the rotational displacement is close to zero. This means that bending is nearly non-existent during the hydrostatic tension of the TPMS shells; thus, the geometries of shells are simply scaling up without any distortion. However, when we examine the hydrostatic tensions for the corresponding hollow lattices of the five TPMS shells, the stress concentrations are significantly accumulated on specific locations of the shells. For most cases, the stress concentrations occur at the connecting nodes where hollow struts join. In the case of gyroid-like hollow lattices, where the hollow struts are much slenderer than the connecting nodes, stress concentrations can occur in the middle of the hollow struts. Simultaneously, the rotational displacement field of the hollow lattices under hydrostatic tension often are showing varied values across the geometry. In another word, the geometry of the hollow lattice is distorted despite that the imposed tension is isotropic. In specific, the connecting nodes often expanded in size, while the hollow struts remain with minimal shape change. It is reasonable to infer that the uniform stress and geometrical scaling of TPMSs during hydrostatic tension is closely related to their mean zero curvature. It can be further judged that such mechanical response during hydrostatic tension should be exclusively attributed to TPMS shells if we only consider embedded surfaces, who do not present self-intersections.

The mechanical behavior of TPMS shells during isotropic tension can be further interpreted from the perspective of how the elastic energy are stored. For thin shells, the stored elastic energy can be split into two separate parts. One concerns the stretching of the shell; and the other concerns the bending of the shell. Typically, given the same displacement, the stored energy in stretching is

significantly higher than the stored energy in bending due to the low bending stiffness of the thin shell. In this sense, when the TPMS is under hydrostatic tension, the elastic energy is entirely stored in a stretching manner, since there is no local curvature change. Because of this, we here reasonably note the TPMSs as "stretching dominated surfaces". It is naturally that storing elastic energy in a stretching manner is a more efficient way compared to storing elastic energy in a bending manner towards higher bulk moduli. In fact, it is reasonable that the geometries of TPMSs towards maximum bulk modulus represent local optima among all shell structures if not equally the global one.

Fig. 4.6 displays the calculated bulk moduli and the specific bulk moduli of the 5 TPMS shells and their corresponding hollow lattices. In all cases, the TPMS shells have higher bulk moduli compared to their hollow lattice count-parts of the same volume densities. Moreover, the calculated bulk moduli of TPMS shells scale linearly with the thickness or the volume density of the shells. However, the bulk moduli of the hollow lattices do not scale linearly with the thickness or volume density of the structure. Instead, their scaling factor is larger than 1. This result confirms that the TPMS shells are behaving as 'stretching dominated surfaces' when loaded with hydrostatic pressures. And such stretching nature is absent with all the hollow lattices under the same circumstance. In fact, it is obviously impossible to deform hollow lattices in a pure stretching manner with any loads applied only on the boarders of a unit cell.

In the meantime, the bulk moduli of TPMS shells are compared to the Hashin-Shtrikman upper bound for the bulk moduli of two-phase materials, defined by the equation below.

$$K_{HS+} = K_2 + \frac{1 - v_2}{\frac{1}{K_1 - K_2} + \frac{3v_2}{3K_2 + 4G_2}}$$

Here K_2 and G_2 are the bulk modulus and shear modulus of the solid phase in the shell structure; K_1 is the bulk modulus of the air within the shell structure, which is set to be zero; v_2 represent the volumetric density of the solid phase.

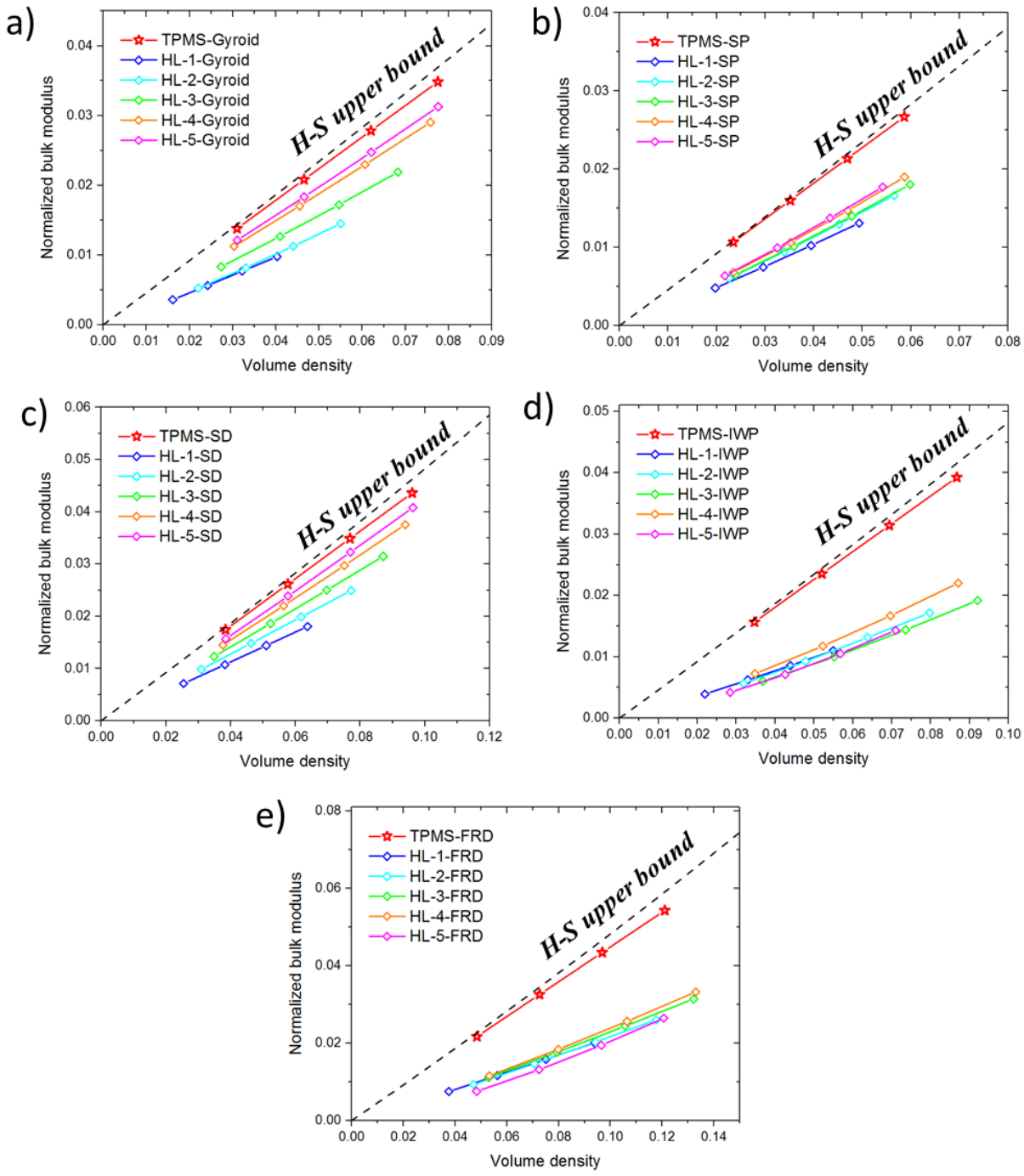

Figure 4.6 The normalized bulk modulus for TPMSs and HLs of different symmetries. a) Gyoid TPMSs and gyroid-HLs; b) SP TPMSs and SP-HLs (same as SC HLs); c) SD TPMSs and SD-HLs; d) IWP TPMSs and IWP-HLs (same as BCC HLs); e) FRD TPMSs and FRD-HLs (same as FCC HLs). Black dashed lines represent the H-S upper bounds. The thickness to unit cell length ratios of examined TPMSs and HLs are 0.01, 0.015, 0.02 and 0.025.

It can be seen that the bulk moduli are slightly lower than the Hashin-Shtrikman upper bound. As the volume density increases, the gap between the bulk moduli of TPMS shells and the Hashin-Shtrikman upper bound become larger. This is because while the bulk moduli of TPMS shells scales linearly, the Hashin-Shtrikman upper bound is not linear; as the volume density increases, the slope of the bound increases. In other words, the minimum slope of the bound rest at the zero point. The slope value at the zero point stands for the specific bulk modulus at the point. This means the minimum specific bulk modulus along the Hashin-Shtrikman upper bound is at its zero point. On the other hand, because the bulk moduli of TPMS shells scales linearly with its volume density, the specific bulk moduli of all TPMS shells are equaling the same value. This value should be no larger than the minimum specific bulk modulus along the Hashin-Shtrikman upper bound, otherwise the bulk modulus of TPMS shells could exceed the Hashin-Shtrikman upper bound near the zero point. We compared the specific bulk moduli of TPMS shells and all the hollow lattices counter parts to the specific bulk modulus at the zero point along the Hashin-Shtrikman upper bound. In Fig. 4.7, we can see that only the TPMS shells have specific bulk moduli that approach such limit defined by the Hashin-Shtrikman upper bound. The specific bulk moduli of the TPMS shells are less than 2% lower than the upper limit. We can attribute such difference to the geometry errors of the numerical model.

In sum, these results show that thin TPMS shells are among the optimal shell structure designs to maximize the specific bulk moduli. And they are exclusively optimal shell structures towards maximum bulk moduli among the shells with embedded surfaces.

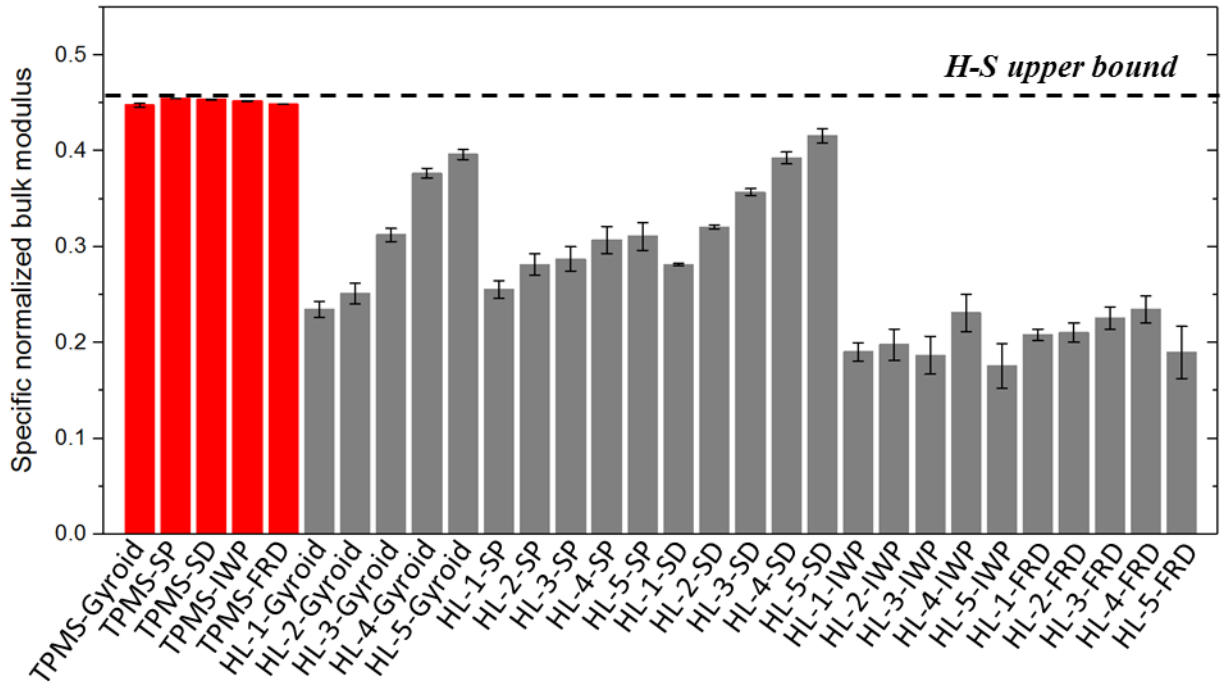

Figure 4.7 Specific normalized bulk modulus for all the numerically examined structures (HLs and TPMSs) in this work. The specific bulk modulus is calculated based on the volume density.

4.3.3 Elastic an-isotropy of TPMS shells

In many research works and many real-life applications, structures are often challenged under uniaxial tension or compression. Although TPMSs are proven to be superior under hydrostatic deformation, it is also important to understand whether they can outperform other shell structures, like hollow lattices in other manners of deformation. For structures with cubic symmetries, it can be mechanically an-isotropic if the following equation is not met:

$$G = \frac{3KE}{9K - E}$$

It has been already discovered that many shell structures with cubic symmetries are not isotropic. Here we further probe the Young's moduli G and the shear moduli E to evaluate the possible an-isotropy of the TPMS shells.

When we calculate the mechanical properties, for example, the Young's modulus along different orientations, we should rely on the 4th-order elastic tensors and perform rotation

transformations. Here, we rely on the reported equations (Wortman and Evans 1965) obtained by such transformation. When the transformation from system x_i to x_i', where

$$x_i' = l_i x_1 + m_i x_2 + n_i x_3, \quad i = 1,2,3$$

then

$$S_{22}' = S_{11} + S_c(l_2^4 + m_2^4 + n_2^4 - 1)$$

$$S_c = S_{11} - S_{12} - \frac{1}{2}S_{44}$$

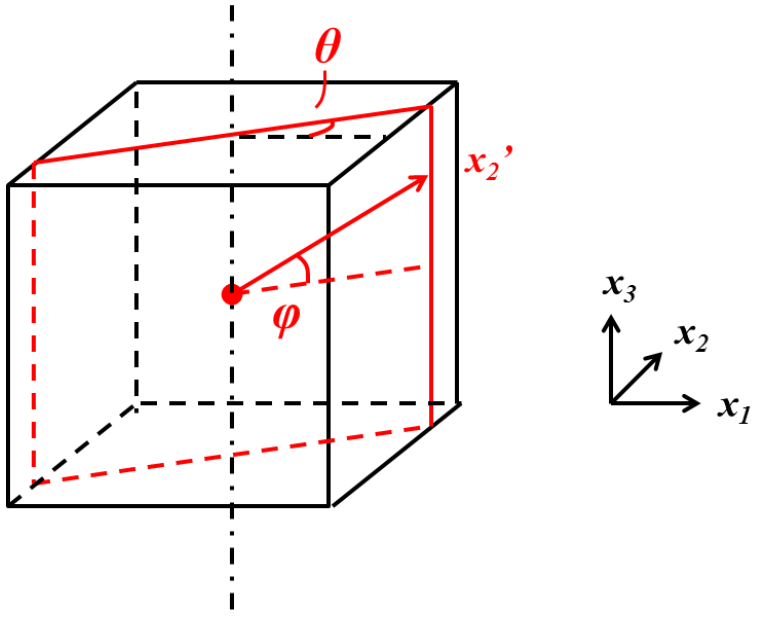

Figure 4.8 Illustration of the coordinate system used in the conversion of the Young's modulus along different orientations

Now, we introduce two angles, θ and φ, to represent the rotation of the coordinate axes, as shown in Fig. 4.8. The equation can be rewritten as

$$S_{22}' = S_{11} + (S_{11} - S_{12} - \frac{1}{2}S_{44})((cos\theta cos\varphi)^4 + (sin\theta cos\varphi)^4 + sin\varphi^4 - 1)$$

then

$$\frac{1}{E'} = \frac{1}{E} + \frac{9KG - EG - 3KE}{6KEG}((cos\theta cos\varphi)^4 + (sin\theta cos\varphi)^4 + sin\varphi^4 - 1)$$

The final equation means that the 3D polar graphs of Young's moduli along different orientations can be determined given a known set of (K, E, G). Whereas the 2D polar graphs of Young's moduli can be determined given a known set of (K, E, G, θ). It is then clear that to plot the polar graph of

Young's moduli in the (100) plane, θ need to be set as 0; and to plot the polar graph in the (110) plane, θ need to be set as $\pi/4$.

Fig. 4.9-13 summarize the polar graphs of the Young's moduli in the (100) and (110) planes for all the TPMS shells and corresponding hollow lattices. These polar graphs indicate the extent of an-isotropy regarding the Young's moduli along different orientations of the structures. The polar graphs of a perfect isotropic material have a precise circular shape. From Fig. 4.9 and Fig. 4.10, it is shown that the examined Gyroid and SP TPMS shells are not isotropic regarding their Young's moduli. They exhibit the highest Young's modulus along [111] direction and the lowest along [100] direction. On the other hand, from Fig. 4.11-13, although the an-isotropy of the SD, IWP and FRD shells are dependent on their thickness or volume density, at least one from each type of these 3 TPMSs has been examined to be near to isotropic. We also compare the an-isotropy of TPMSs and their corresponding hollow lattices. Except for the case of SP shells, which themselves are significantly more an-isotropic than other TPMSs, the an-isotropy of hollow lattices are higher than their corresponding TPMS shells. When the hollow lattice has a bending dominated strut-node relation, it generally has certain compliant orientations. This become obvious when the hollow lattice is slender, for examples, the slender BCC hollow lattices in Fig. 4.12 is 5 times more compliant in the [100] direction than in its [111] direction.

The an-isotropic of materials with cubic symmetry is often evaluated by Zener ratio (INGEL and III 1988), expressed as follow:

$$Z = \frac{G_{100}}{G_{110}}$$

The Zener ratio of all examined structures are plotted in Fig. 4.14. It is interesting to note that as the thickness of the TPMS shells increase, the Zener ratio increases. This means that the Young's moduli along the [110] and [111] direction increases faster than the Young's modulus along the [100] direction does, as the shell thickness increases.

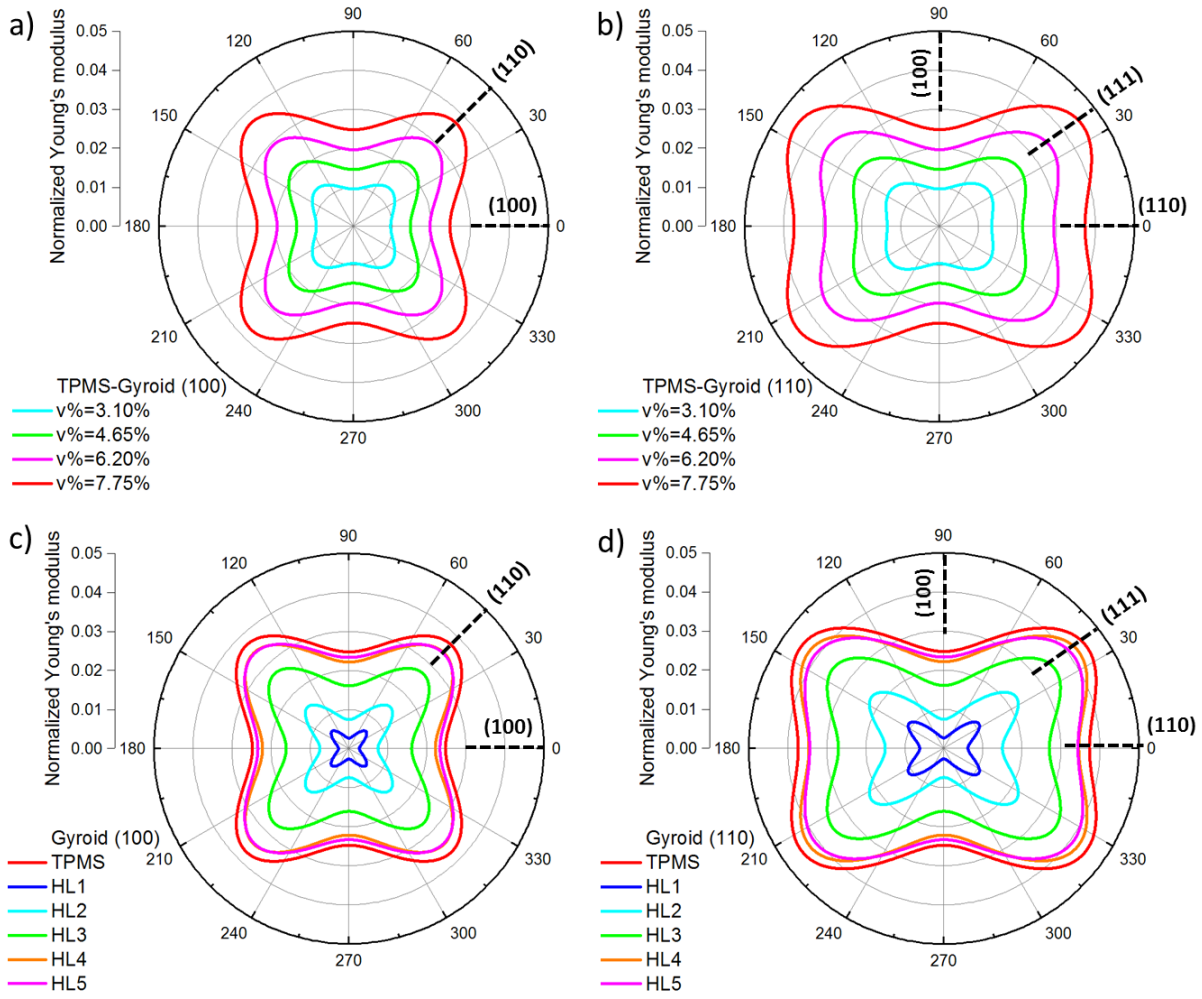

Figure 4.9 Polar graphs for a) Gyroid TPMSs with varied volume density ($\theta = 0$); b) Gyroid TPMSs with varied volume density ($\theta = 45°$); c) Gyroid-HLs compared to the gyroid TPMS of the same thickness ($\theta = 0°$); d) Gyroid-HLs compared to the gyroid TPMS of the same thickness ($\theta = 45°$);

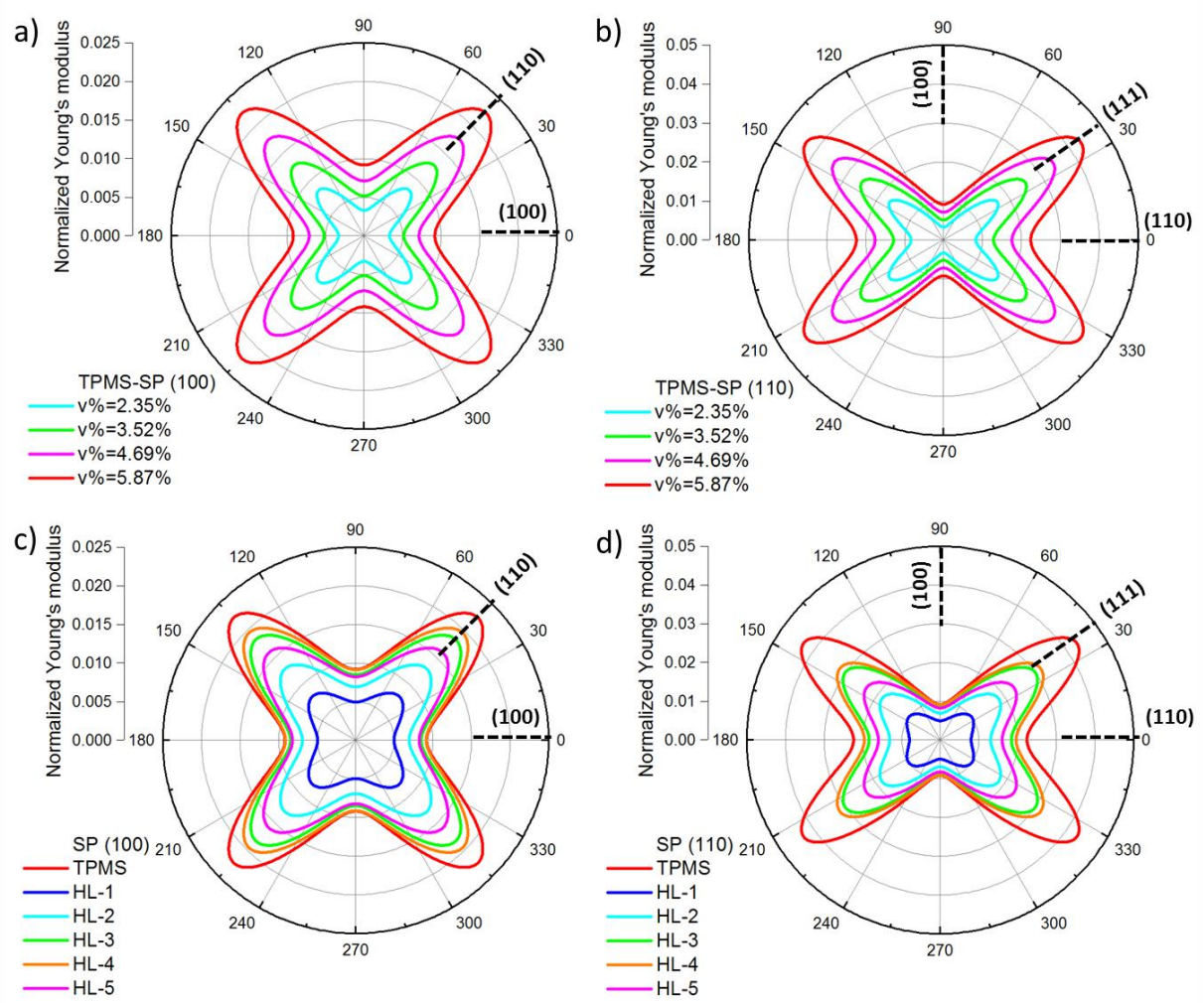

Figure 4.10 Polar graphs for a) SP TPMSs with varied volume density ($\theta = 0$); b) SP TPMSs with varied volume density ($\theta = 45°$); c) SP -HLs compared to the SP TPMS of the same thickness ($\theta = 0°$); d) SP -HLs compared to the SP TPMS of the same thickness ($\theta = 45°$);

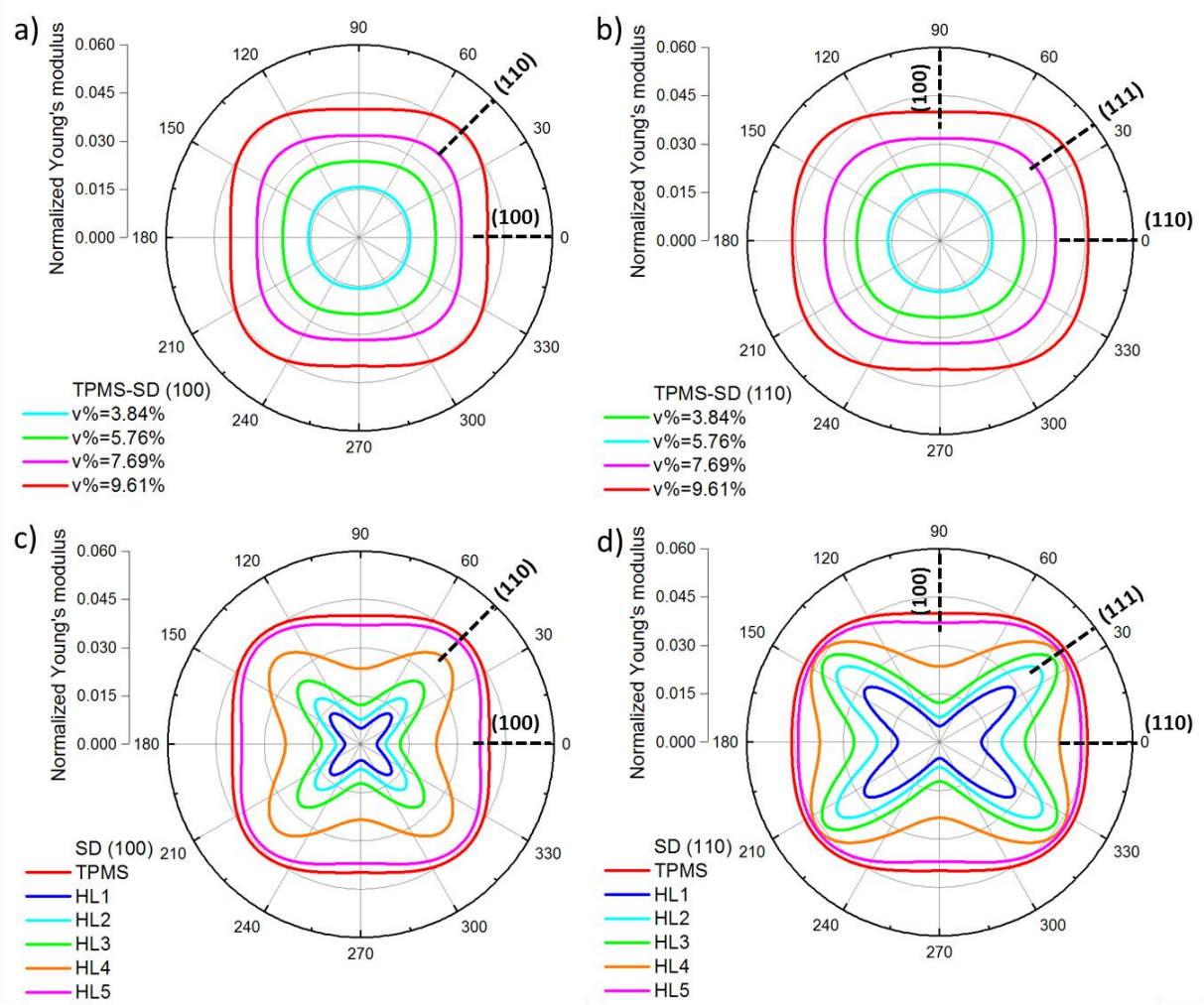

Figure 4.11 Polar graphs for a) SD TPMSs with varied volume density ($\theta = 0$); b) SD TPMSs with varied volume density ($\theta = 45°$); c) SD -HLs compared to the SD TPMS of the same thickness ($\theta = 0°$); d) SD -HLs compared to the SD TPMS of the same thickness ($\theta = 45°$);

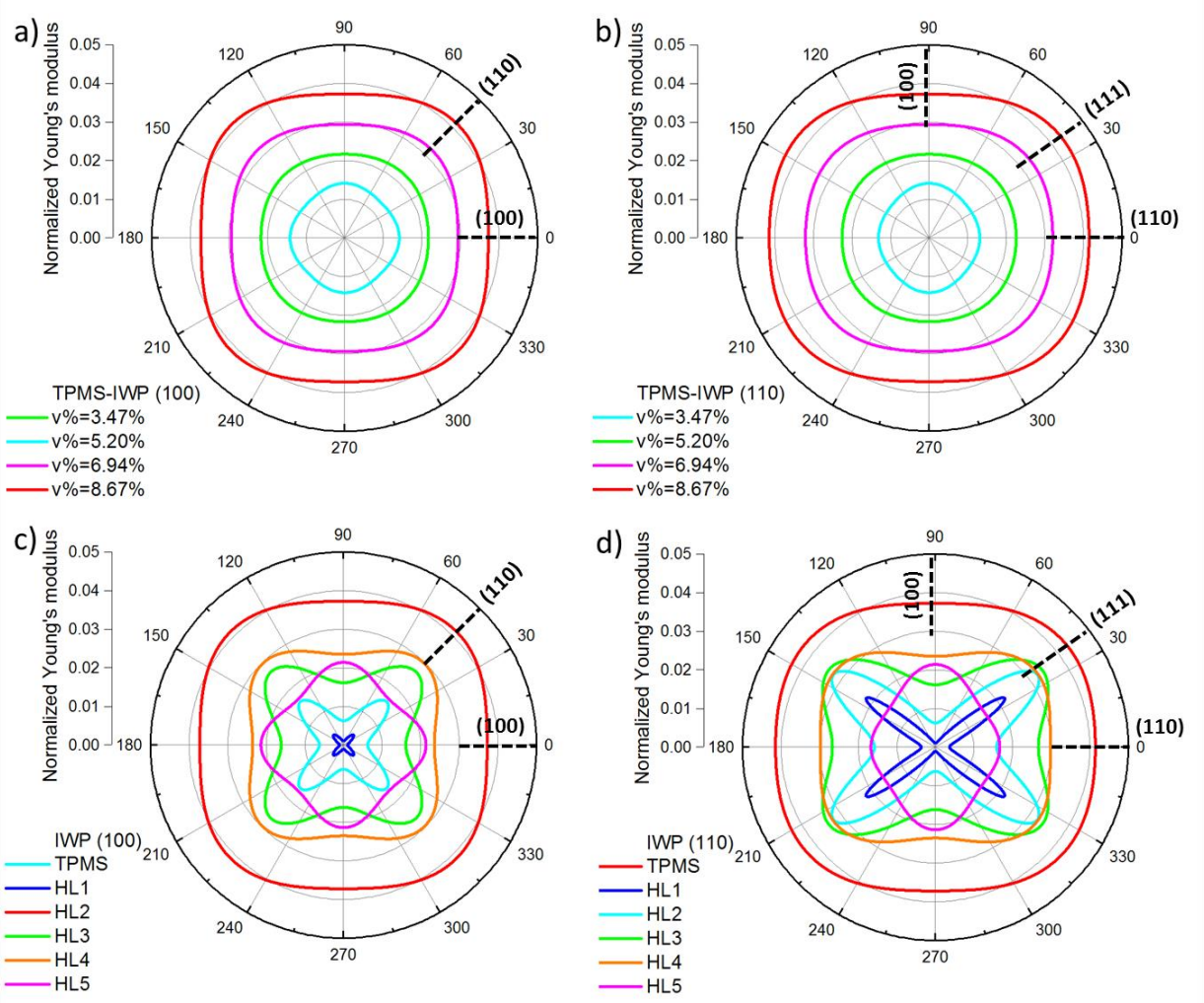

Figure 4.12 Polar graphs for a) IWP TPMSs with varied volume density ($\theta = 0$); b) IWP TPMSs with varied volume density ($\theta = 45°$); c) IWP -HLs compared to the IWP TPMS of the same thickness ($\theta = 0°$); d) IWP -HLs compared to the IWP TPMS of the same thickness ($\theta = 45°$);

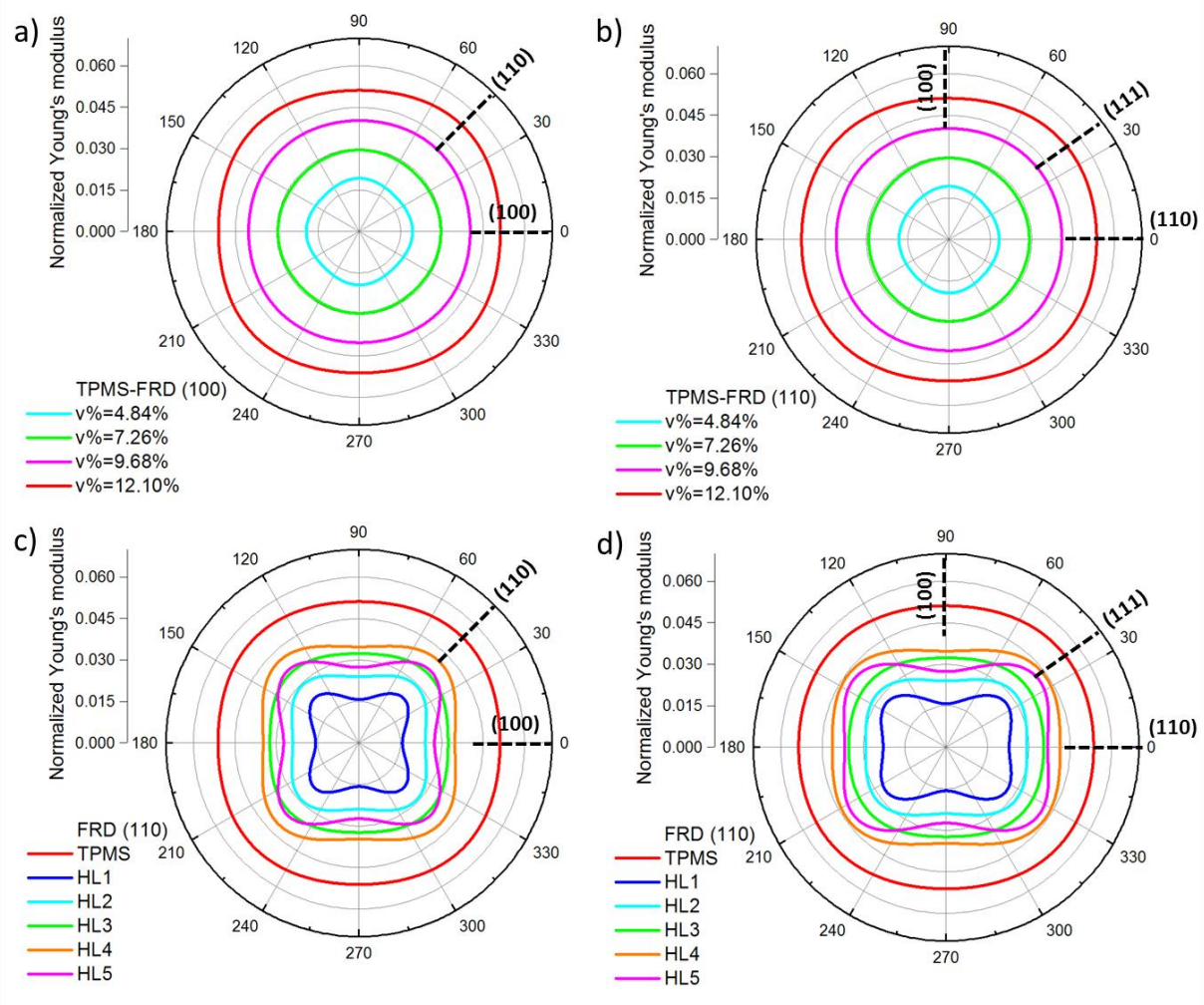

Figure 4.13 Polar graphs for a) FRD TPMSs with varied volume density ($\theta = 0$); b) FRD TPMSs with varied volume density ($\theta = 45°$); c) FRD -HLs compared to the FRD TPMS of the same thickness ($\theta = 0°$); d) FRD -HLs compared to the FRD TPMS of the same thickness ($\theta = 45°$);

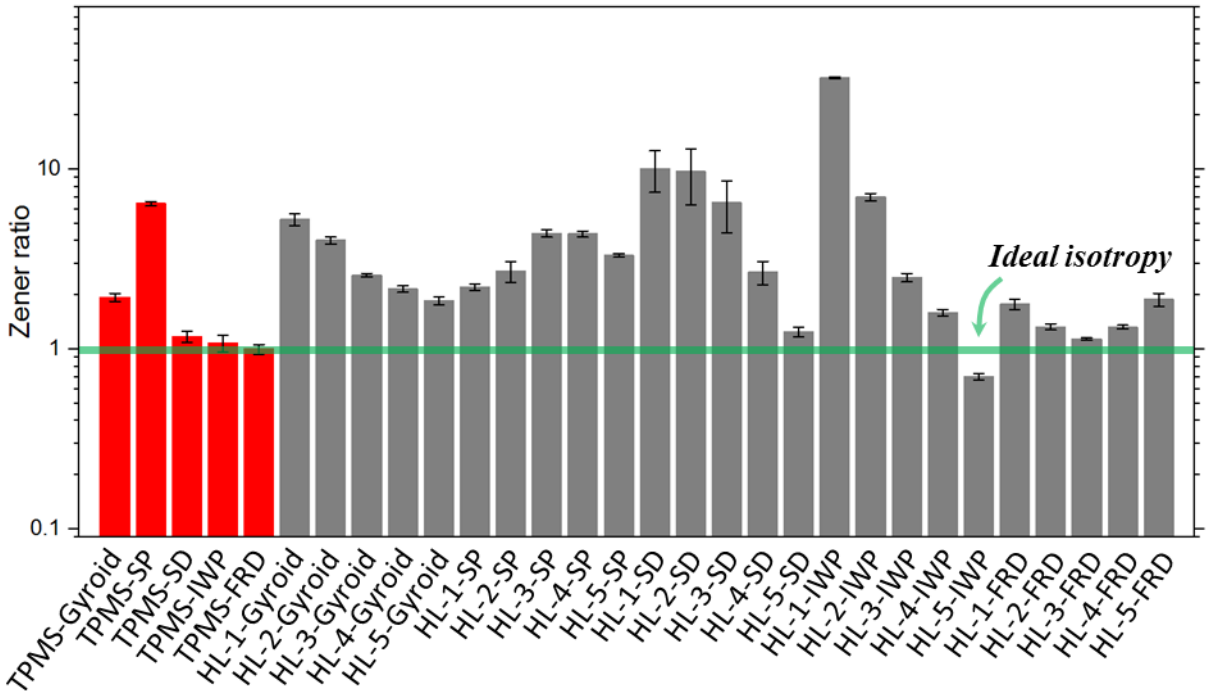

Figure 4.14 Zener ratios for all the numerically examined structures (HLs and TPMSs) in this work. The ideal isotropy line (Z = 1) is highlighted.

4.3.4 Mechanical properties of extended TPMS shells

Although the definition of TPMSs is simple, it often results into only one geometry solution for each symmetry. This means that the spatial design based on TPMSs are often inflexible. In other words, we only have 3 parameters to change, which are i) the thickness of the shell, ii) the length of the unit cell and iii) the symmetry of the TPMS, before we are fixed with a sole output for the geometry. Despite the outstanding mechanical properties that we already discovered with the TPMS shells, this problem limits the application of the TPMS shells where the spatial occupation percentage need to be tuned without changing the shell thickness and the unit cell size. Here we present a strategy to construct extended TPMSs (eTPMSs) while effectively preserving their outstanding mechanical properties. Furthermore, we explored the Young's moduli and the anisotropy of the generated eTPMSs as well.

The strategy to extend a TPMS is based on an important geometrical feature of a TPMS with planes of symmetry. For a TPMS with planar symmetry, for example, SP, IWP and FRD

surfaces, the surface meets the planes of symmetry orthogonally. This means that if the surface is sliced by a plane of symmetry and separated by a certain distance, the two parts can be connected by extending the cross-section lines at the slicing plane into new surfaces with zero Gaussian curvatures, while such extension operation does not introduce discontinuity to the extended surface as a whole. Fig. 4.15 depicts such extension operation for an FRD surface. In Fig. 4.15, the green meshed surface is the irreducible unit surface of an FRD surface. It meets four symmetry planes on its four boundaries. When the FRD surface is put to a typical FCC unit cell, the four symmetry planes mentioned above are the (001), (110), $(1\bar{1}0)$ and $(10\bar{1})$ planes. By extending the cross-section lines between the FRD surface and these symmetry planes, or the boundaries of the green surface, along the normal direction of the symmetry planes, four extended surfaces (yellow) can be made. Theses extended surfaces are continuous extensions of the green unit surface. After such initial extension, the irreducible surface and one of its extension surfaces can be further expanded to a full unit cell by mirroring operations described in the previous section. These four types of unit cells of the eTPMSs are demonstrated in Fig. 4.15 as well.

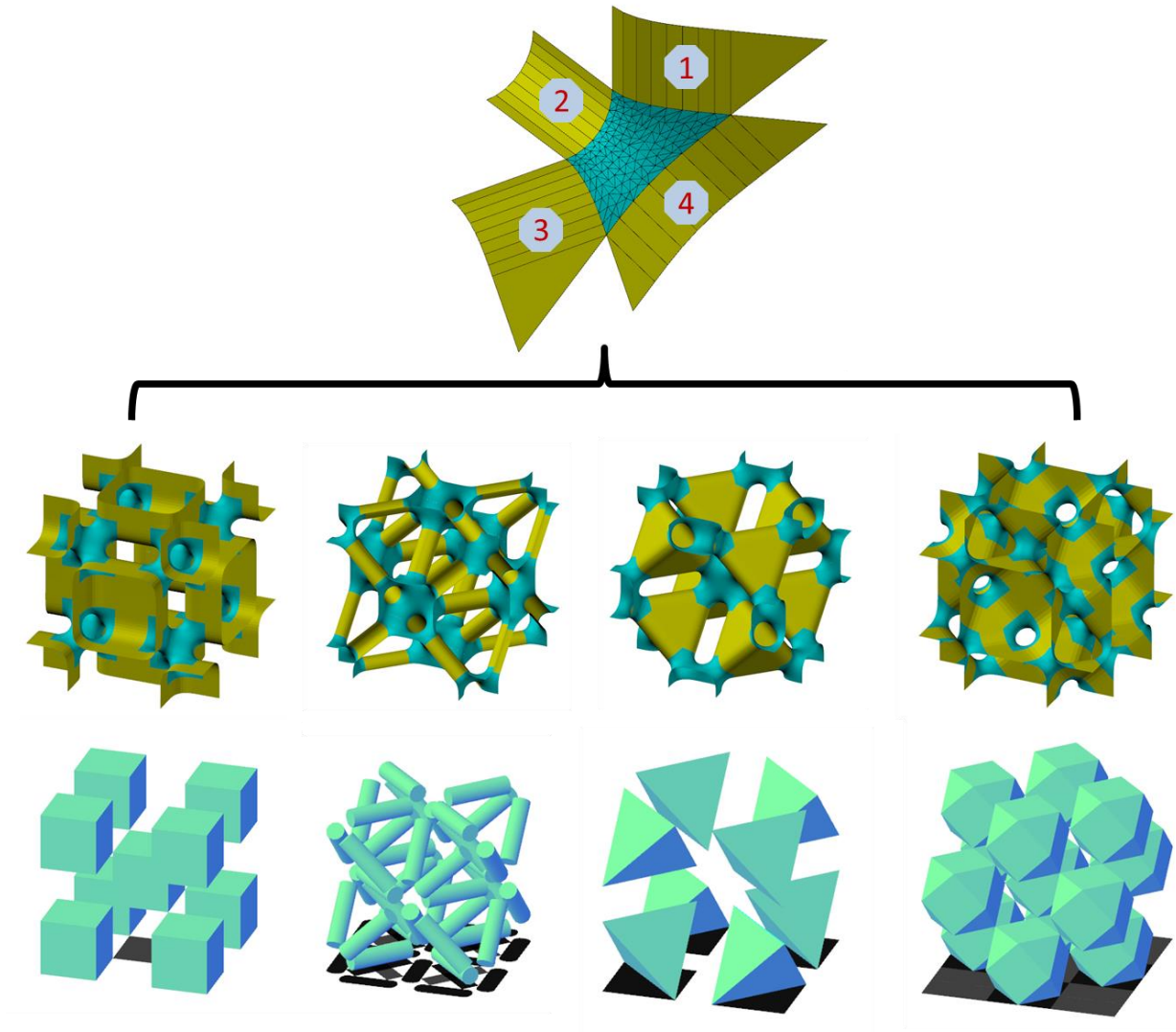

Figure 4.15 Illustration of eTPMSs developed from an FRD TPMS. The first row shows possible ways to extend zero-Gaussion-curvature surfaces from an irreducible TPMS unit surface; the second row shows the four types of eTPMSs (green: zero-mean-curvature surface, yellow: zero-Gaussion-curvature surface); the third row shows representative 3D space groups for the eTPMS above.

The four types eTPMSs in Fig. 4.15 can be perceived with the idea of connecting zero Gaussian curvature surface components with slices of TPMSs. To be more specific, the first eTPMS (Ext-1) is equivalent to FCC-aligned cubic shells connected at their vertices; the second eTPMS (Ext-2) is equivalent to a FCC hollow lattice, in which the cylindrical struts are connected with TPMS nodes; the third eTPMS (Ext-3) is equivalent to SC-aligned tetrahedron shells connected at their vertices; the forth eTPMS (Ext-4) is equivalent to FCC-aligned truncated cube

shells connected at their triangular faces. The zero Gaussian curvature components are hollow cubes, cylinders, tetrahedrons and truncated cubes in the Ext-1-4, respectively. In fact, it has been reported that the node smoothing in a hollow lattice material is beneficial to its mechanical performance (Portela, Greer, and Kochmann 2018). However, an optimal smoothening strategy has not been defined. In this work, we are also testing the TPMSs as the smooth connection of the zero Gaussian curvature component, including cylindrical struts in hollow lattices.

Herein, we will mainly examine the eTPMSs on the basis of the FRD surface.

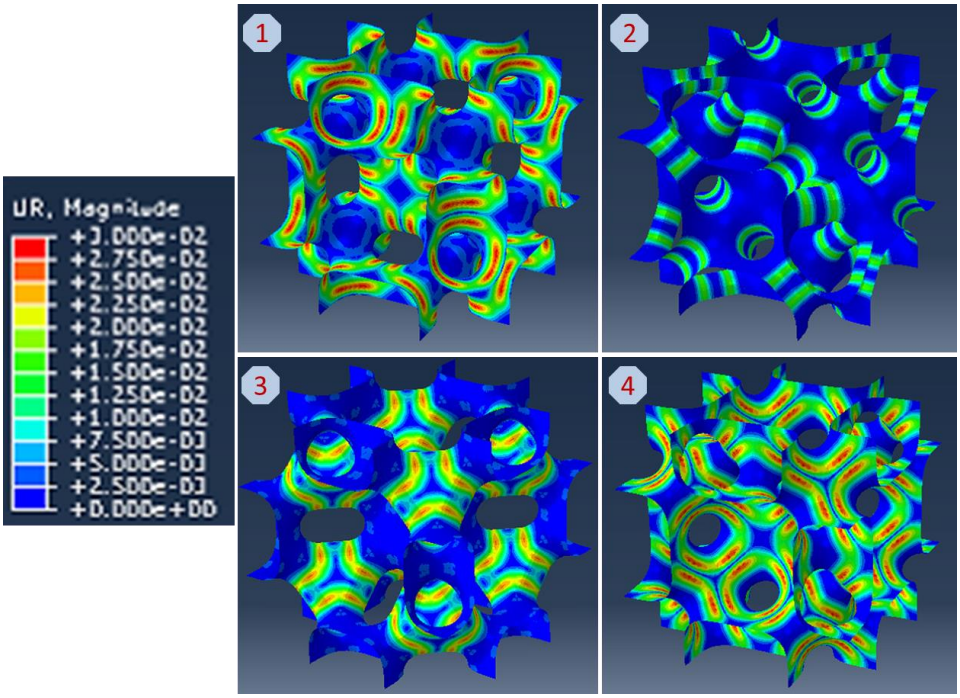

Figure 4.16 Comparison of the rotational displacement (bending) between various eTPMS shells and under the deformation of hydrostatic tension. The strains over xyz directions are 0.8% respectively.

Firstly, we put these eTPMSs under hydrostatic tension to evaluate their bulk moduli. Fig. 4.16 and Fig. 4.17 depict the rotational displacement and stored elastic energy distributions of these eTPMSs. It is shown that these eTPMSs do not maintain exactly their shape during hydrostatic tension. Also, their stored elastic energy is not uniformly distributed across the structure. These indicate that the eTPMSs no longer possess the mechanical behavior of TPMSs, which leads to maximized bulk moduli. Fig. 4.18 further details the bulk moduli of the examined eTPMSs, showing that they are deviating from the ideal Hashin-Shtrikman upper bound by the range of 11.2% to 38.4%, depending on their extension lengths or shell thicknesses. Although

these eTPMSs are still surpassing the hollow lattices discussed in the previous sections in bulk moduli.

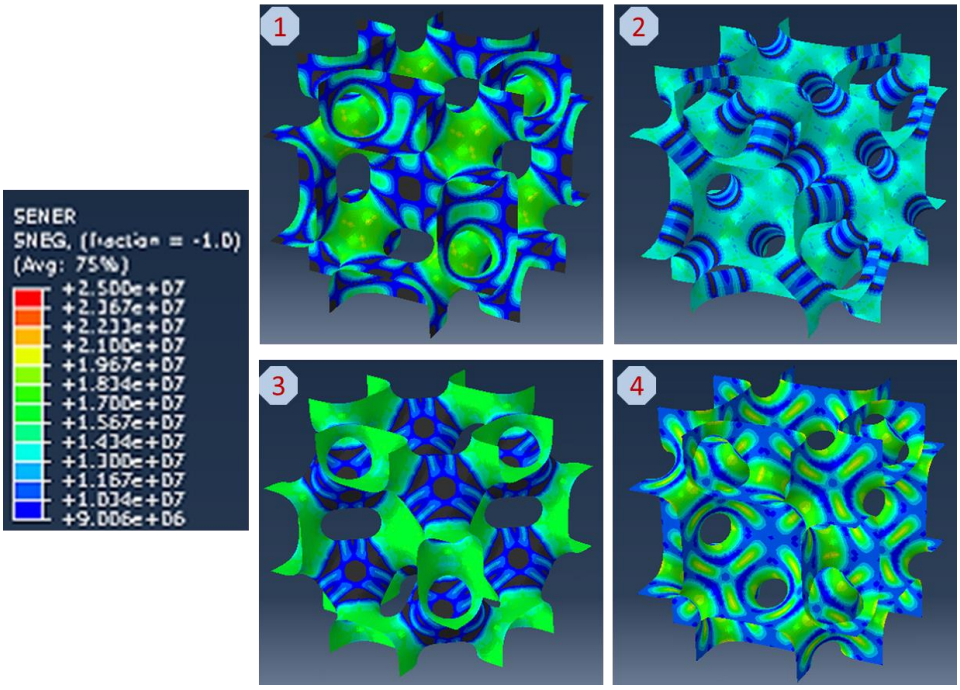

Figure 4.17 Comparison of the elastic energy distribution between various eTPMS shells under the deformation of hydrostatic tension. The strains over xyz directions are 0.8% respectively.

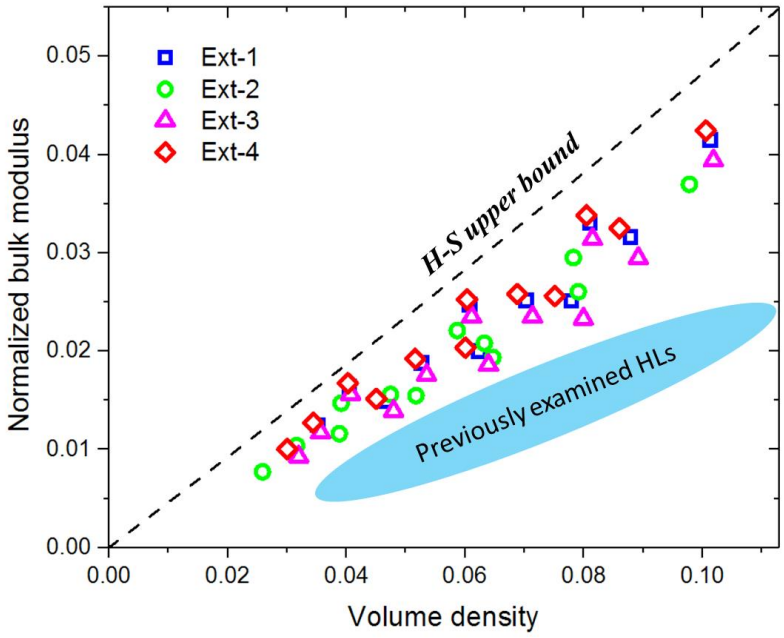

Figure 4.18 Normalized bulk moduli of the four types of eTPMSs. Extension ratio: 0.2, 0.4, 0.6.

Even though the eTPMSs have lower bulk moduli than TPMSs, it might be different regarding their Young's moduli since their anisotropy can vary as the extensions are added to the surfaces. Fig. 4.19 shows the Young's moduli of the eTPMSs along the [100] direction in comparison with the FRD surface. Interestingly, despite the wide distribution of the Young's moduli from eTPMSs, the highest value can match the same level as the Young's moduli from FRD shells, specifically.

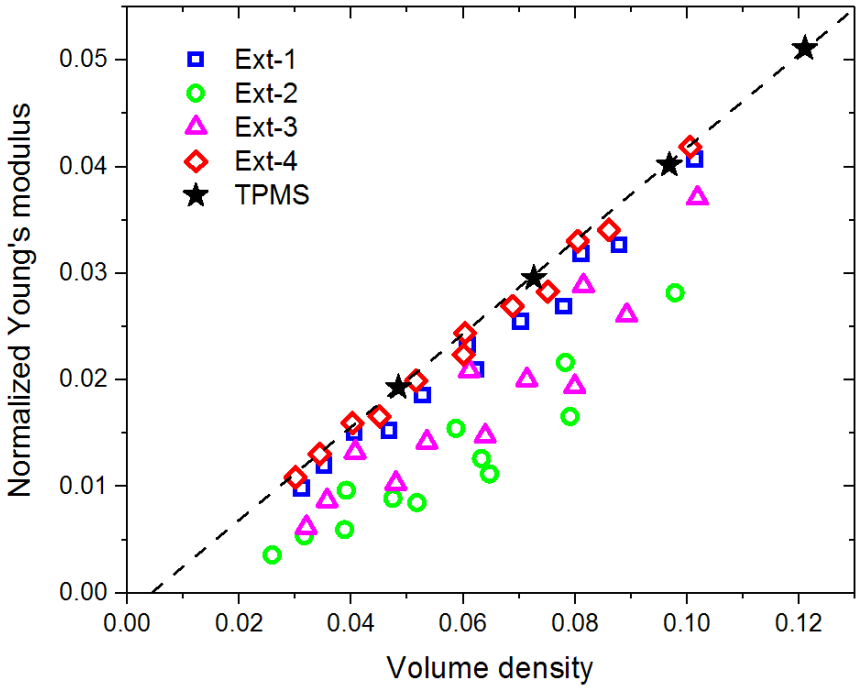

Figure 4.19 Normalized Young's moduli along [100] direction of the four types of eTPMSs. Extension ratios: 0.2, 0.4, 0.6.

In order to clearly show whether the specific Young's moduli of the eTPMSs can be superior than those of the TPMSs, the polar graphs regarding the specific Young's moduli in the (110) plane of selected eTPMSs and the FRD shell are plotted. The selected eTPMSs have the shortest extension length among the explored values and have the same thickness as the reference FRD shell. In Fig. 4.20, the four eTPMSs listed are compared to the FRD shell. We can see that the eTPMS of extension-1 has higher specific Young's moduli along the [110] and [111] directions compared to the FRD shell, although its specific Young's moduli along the [100] direction is lower. The eTPMSs of extension-3&4 have nearly the same specific Young's moduli compared to

the FRD shell along the [111] and [100] directions, respectively, while along other directions, they fall short. The eTPMS of extension-4 is closest to be isotropic, meaning that such extension operation can serve as a way to repair the an-isotropy of the TPMS, while preserving the high moduli of the surface structures. Notably, the eTPMS of extension-2 become significantly more compliant in all directions compared to the FRD shell.

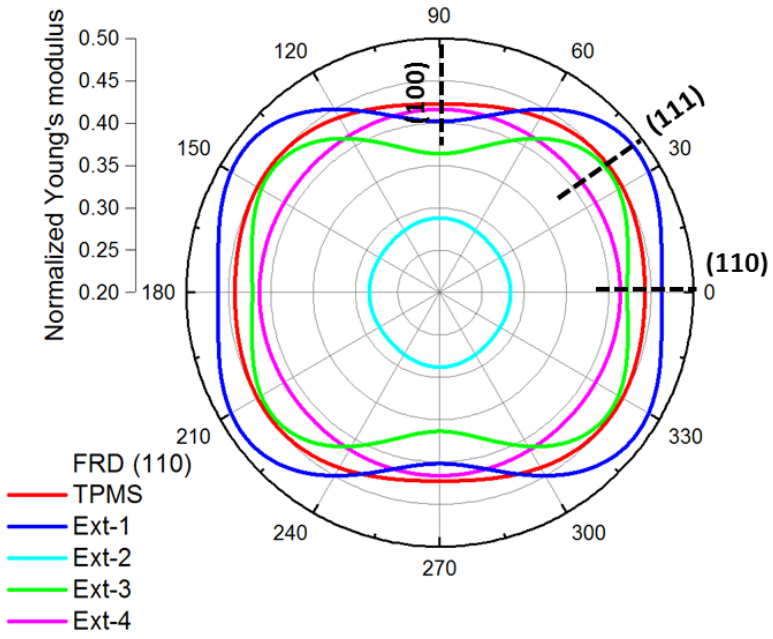

Figure 4.20 Polar graphs showing the normalized Young's moduli of the four types of eTPMSs. Extension ratio: 0.2.

In fact, the geometry of the eTPMS of extension-2 is very similar to hollow lattices. The extended surface in the eTPMS of extension-2 are the hollow cylindrical struts, while the original TPMS serves as the hollow nodes. Despite their adequate bulk moduli, their Young's moduli are significantly lower because of a major decrease in their Poisson's ratio. Therefore, structures that are geometrically like hollow lattices could be interior towards high Young's moduli.

The reason that the eTPMS of extension-1 has the highest specific Young's moduli among all the examined shell structures along their [111] direction is that their extended surfaces are mostly aligned parallel with the {100} planes. Such alignment makes these extended surfaces active in storing elastic energy when the shell is stretched along [110] and [111] direction. Other eTPMSs do not have a concentrated way of aligning the extended surfaces. The improvement of specific Young's modulus is essentially realized by tuning the mechanical anisotropy of the structure

without inducing significant change in bulk modulus. Effectively, the Young's moduli along certain orientations will increase while the moduli along other orientations will decrease. The evolution of Zener ratios in all four type of FRD based eTPMS is plotted in Fig. 4.21.

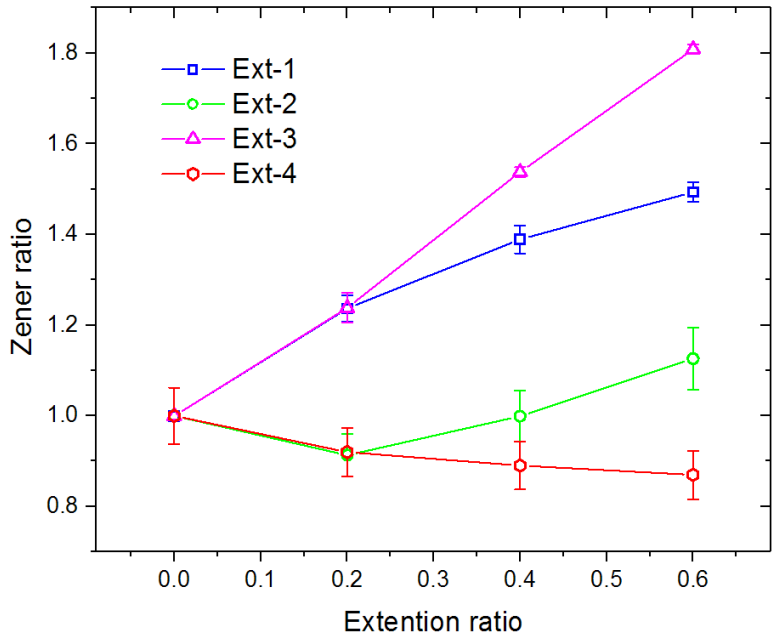

Figure 4.21 Zener ratios of the four types of eTPMSs. Extension ratios: 0.2, 0.4, 0.6.

4.3.5 Experimental explorations

Because the experimental test samples consist of four side walls and inner structures, as shown in Fig. 4.22, the measured Young's modulus of the structure is hardly the direct reflection of the theoretical Young's modulus of the periodic structure itself. However, the numerical results in the previous section can serve as the guideline for searching better mechanical performance in various of available inner structure designs, while the side walls are present.

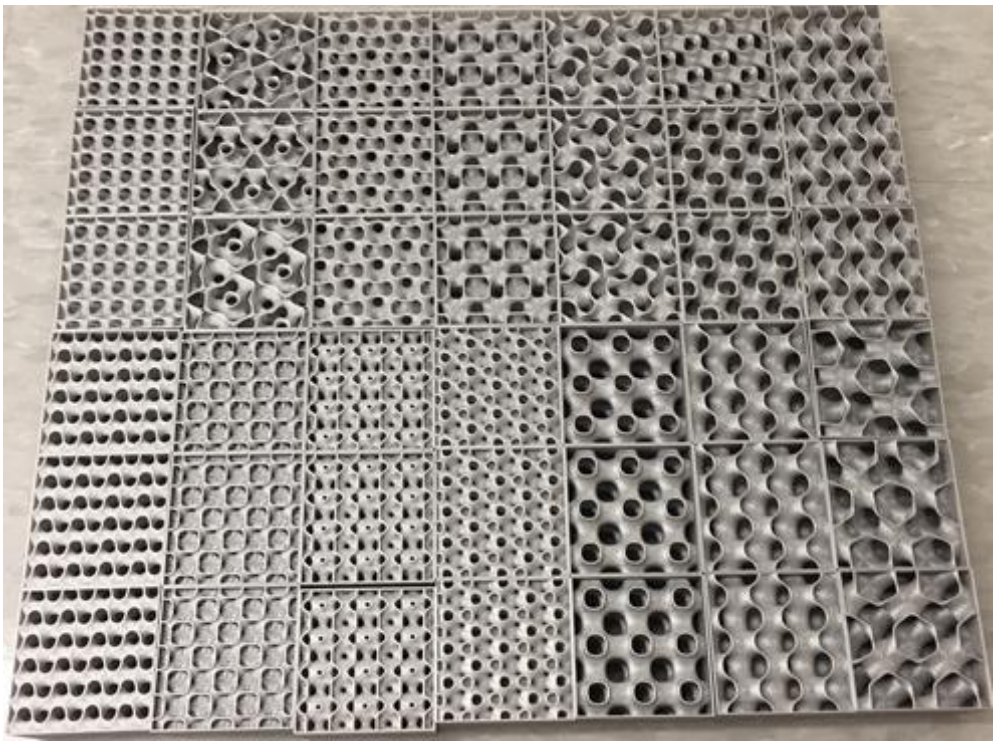

Figure 4.22 Photograph of various printed TPMSs along [100], [110] and [111] directions.

The measured Young's moduli of various 3D printed samples of TPMSs, eTPMSs and HLs are plotted in Fig. 4.23. It shows that the TPMSs and HLs have similar elastic moduli when the mass density is below 0.2 g/cm^3. At higher mass densities, the Young's moduli of TPMSs are slightly higher than the HLs given that they have similar densities. The contrast between the elastic stiffnesses of TPMSs and HLs are not so significant experimentally compared to their numerically predicted values. This phenomenon should be attributed to the underperformance of 3D printed TPMSs due to the imperfections introduced in the printing processes. The used FDM 3D printing method inevitably brings inaccuracy and anisotropy because of the nature of layer by layer printing. Nevertheless, between HLs and TPMSs, the latter are still the better options for a higher elastic stiffness.

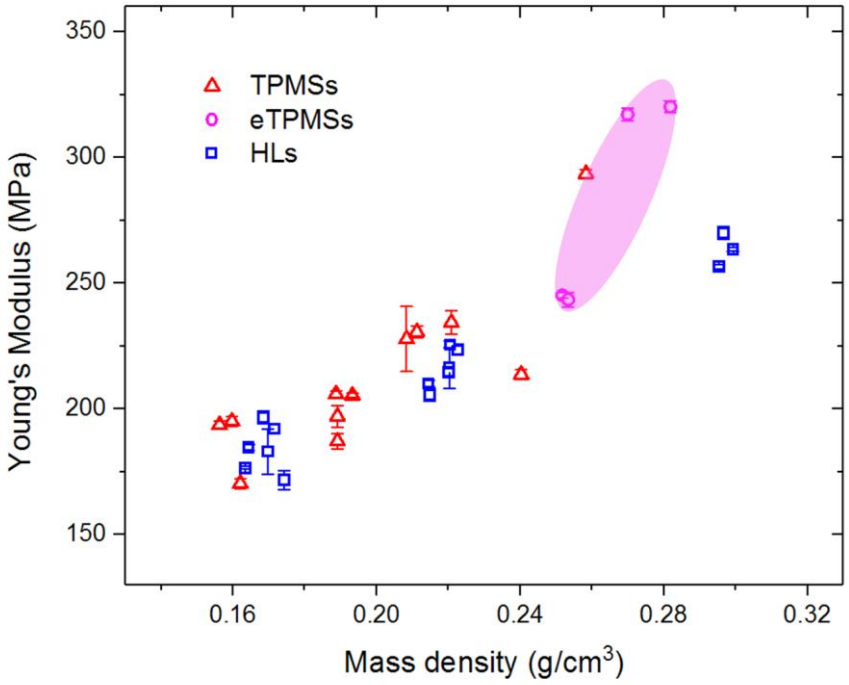

Figure 4.23 The measured Young's moduli of various samples of TPMSs, eTPMSs and HLs.

Notably, the chosen eTPMSs (Ext-1) are outperforming both TPMSs and HLs in the density range of 0.24-0.3 g/cm^3. This is consistent with the numerical results. The comparison of the experimentally measured and numerically predicted Young's moduli is shown in Fig. 4.24. The improvement along the [111] direction of the FRD based eTPMS (Ext-1) at an extension ratio of 0.2 is 9.5% compared to the FRD TPMS, while the numerical results predicted an 8.2% increase. The improvement along the [100] direction of the Ext-1 structure at the extension ratio of 0.2 is around 3.4% compared to unextended FRD TPMS, despite that the numerical results predict a 4.8% decrease. Again, this is caused by the inaccurate geometry produced by FDM 3D printing, especially the zero-mean-curvature surfaces where the key mathematical feature of the structure is sensitive to the inaccuracy.

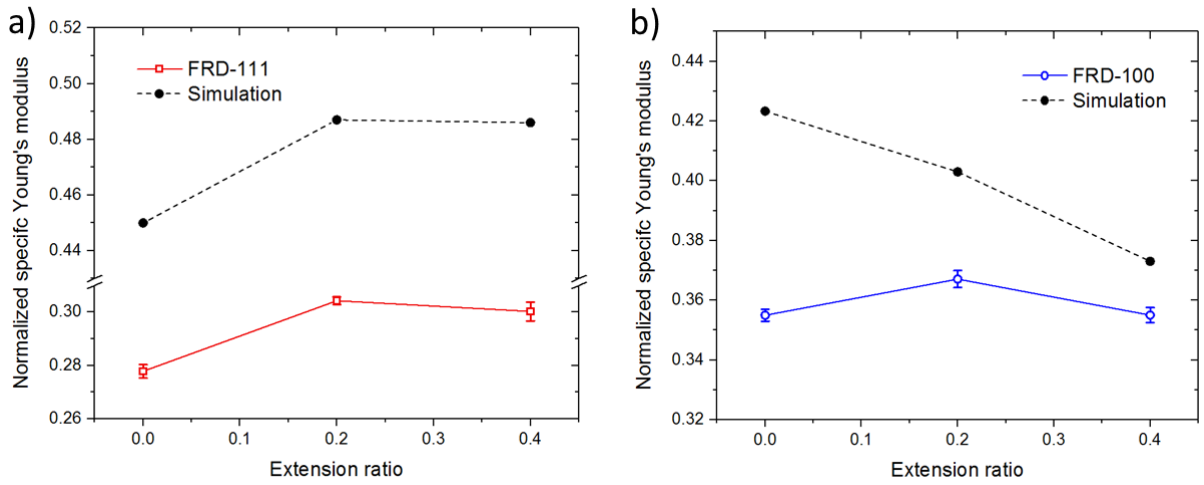

Figure 4.24 The comparison of the experimental and numerical results on the normalized specific Young's modulus of FRD based eTPMs and TPMSs along the orientation a) [111] and b) [100].

4.4 Conclusion

In this chapter, we have systematically studied the static mechanical properties of thin elastic TPMS shells and eTPMS shells through numerical models. We have developed numerically accurate geometries in the models for 5 types of TPMSs (Gyroid, SP, SD, IWP and FRD) with varies symmetries, covering all commonly used shellular designs. They are compared with hollow lattices of different strut length to unit cell size ratios regarding bulk moduli and Young's moduli along all crystallographic orientations. TPMSs are proven to have higher moduli values in all comparisons to hollow lattices. All TPMSs are showing near ideal specific bulk moduli, which is only lower by less than 2% compared to the theoretical Hashin-Shtrikman upper bound. In particular, the FRD shells are also showing good potential in achieving near isotropy. Moreover, we propose extension methods for a larger library of shellular designs, namely eTPMSs, on the basis of TPMS surfaces and have examined the case for FRD surfaces. The eTPMSs can provide larger tuning space for the Zener ratio, which is a measure of an-isotropy, while preserving the high specific moduli. Especially, we discovered one of the eTPMSs as a good candidate for pursuing exceptionally high specific Young's modulus along a certain crystallographic direction ([111] direction), surpassing the specific Young's modulus reference FRD shell.

5. MULTISCALE TRIPLY PERIODIC MINIMAL SURFACES WITH CORRUGATED SUB-STRUCTURE

5.1 Introduction

Triply periodic minimal surfaces (TPMSs) have been attracting much attention in recent research studies for pursuing ultimately stiff and strong materials with 3D architectures (Al-Ketan, Abu Al-Rub, and Rowshan 2018; Bonatti and Mohr 2019b; S. C. Han and Kang 2019). Thin shellular structures with TPMS designs are found to be excellent regarding their bulk moduli, approaching nearly the theoretical Hashin-Shtrikman upper bound. Such superior bulk moduli originate from the unique mean zero curvature of the TPMSs, which effectively repel any strain concentration or geometry distortion when the structure is imposed with hydrostatic loading. However, in many real-life applications, such as load bearing or energy absorption, in which light weight cellular materials are often used, external loads are often an-isotropic. To be more specific, in many cases, the Young's modulus or yield strength in the optimal orientation is the most critical performance index for hollow structures. When a TPMS structure is subject to uniaxial loading, local changes of curvatures, or so-called bending spots, are inevitable. Firstly, bending is much less efficient in storing strain energy than stretching, it usually unfavored when a higher stiffness is desired. Secondly, the bending of TPMS structures often lead to early yield or local failure since like many cellular structures, the TPMS structures hardly have any strain hardening ability. These challenges need to be overcome especially when the TPMSs are under compressive loadings.

Corrugated surfaces are found in nature. Leaves of palm and beech have corrugated surfaces, which originate from their folding mechanism during growth (Kobayashi, Kresling, and Vincent 1998). These corrugated surfaces can naturally be used to generate 3D structures with folding or collapsing mechanisms. In many cases, for example, Miura-ori, the structures can be folded with a single degree of freedom (Schenk and Guest 2013). However, the conditions for a folding mechanism is often strict. Pattern of tessellation, boundary conditions and thickness of the structure shell all affect whether a folding mechanism is possible. Examples have been shown that without a possible folding mechanism, or with relatively rigid boundaries, a corrugated surface can be much stiffer than a smooth one under a load of bending. Corrugated panels are also widely applied in engineering applications because of their enhanced mechanical performance (Dayyani et al. 2015; Xia, Friswell, and Flores 2012).

Applying corrugated surfaces on a period 3D structure for stiffening or strengthening purposes is rarely discussed. Numerical pathways to impose origami structures on curved surfaces have been reported (Dudte et al. 2016). However, these discussions are mainly under the premise of preserving the foldability of the entire structure, which in return requires free boundaries for the curved structures. On the uniform deformation of a TPMS surface, periodic boundary conditions are often prescribed. It is then possible to introduce proper second-order corrugated structures on the TPMS surfaces, while any folding mechanism is denied. In this case, the bending behavior of the structure could be impeded by the increased local bending stiffness due to the corrugated sub-structures, which eventually leads to the improvement of Young's modulus or yield strength.

5.2 Methodology

5.2.1 Geometry designs

First of all, since the base TPMS structures are highly symmetrical, we determine that the introduction of second-order corrugated structures should not significantly disrupt or alter the original symmetry of the base TPMSs. This is not only meaningful in retaining the symmetry of the cellular structure, which could further affect the deformation mechanism, but also crucial in reducing the complexity while generating the multi-order structures. Here we used 3 types of TPMSs as the bases: Schwarz P (SP) surface, gyroid surface and Scheon's F-graph-Rhombic dodecahedra graph (FRD) surface.

As shown in the Fig. 5.1-3 below, in order to generate the multi-order TPMS structures with corrugated patterns, an irreducible unit surface should be generated based on their symmetry. Then, on these unit surfaces, V-groove shaped structures should be generated along assigned directions. Here, we note the direction of a V-groove to be the direction perpendicular to the V shape. Specifically, for SP surfaces, such unit surface is bounded by (001), (010), (110) and $(10\bar{1})$ planes. The unit surface within this cell is then simplified to a planar kite-shaped quadrilateral. The V-grooves can be imposed to either diagonal directions of the quadrilateral, resulting in either radical patterns or hexagonal patterns in the larger cells. We then name then as SP-Rad and SP-Hex. For gyroid surfaces, the irreducible unit surface is bounded by a pair of (001), (010) and (001) each, which is a cube of 1/64 of the gyroid unit cell. The surface within such a cell can be simplified to two contacting triangles. The angle between these two triangles is 135.6 °. Similar to the SP

case, the V-grooves can be directionally imposed on these triangles to form either radical patterns or hexagonal patterns. The resultant corrugated surfaces are names as Gyroid-Rad and Gyroid-Hex. For the FRD case, the bounding planes of the irreducible cell are (001), (110), $(1\bar{1}0)$ and $(10\bar{1})$. Different from the SP and gyroid cases, the curved quadrilateral within the irreducible cell is not symmetrical. Therefore, the directions of the imposed V-grooves are no longer the diagonal directions, which are from vertex to vertex. Instead the directions of the imposed V-grooves are from edge to edge. In the meantime, the unit quadrilateral is remained curved instead of being simplified to a planar one. The merit of this arrangement is that the position of the vertices can be remained at the peak or valley of the V-grooves, despite the asymmetry of the unit quadrilateral. If any of the four vertices are not placed at the peak or valley of the V-grooves, an incomplete period of the V-grooves will form on the boundaries of the quadrilaterals after mirroring, rotation or translation processes. In the end, the resultant two corrugated FRD structures are named as FRD-Rad and FRD-Hex for consistency.

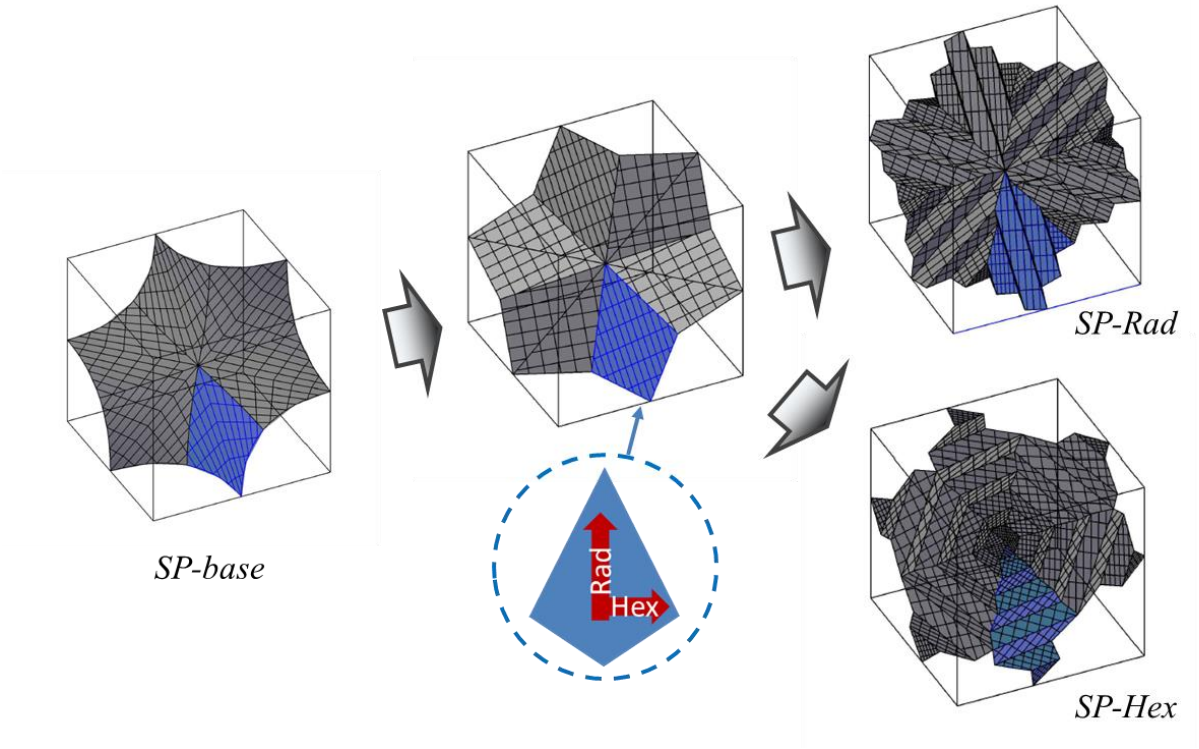

Figure 5.1 Transformation from SP structures to corrugated SP-Rad/SP-Hex structures.

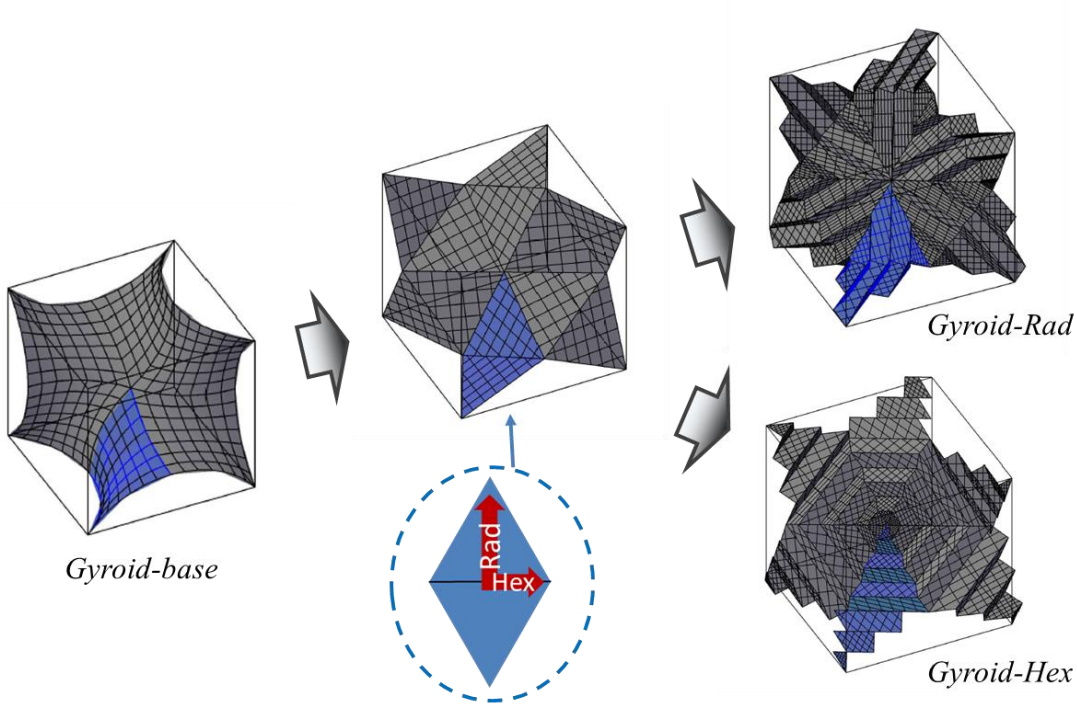

Figure 5.2 Transformation from gyroid structures to corrugated Gyroid-Rad/Gyroid-Hex structures.

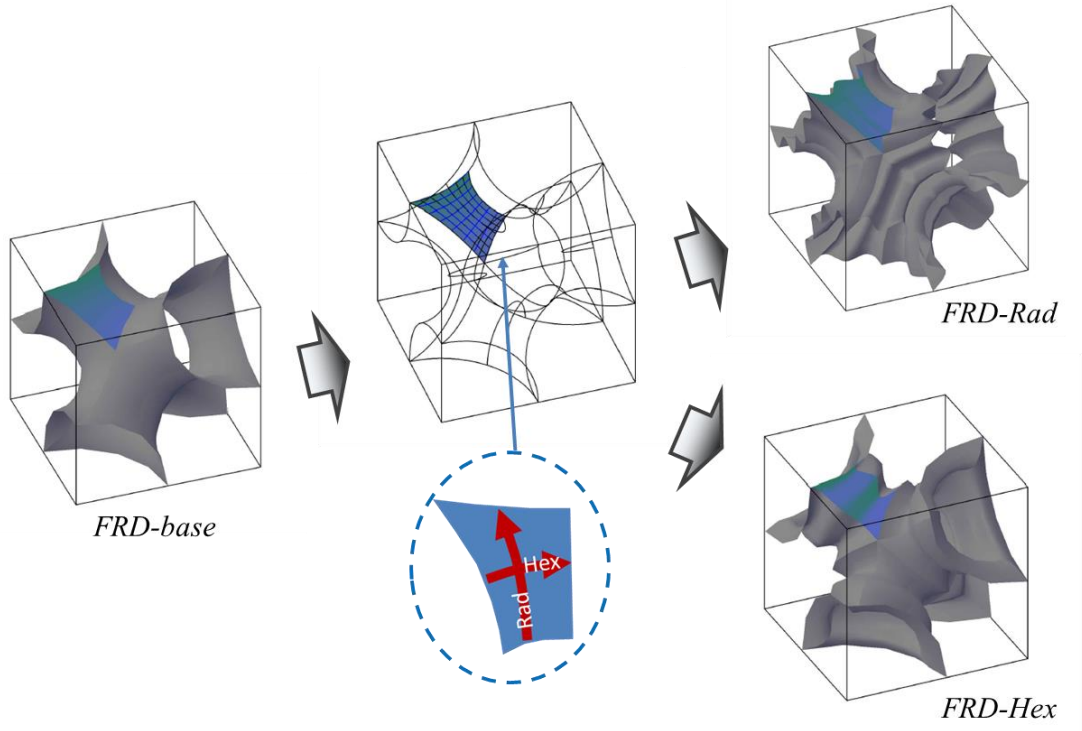

Figure 5.3 Transformation from FRD structures to corrugated FRD-Rad/FRD-Hex structures.

5.2.2 Structure fabrication and measurement

The structures are fabricated by two photolithography method through the Nanoscribe Professional GT 3D printer. IP-dip resin is used. Equipped objective lens is 63X. The original and corrugated TPMS structures were first developed in AutoCAD software and output as the STL file for input of the Describe software. Describe is a slicing/hatching software that comes with Nanoscribe Professional GT. The structures are written on a piece of 1' square quartz slide via Dip-in laser lithography (DiLL) mode. The laser power of 70 mJ is used and the galvo mirror driven laser spot movement speed is set to 10 mm/s. Four duplicates of each structures are written at the same time, placed at four corners of a square. The size of each structure is 42x42x28 μm and adjacent structures have a gap of 40-50 μm in between for ease of nanoindentation tests (the indentation head has a flat square top sized ~100 μm). For the samples that need to be reinforced by ALD ceramic shells, a properly rinsing and cleaning procedure is conducted before they are placed in the ALD chamber (Cambridge Nanotech Fiji ALD). The ALD coating of AlO_x is conducted at the temperature of 200 °C with O_2 plasma as the oxygen source. Typically, a thickness of 20 nm is coated during 200 cycles. Stress-strain curves of the samples during compression are obtained by nanoindentation measurement (G200, Keysight Technologies) with a flat-top indenter. All samples are compressed to failure at a strain rate of 10^{-3} s^{-1}. The before and after compression morphology of the sample structures are observed in a SEM microscope (Hitachi s-4800 FESEM) after properly coating the samples with Au-Pd.

5.3 Results and discussion

5.3.1 3D printing products

The final products of the 3D printed base and corrugated TPMS structures are displayed in Fig. 5.4 and Fig. 5.5. It is clear that despite the corrugated sub-structures, the base and two corrugated structures are nearly identical in shape. The size of the structure is L: 42 μm; W: 42 μm; H: 28 μm. Despite the digital input geometries of different samples having the same thickness of 0.35 μm, the 9 types of prints have different thicknesses and volume densities. The actual thickness and volume density values are measured from the SEM images. Fig. 5.6 shows the SEM measurement of the sample thickness. Typically, a feature thickness is measured from the SEM image. Because the selected feature thickness is not necessarily the effective thickness of the structure, some

measured feature thickness needs to be multiplied by a certain value in order to obtain the effective thickness of the shell. This multiplier can be obtained through the measurement in the CAD models. Although the shell thickness of the printed structure can change from the thickness of the original model, this multiplier remains the same as long as there's no angular distortion in the printing. The calibrated thicknesses and volume densities of various structures are listed in Table. 4.1. It turns out that the printed structures are all thicker than the input digital geometry.

Table 5.1 3D printed geometry calibration parameters

	SP-Base	SP-Rad/Hex	Gyriod-Base	Gyriod-Rad/Hex	FRD-Base	FRD-Rad/Hex
Feature thickness (μm)	0.73	0.83	0.62	0.66	0.54	0.58
Multiplier	1	0.86	1	0.91	1	1
Effective thickness (μm)	0.73	0.72	0.62	0.60	0.54	0.58
Volume density	12.6%	12.6%	13.9%	14.8%	18.9%	19.5%

There are many factors in the 3D printing process which could cause the printed structure to be thicker than the input CAD model. For examples, smaller slicing distance causes higher laser dose per resin volume, which could result in thicker curing; multiple contours, which means laser scans along the perimeter of the geometry, are likely to increase the thickness of vertical shells; the direction of the filling, which means the laser scans in aim of curing the infill volume within the outer perimeters, could cause the thicknesses of differently orientated shells to be unequal. Therefore, the shell thickness of 3D printed structures is a complex outcome of the slicing strategies and the laser scanning pre-set. More importantly, it could also be very dependent on the input geometry itself.

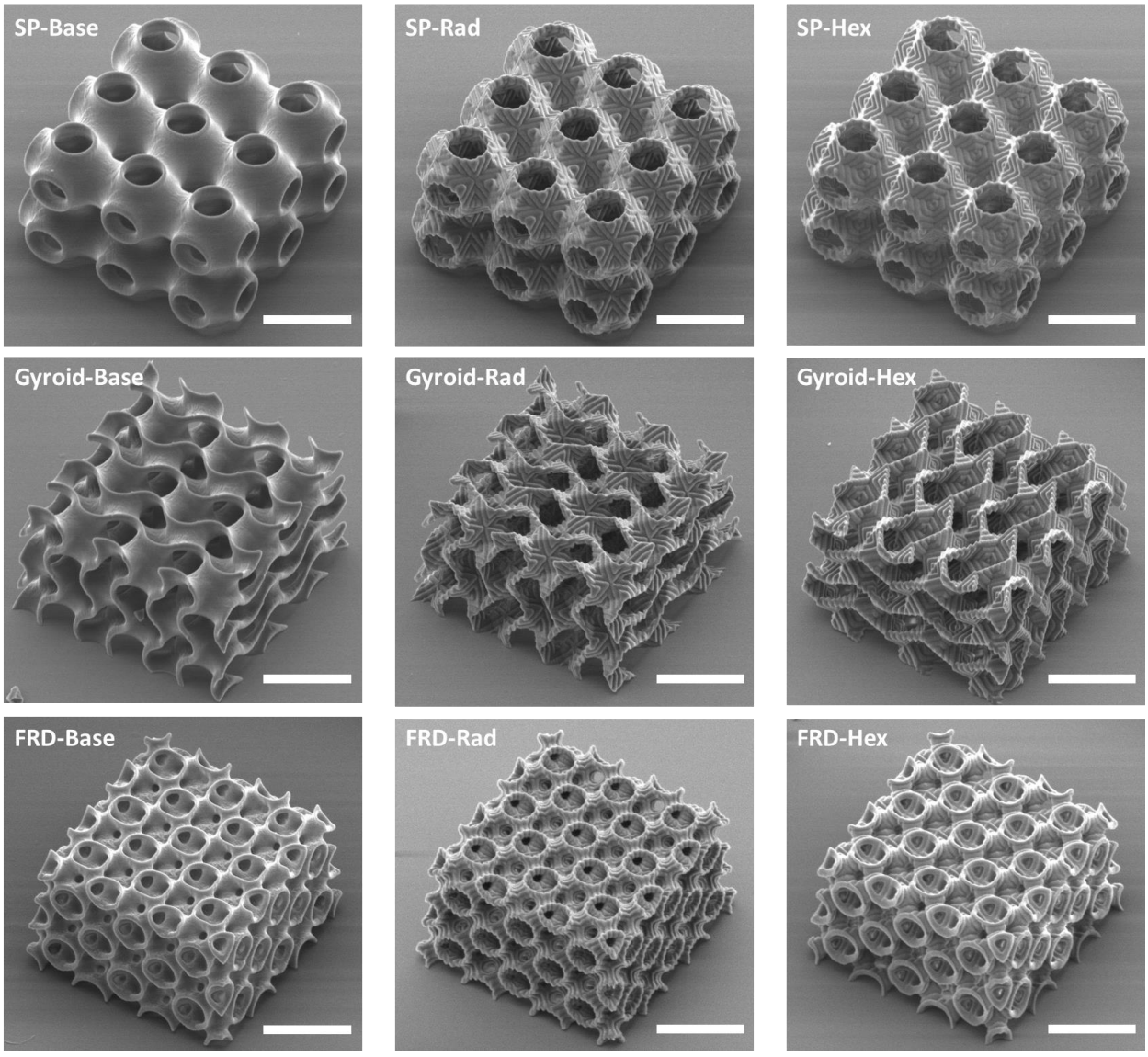

Figure 5.4 3D printed smooth and corrugated TPMS structures from an angled view, scale bar: 10 μm.

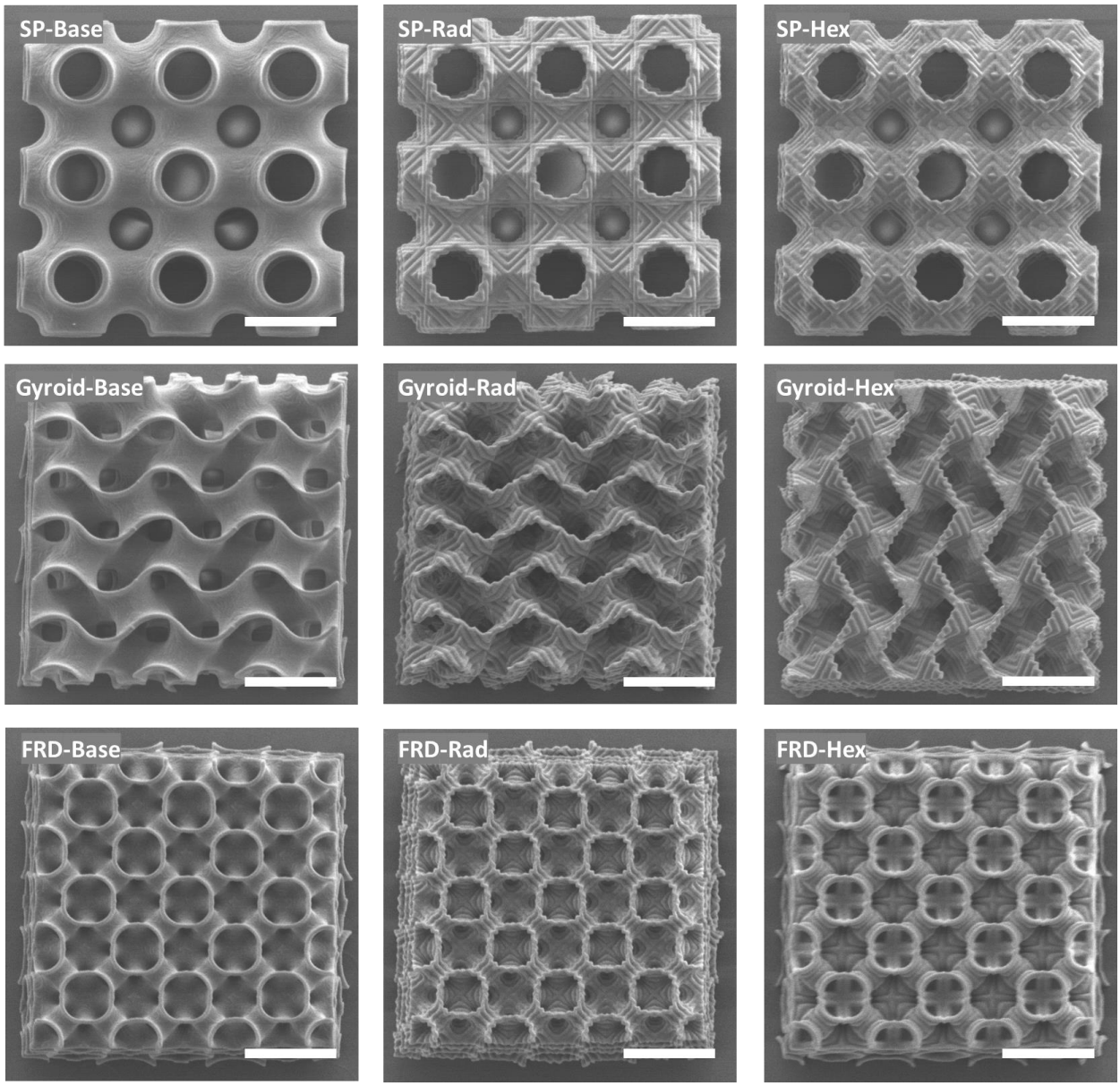

Figure 5.5 3D printed smooth and corrugated TPMS structures from top view, scale bar: 10 μm.

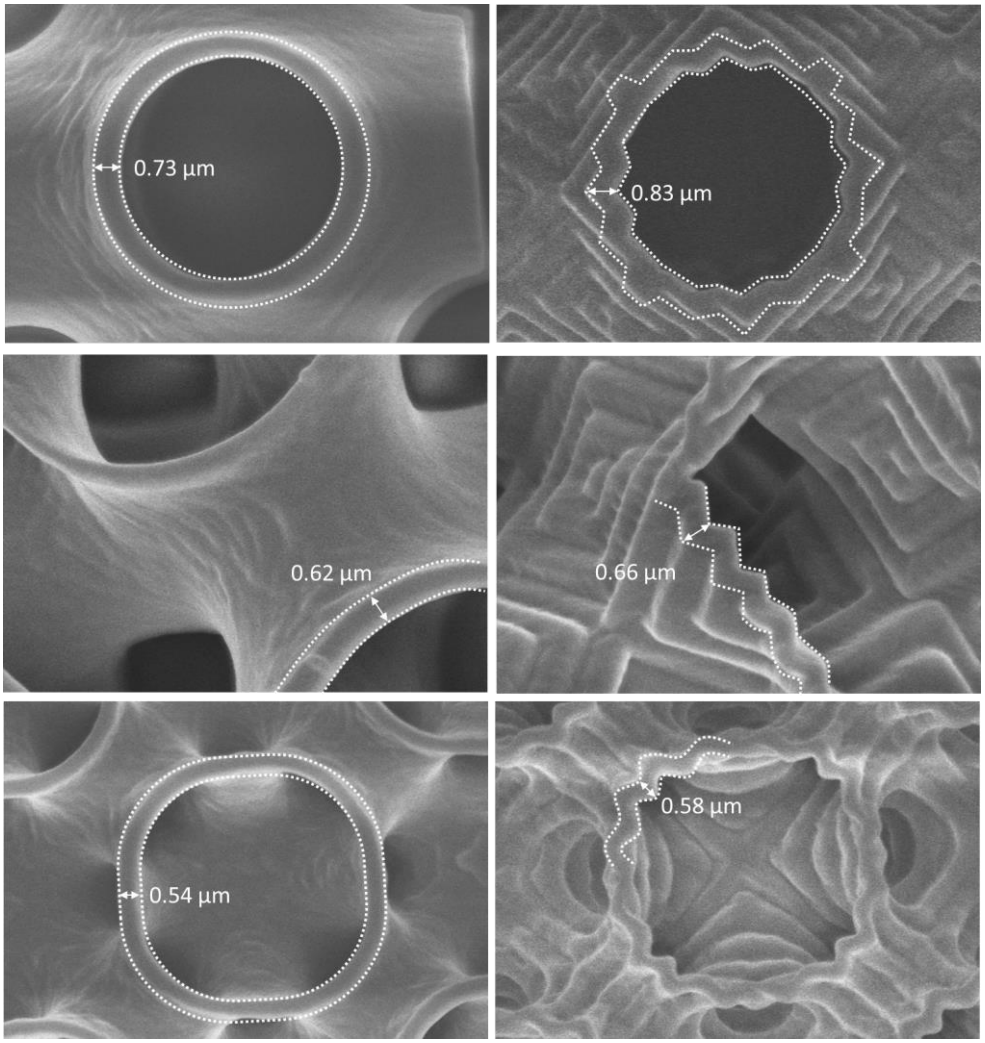

Figure 5.6 Size calibration for 3D printed smooth and corrugated TPMS structures on zoom-in SEM images.

5.3.2 Elastic property of corrugated TPMSs

The stress-strain curves of the original and corrugated TPMSs are obtained from the nanoindentation tests with flat punch indenter, as shown in Fig. 5.7. A typical stress-strain curve of the printed TPMS structures consists of 3 parts. Initially, a toe-area is often present, where the stiffness of the structure slowly ramps up. The reason for the existence of the toe-area is that the printed structures do not have a strictly flat top, which causes progressive contact and loading as the displacement of the flat indenter elevates. Such toe-area existence has been reported by other tests of micro-scale architected materials. The next stage is the elastic region, where the stress-

strain relationship is linear or close to linear, depending on the pristine material property. It has been reported that the cured IP-dip could present hyperelastic properties as well. However, in most cases, these cured photo-resins are perceived by general elastic-plastic behaviors. After the elastic stage, the structures yield and undergo plastic deformation before reaching final failure. The Young's modulus of the structure is measured in the elastic region of the stress-strain curve.

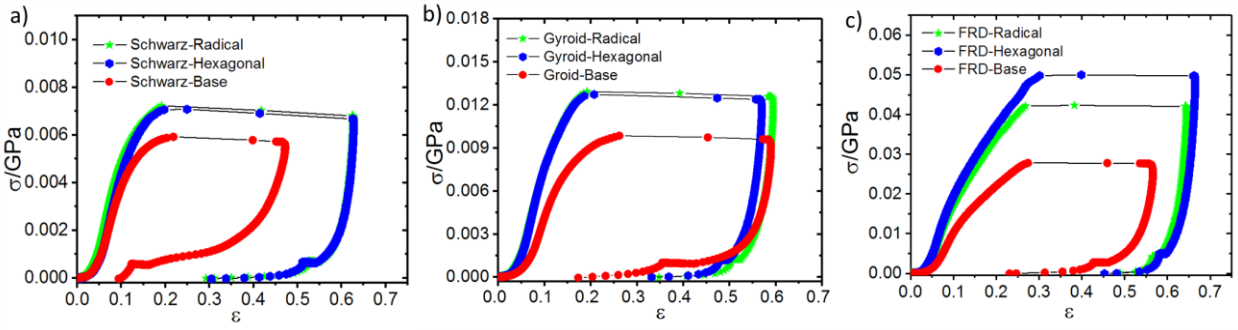

Figure 5.7 Stress-strain curves from micro-sized compression tests on smooth and corrugated TPMS structures. a) SP-base/Rad/Hex; b) Gyroid-base/Rad/Hex; c) FRD-base/Rad/Hex.

From Fig. 5.7, we can observe that the toe-areas of these measured stress-strain curves extend to strains up to around 0.05. During the test of compression, a strain of 0.05 of the structures is equivalent to a displacement of 1.4 μm. As aforementioned, such toe-areas exist when the flat punch is gradually engaging the entire top surface of the tested structure. It takes around 2° of angle mismatch for a 40 μm sized structure to allow 1.4 μm mismatch in height. Such angle mismatch can either come from the flat punch surface or the structure itself. Still, in the gyroid and FRD structures, it is observed that the base structures have toe-areas that stretch for larger strains compared to the corresponding corrugated Rad or Hex structures. While in the case of SP structures, the base, Rad or Hex structures have similar toe-areas. We infer that the reason is that the edges on the top surface of the gyroid and FRD structures have free ends, while the top edges of the SP structures are closed circles. These free ends on edges make the structure susceptible to early bending specifically at their locations, which could further extend the strain of toe-areas. In this sense, the shorter toe-areas in the corrugated gyroid and FRD structures imply that the early bending at the free ends of the top edges are suppressed by the corrugated sub-structures.

The Young's modulus values of the tested structures are derived from the elastic region of the stress-strain curves, concluded in Fig. 5.8. As a reference value, we also included the theoretical Young's modulus values of SP, gyroid and FRD shells of the same densities (based on the

numerical results in the previous chapter) in Fig. 5.8. It can be seen from the figure that the measured Young's modulus values of Rad and Hex structures are higher than the values of corresponding base structures. Specifically, SP-Rad's Young's modulus is 14% higher than SP-Base's; SP-Hex's Young's modulus is 19% higher than SP-Base's. Similarly, the increase of Young's modulus against the TPMS counterpart is 33% for Gyroid-Rad, 38% for Gyroid-Hex, 63% for FRD-Rad and 55% for FRD-Hex.

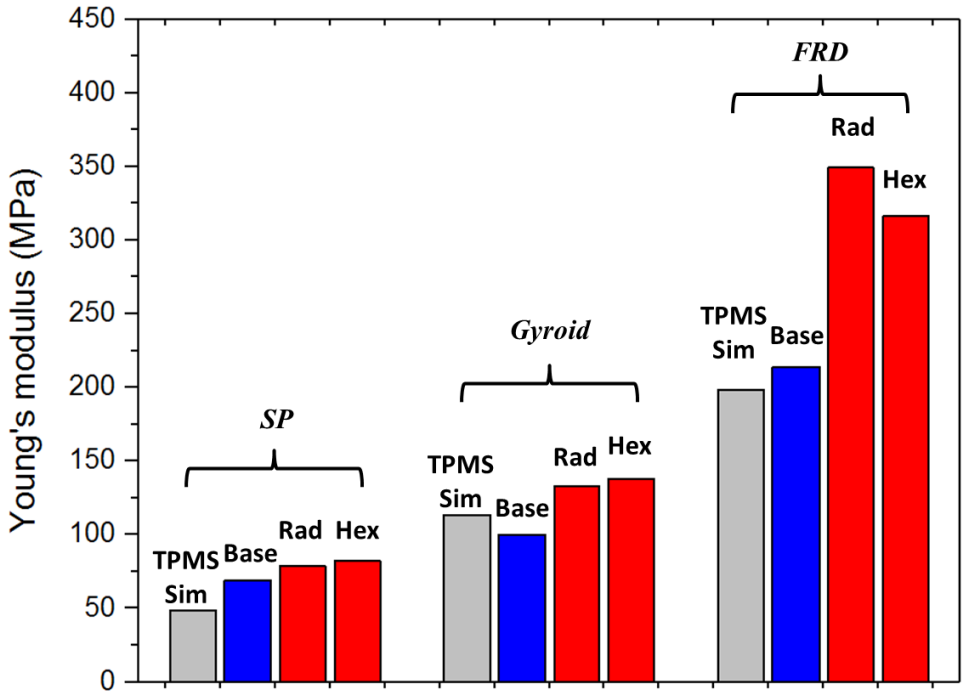

Figure 5.8 Histogram of measured Young's moduli of smooth and corrugated TPMS structures. Theoretical Young's moduli of TPMSs are shown as references.

Compared to the corresponding theoretical Young's modulus values of TPMS shells, the Gyroid-Base and FRD-Base structures have lower measured Young's modulus; meanwhile, the SP-Base have a higher measured Young's modulus. We infer that there are two competing factors that lead to either higher or lower measured Young's modulus values. The first factor is that, the imperfections in printing (i.e. shape distortion, surface dents) and in compression test (i.e. angular mismatch) can lead to lower measured Young's modulus. These imperfections can cause early bending within a structure, which eventually can reduce the measured stiffness. The second factor, which could lead to higher measured Young's modulus, is related to the compression method. During the compression, the bottom of the structure is adhered to the glass substrate and the top

of the structure is contacting the flat indenter surface, affected by friction forces. These boundary conditions tend to restrain the lateral expansion of the structure during compression. All the structures are compressed in their (100) direction. The (100) direction is a weak direction for SP shells, where a Poisson's ratio > 0.4 (based on the calculation in the previous chapter) can be expected. With a large Poisson's ratio, the lateral constraints could cause a high increase of measured stiffness. According to the data in Fig. 5.8, the second factor is more dominant for the SP and FRD structures, causing higher measured Young's moduli of SP-Base and FRD-Base than their theoretical values.

5.3.3 Plastic behavior and failure

During the plastic region of the original and corrugated TPMS structures, a hardening process is observed. After reaching the yield point, the structures are still far from crushed. According to several literatures, the cured IP-dip under compression represent a mild strain-hardening mechanical property (Hsieh et al. 2019; Meza et al. 2015). The compressive strength is generally 20%-30% higher than the yield point. However, it is possible that the effective plastic behavior of a 3D IP-dip structure can be altered depending on its design. The printed smooth or corrugated TPMSs in this work has failure strengths which are more than twice as high as their yield points. It is reasonable to infer that such strain-hardening plastic behavior of the printed TPMSs is related not only to the intrinsic mechanical property of the cured IP-dip, but also to the spatial geometry of the compressed structures.

Fig. 5.9 plots the yield point and final failure strength of the smooth and corrugated TPMS structures. We can see that the increase of yield strength of corrugated TPMS against the TPMS counterpart is 24% for SP-Rad, 21% for SP-Hex, 37% for Gyroid-Rad, 35% for Gyroid-Hex, 30% for FRD-Rad and 24% for FRD-Hex. While the increase of failure strength of corrugated TPMS against the TPMS counterpart is 22% for SP-Rad, 20% for SP-Hex, 33% for Gyroid-Rad, 30% for Gyroid-Hex, 79% for FRD-Rad and 51% for FRD-Hex. Generally speaking, both the yield strength and failure strength of the TPMS structures are significantly enhanced by the introduction of the corrugated sub-structures. Note that such introduction does not necessarily mean an as significant increase in the effective volume density of the structures. The percentages of strength increase are all within the range of 20-40% except for the cases for the failure strengths of FRD-Rad and FRD-Hex, in which the percentages of increase are beyond 50%. Such outstanding

increasement values are attributed to the exceptionally large failure strains of the FRD-Rad and FRD-Hex. Their failure strains are beyond 0.2, which are not seen in the corrugated SP or gyroid structures.

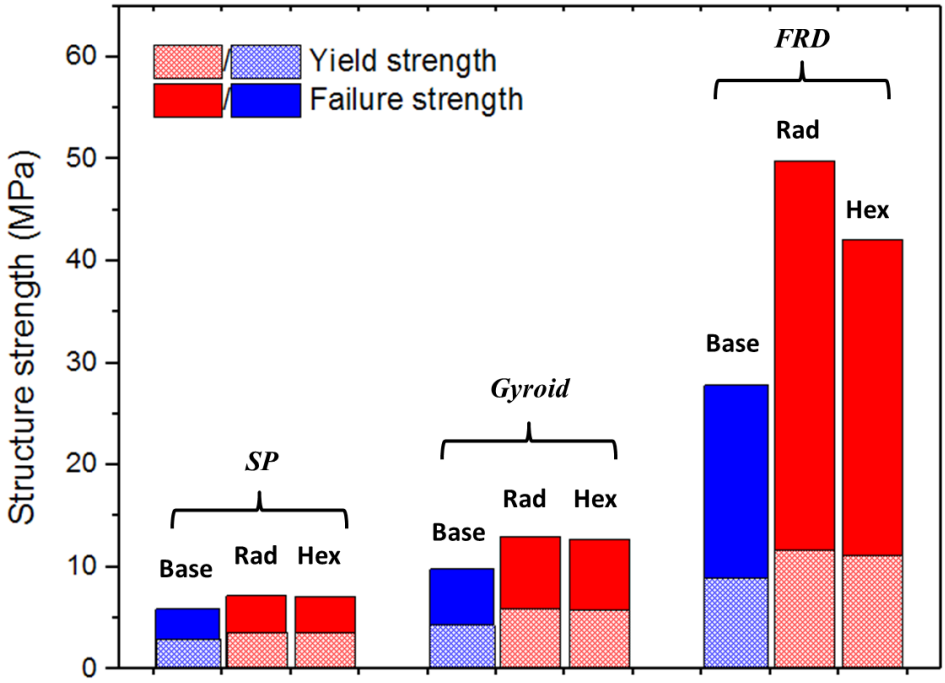

Figure 5.9 Histogram of measured yield strength and failure strength of smooth and corrugated TPMS structures.

We also calculate the average post-yielding stiffness (calculated based on the range from the yield point to the failure point), as shown in Fig. 5.10. The meaning of the average post yielding stiffness providing a measure of the rate for the structure to lose its stiffness as the plastic strain progresses. This terminology is often used in the cases where vibration need to be damped by a plastic hysteresis of a device, for example, a buckling-restrained braces (BRBs) (Gray et al. 2014). It is found that the increase of average post-yielding stiffness of corrugated TPMS against the TPMS counterpart is 45% for SP-Rad, 48% for SP-Hex, 90% for Gyroid-Rad, 100% for Gyroid-Hex, 60% for FRD-Rad and 54% for FRD-Hex.

This can be explained as the bending behavior is significantly hindered in the corrugated TPMSs compared to the smooth TPMSs. As mentioned in the previous section, local bending behavior exists in the elastic range of smooth TPMS structures. These local spots should continue to deform in a bending manner as the structure enters the plastic region. Because these bending

deformations allow for larger local displacement before the final failure point is reached. As a result, to achieve a certain amount of effect strain on the structure, a larger force needs to be loaded on the corrugated structures compared to the smooth ones. This also can explain that the corrugated SP and gyroid structures appear to be more 'brittle', despite the reinforcement effect of the corrugated sub-structures. Meanwhile, it is worth noting that the 'embrittlement' effect caused by the corrugated sub-structure is not seen in the FRD TPMSs. We infer this is related to the intrinsic deformation behavior of the TPMS structure of FCC symmetry. A more comprehensive explanation of this phenomenon may require future research involving in-situ videotaping of the micro-compression test.

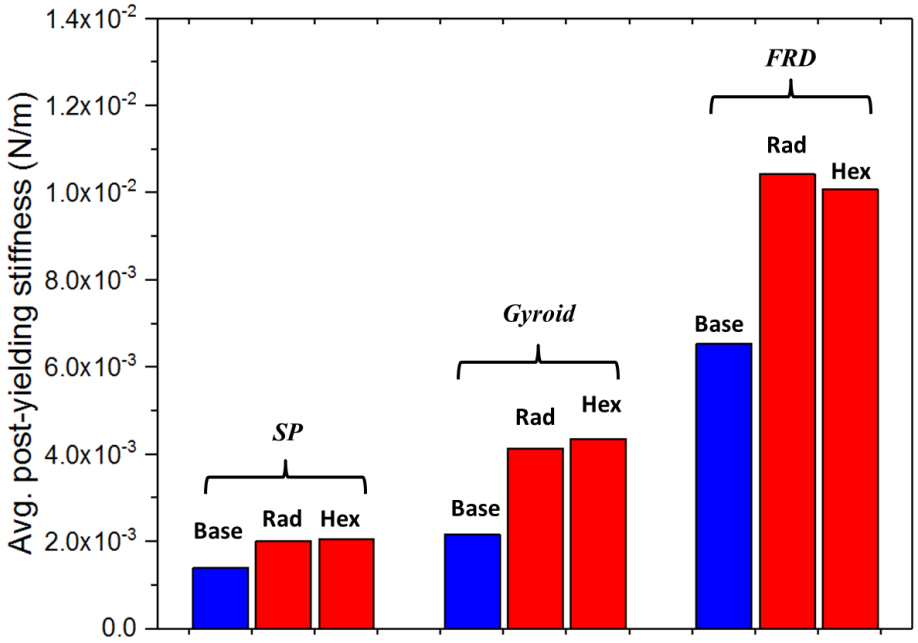

Figure 5.10 Histogram of calculated average post-yielding stiffnesses of smooth and corrugated TPMS structures.

The failure morphologies of the smooth and corrugated structures are also significantly different. According to an existing report, the cured IP-dip exhibit hyperelastic properties to a certain extent. Based on the failure morphologies in Fig. 5.11, it can be seen that the base structures are still standing up with nearly the same shape as before compression. Only a few long cracks are seen on the structures. It can be inferred that after the crack propagation and failure of the base structures, significant elastic bending is still present while the structures are compressed. This is possible because of the hyperelastic property of the cured IP-dip (Lemma et al. 2017). Meanwhile,

the compressed Rad and Hex structures are all fragmented after mechanical failure. According to the failure morphology, the crack propagation directions are clearly affected by the sub-structure orientations on the corrugated Rad and Hex structures. It is inferred that the plastic strain distribution is largely affected by the corrugated sub-structures in the compressed states. The orientation of the high plastic strain region is likely altered by the existence of the corrugated sub-structures. As a result, the Rad and Hex structures have shorter and denser cracks, which eventually split the structures to broken pieces. Roughly speaking, the smaller the broken pieces are, the denser the cracks should be. The sizes of the failure structure pieces are ranked as: SP-Rad/Hex > Gyroid-Rad/Hex > FRD-Rad/Hex.

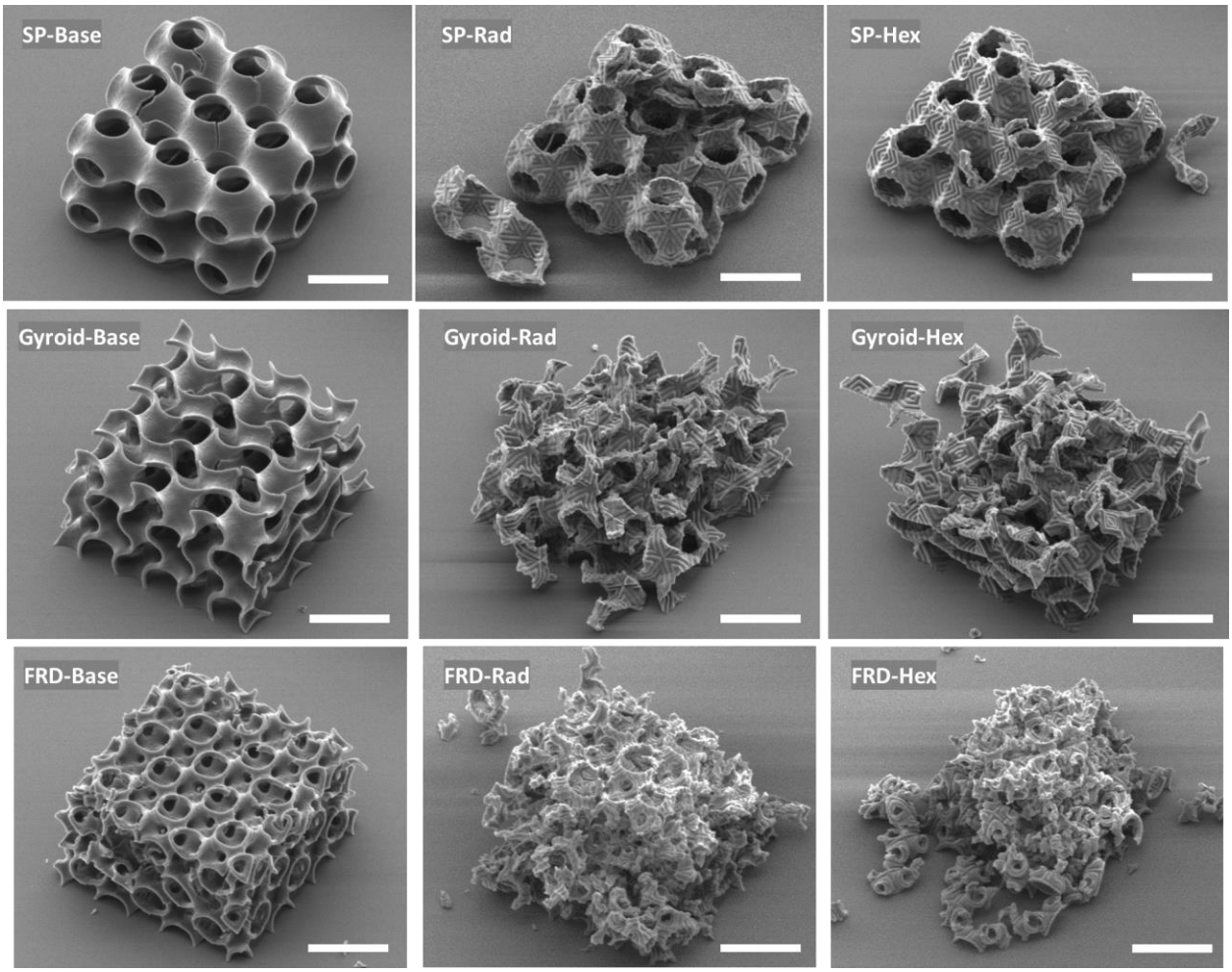

Figure 5.11 SEM images of after-failure morphologies of smooth and corrugated TPMS structures. Scale bar: 10 μm.

5.3.4 The reinforcement effect of ceramic shells

It is not an uncommon technique to reinforce 3D printed polymeric cellular structures with ceramic shells. It has been reported by many that by applying an ALD ceramic shell on polymeric lattices, the stiffness and strength of the structures can be boosted significantly (Jens Bauer et al. 2014; Meza et al. 2015). Since the lattices reinforced by the ALD coating are consisted mostly of cylindrical struts, the coated ceramic layer was mostly in form of cylindrical shells. These shells significantly increase the stiffness of the struts and suppressed their buckling behavior. The ceramic reinforced polymeric lattices are often more brittle compared the non-reinforced ones.

Here, ALD ceramic coating is performed on the smooth and corrugated TPMS prints. Their mechanical performances are examined using the same nanoindentation approach. Note that the coated ceramic layer is either smooth or corrugated shells which are offset for half of the polymer wall thickness from the original TPMSs.

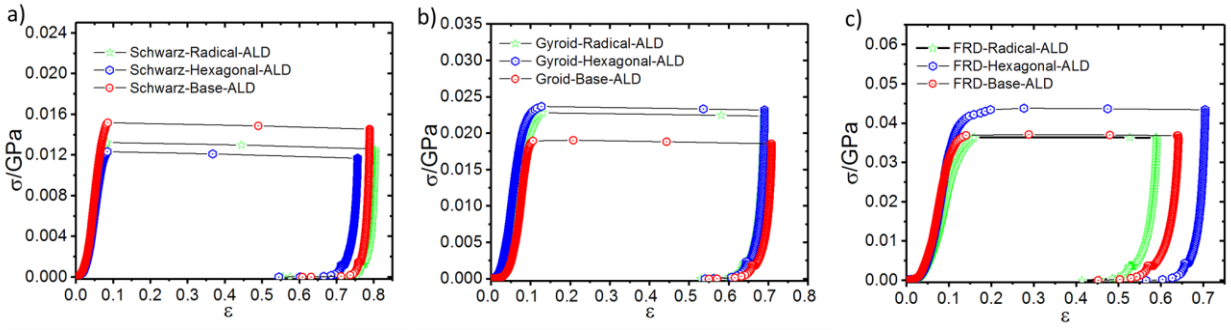

Figure 5.12 Stress-strain curves from micro-sized compression tests on ALD ceramic layer reinforced smooth and corrugated TPMS structures. a) SP-base/Rad/Hex; b) Gyroid-base/Rad/Hex; c) FRD-base/Rad/Hex.

It can be seen from Fig. 5.12, that the shapes of the stress-strain curves are significantly different from the un-coated structures. Firstly, the yield strengths of the structures are all improved. Secondly, the plastic strain hardening regions are becoming negligible, meaning that the failures of the structures come shortly after the yield points are reached. Interestingly, the ALD layer is effective in improving the stiffness of the smooth TPMS structures, just as many other papers reported. However, the ALD layer is not as effective in improving the stiffness of the corrugated TPMS structures. Notably, the uncoated corrugated FRD structures have comparable elastic stiffness with the ALD coated corrugated FRD structures. This is possibly due to the

overlapped stiffening mechanism, which relies on generating stiffer surfaces and resisting bending, of these two strategies.

Moreover, the after-failure morphologies (Fig. 5.13) of all coated TPMSs show catastrophic failure like the uncoated corrugated gyroid and FRD structures. The debris after the compression failure consists of many small fragmented pieces of the original structure. This is another evidence that large local bending is not possible for the ALD ceramic coated structures because of the brittle ceramic layer on top of the surfaces, which will crack at smaller strains compared to polymers. These cracks on the ceramic shells are likely to induce the inner polymer to fracture due to local stress concentrations. On the other hand, the similarity in after-failure morphologies suggests that the corrugated sub-structures and the ALD ceramic coating could have similar strengthening mechanisms regarding the TPMS shaped mechanical metamaterials.

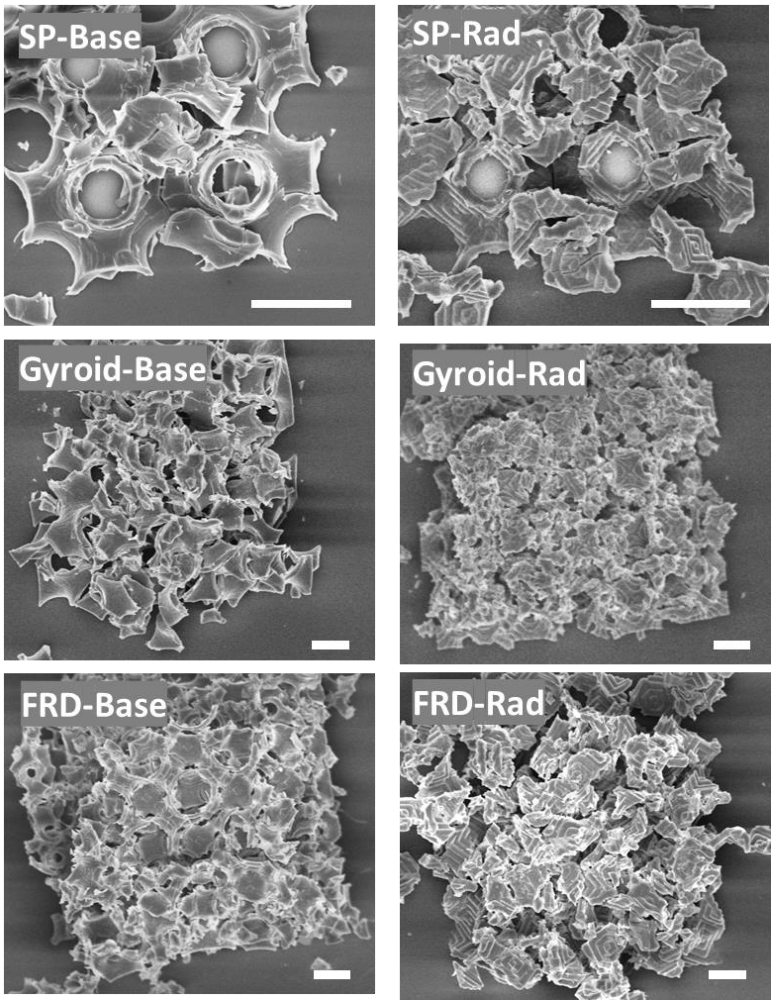

Figure 5.13 SEM images of after-failure morphologies of ALD ceramic coated smooth and corrugated TPMS structures. Scale bar: 5 μm.

5.3.5 Comparison with other mechanical metamaterials

Here we plot our smooth and corrugated TPMS structures in the Ashby plots of the relative modulus and strength over the volumetric density. In Fig. 5.14, regarding the ratios of normalized Young' modulus over volume density, it can be calculated from the 9 types of printed structures in this work that they span a range of 0.22-0.72, with the SP-Base being the lowest case and the FRD-Rad being the highest case. Within the 0.1-0.2 volume density range, the SP-Base/Rad/Hex, Gyroid-Base/Rad/Hex and FRD-base structures has comparable relative Young's moduli and relative failure strength with the current best reported light weight stiff architected materials (3D printed metal TPMSs and glassy carbon nanolattices). While the FRD-Rad and FRD-Hex structures outperforms the reported 3D printed metal TPMSs and glassy carbon nanolattices in terms of relative Young's moduli and relative failure strength at their volume densities.

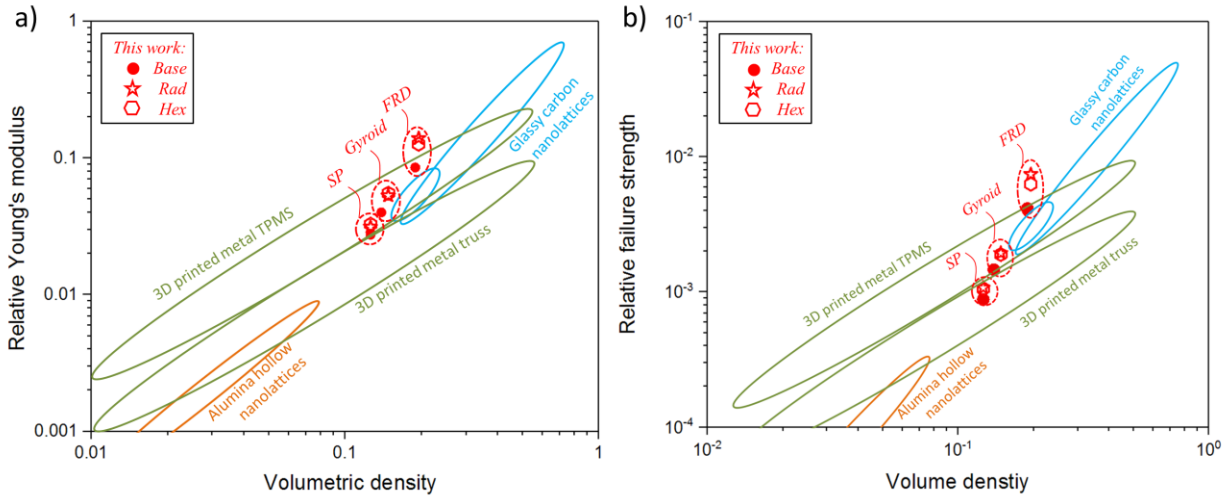

Figure 5.14 Comparison of the a) relative Young's moduli and b) relative failure strength between the smooth and corrugated TPMS structures in this work and a few cellular mechanical metamaterials reported elsewhere (J. Bauer et al. 2016; Bonatti and Mohr 2019b; Meza, Das, and Greer 2014; X. Zhang, Vyatskikh, et al. 2019).

5.3.6 Conclusion

In this work, we developed a method to introduce second-order corrugated sub-structures on the smooth surface of TPMSs, in aim of stiffening and strengthening the smooth TPMS structures. This approach is experimentally validated via the mechanical tests on high precision nanoscale 3D prints. As a result, the enhancement of the corrugated TPMSs compared to smooth ones can go up

to 63% in Young's modulus, 37% in yield strength and 79% in failure strength. These improvements are attributed to the suppression of early or local bending on the TPMS structures due to the corrugated sub-structures. The improvement of the after-yielding stiffness and the crack distribution in the failure morphology proves that the corrugated sub-structures effectively change the plastic behavior of the TPMS structures. Thanks to the reinforcement effect from the corrugated sub-structures on the TPMSs, the best corrugated TPMS structure outperforms the currently reported light weight mechanical metamaterials in terms of relative Young's moduli and relative failure strength over the volume density of 0.1-0.2.

6. CONCLUSIONS

6.1 Summary

In this thesis, we used experimental and numerical approaches to study three types of mechanical metamaterials: i) composite bending dominated HLs; ii) TPMSs and eTPMSs; iii) corrugated TPMSs. Generally, we have demonstrated a few strategies in designing and improving the specific stiffness or strength via these examples of mechanical metamaterials. By introducing carbon/ceramic composite in the bending dominated HLs, we proved the effectiveness of using the composite layered material against the single layer ceramic. While studying the nature of TPMS, we discovered that they were stretch dominated under isotropic deformation with no stress concentrations within the shell structure. This meant that they had an optimal specific bulk modulus approaching the H-S upper bound. Next, we proposed a strategy to smoothly connect the zero-mean-curvature surfaces in TPMSs with the extension of zero-Gaussion-curvature surfaces, forming new 'eTPMSs". These new shellular structure could have improved specific Young's modulus along their stiffest orientation compared to their TPMS base structures. Lastly, we proposed and experimented a strategy of introducing corrugated sub-structures to existing TPMSs to improve their mechanical properties, such as Young's modulus, yield strength and failure strength in compression. We found out that the corrugated sub-structure can effectively suppress the local bending behavior and redirect crack propagation while such structures were under uniaxial compression.

6.2 Outlook and Future Studies

6.2.1 Other Candidate Structures

Self-intersected shellular structures are also promising candidates in the race of higher specific mechanical properties. The intersection line where two plates or curved shells meets could potential boost the mechanical property of the overall structure by suppressing bending or buckling. Another category of potential candidates in these mechanical metamaterials is the structural composite. One can refer to a polycrystal structure while replacing the differently orientated grains with differently orientated lattice metamaterials or TPMS materials. Once their boundaries can be dealt with care, these structural composites could realize strengthening

strategies in crystallography science, such as the strengthening effects induced by dislocations, precipitates or twinnings. No doubt unexplored mechanisms could also be discovered along the way.

6.2.2 Other Metamaterial Properties

Other metamaterial properties are also attractive. Foldable, deployable structures can be of great use in medical and aerospace applications. In order to reach foldable and deployable structures, one can generate origami structures on shellular materials. It is possible to discover a corrugation pattern that can fold infinite periodic shellular structures. On the other hand, acoustic metamaterials always have broad impact on sound or vibration attenuation applications. The numerical models built in this thesis are readily useful in predicting the acoustic structure of periodic shellular materials, like their phononic bands, given that the periodic boundary conditions are substituted with Bloch boundary conditions. Various method can be designed in tuning the phononic bands of periodic structures presented in this thesis, which will finally make these structures useful in real-life applications.

REFERENCES

Abueidda, Diab W. et al. 2017. “Mechanical Properties of 3D Printed Polymeric Cellular Materials with Triply Periodic Minimal Surface Architectures.” *Materials and Design*.

Al-Ketan, Oraib et al. 2018. “Microarchitected Stretching-Dominated Mechanical Metamaterials with Minimal Surface Topologies.” *Advanced Engineering Materials* 20(9).

Al-Ketan, Oraib, Rashid K. Abu Al-Rub, and Reza Rowshan. 2018. “The Effect of Architecture on the Mechanical Properties of Cellular Structures Based on the IWP Minimal Surface.” *Journal of Materials Research* 33(3): 343–59.

Al-Ketan, Oraib, Reza Rowshan, and Rashid K. Abu Al-Rub. 2018. “Topology-Mechanical Property Relationship of 3D Printed Strut, Skeletal, and Sheet Based Periodic Metallic Cellular Materials.” *Additive Manufacturing* 19: 167–83. http://dx.doi.org/10.1016/j.addma.2017.12.006.

Ashby, M. F. 2006. “The Properties of Foams and Lattices.” *Philosophical Transactions of the Royal Society A: Mathematical, Physical and Engineering Sciences* 364(1838): 15–30.

Ball, Vincent, Doriane Del Frari, Valérie Toniazzo, and David Ruch. 2012. “Kinetics of Polydopamine Film Deposition as a Function of PH and Dopamine Concentration: Insights in the Polydopamine Deposition Mechanism.” *Journal of Colloid and Interface Science*.

Bauer, J., A. Schroer, R. Schwaiger, and O. Kraft. 2016. “Approaching Theoretical Strength in Glassy Carbon Nanolattices.” *Nature Materials* 15(4): 438–43.

Bauer, Jens et al. 2014. “High-Strength Cellular Ceramic Composites with 3D Microarchitecture.” *Proceedings of the National Academy of Sciences of the United States of America* 111(7): 2453–58.

———. 2017. “Nanolattices: An Emerging Class of Mechanical Metamaterials.” *Advanced Materials*.

Berger, J. B., H. N.G. Wadley, and R. M. McMeeking. 2017. “Mechanical Metamaterials at the Theoretical Limit of Isotropic Elastic Stiffness.” *Nature* 543(7646): 533–37. http://dx.doi.org/10.1038/nature21075.

Bertoldi, Katia, Vincenzo Vitelli, Johan Christensen, and Martin Van Hecke. 2017. “Flexible Mechanical Metamaterials.” *Nature Reviews Materials* 2.

Bi, Hui, I. Wei Chen, Tianquan Lin, and Fuqiang Huang. 2015. “A New Tubular Graphene Form of a Tetrahedrally Connected Cellular Structure.” *Advanced Materials*.

Bonatti, Colin, and Dirk Mohr. 2017. “Large Deformation Response of Additively-Manufactured FCC Metamaterials: From Octet Truss Lattices towards Continuous Shell Mesostructures.” *International Journal of Plasticity* 92: 122–47. http://dx.doi.org/10.1016/j.ijplas.2017.02.003.

———. 2019a. “Mechanical Performance of Additively-Manufactured Anisotropic and Isotropic Smooth Shell-Lattice Materials: Simulations & Experiments.” *Journal of the Mechanics and Physics of Solids*.

———. 2019b. “Smooth-Shell Metamaterials of Cubic Symmetry: Anisotropic Elasticity, Yield Strength and Specific Energy Absorption.” *Acta Materialia* 164: 301–21. https://doi.org/10.1016/j.actamat.2018.10.034.

Bouville, Florian et al. 2014. “Strong, Tough and Stiff Bioinspired Ceramics from Brittle Constituents.” *Nature Materials*.

Bückmann, T. et al. 2014. “An Elasto-Mechanical Unfeelability Cloak Made of Pentamode Metamaterials.” *Nature Communications* 5(May): 1–6.

Bückmann, Tiemo et al. 2012. “Tailored 3D Mechanical Metamaterials Made by Dip-in Direct-Laser-Writing Optical Lithography.” *Advanced Materials* 24(20): 2710–14.

Chabi, Sakineh et al. 2016. “Ultralight, Strong, Three-Dimensional SiC Structures.” *ACS Nano*.

Davami, Keivan et al. 2015. “Ultralight Shape-Recovering Plate Mechanical Metamaterials.” *Nature Communications* 6: 1–7.

Dayyani, I., A. D. Shaw, E. I. Saavedra Flores, and M. I. Friswell. 2015. “The Mechanics of Composite Corrugated Structures: A Review with Applications in Morphing Aircraft.” *Composite Structures* 133: 358–80. http://dx.doi.org/10.1016/j.compstruct.2015.07.099.

Dias, Marcelo A., Levi H. Dudte, L. Mahadevan, and Christian D. Santangelo. 2012. “Geometric Mechanics of Curved Crease Origami.” *Physical Review Letters* 109(11): 1–5.

Dimas, Leon S., and Markus J. Buehler. 2013. “Tough and Stiff Composites with Simple Building Blocks.” *Journal of Materials Research* 28(10): 1295–1303.

Dudte, Levi H., Etienne Vouga, Tomohiro Tachi, and L. Mahadevan. 2016. “Programming Curvature Using Origami Tessellations.” *Nature Materials* 15(5): 583–88.

Eckel, Zak C. et al. 2016. “Additive Manufacturing of Polymer-Derived Ceramics.” *Science* 351(6268): 58–62.

Evans, A. G. et al. 2010. “Concepts for Enhanced Energy Absorption Using Hollow Micro-Lattices.” *International Journal of Impact Engineering* 37(9): 947–59.

Evans, Ken E. 1991. “Auxetic Polymers: A New Range of Materials.” *Endeavour*.

Evans, Thomas A., Robert J. Lang, Spencer P. Magleby, and Larry L. Howell. 2015. “Rigidly Foldable Origami Gadgets and Tessellations.” *Royal Society Open Science* 2(9).

Fang, Nicholas et al. 2006. “Ultrasonic Metamaterials with Negative Modulus.” *Nature Materials*.

Fleck, N. A., V. S. Deshpande, and M. F. Ashby. 2010. “Micro-Architectured Materials: Past, Present and Future.” *Proceedings of the Royal Society A: Mathematical, Physical and Engineering Sciences* 466(2121): 2495–2516.

Fleck, Norman a. 2004. “An Overview of the Mechanical Properties of Foams and Periodic Lattice Materials.” *Cellular Metals and Polymers 2004* (8585858585): 1–4.

Geng, Qiang, Dien Wang, Pengfei Chen, and Shih Chi Chen. 2019. “Ultrafast Multi-Focus 3-D Nano-Fabrication Based on Two-Photon Polymerization.” *Nature Communications* 10(1): 1–7. http://dx.doi.org/10.1038/s41467-019-10249-2.

Gibson, Lorna J. 2005. “Biomechanics of Cellular Solids.” *Journal of Biomechanics* 38(3): 377–99.

Gray, M. G., J. C. De Oliveira, C. Christopoulos, and J. I. Binder. 2014. “Effects of Post-Yield Stiffening and Strengthening on the Collapse Performance of Non-Buckling Braced Frames.” *NCEE 2014 - 10th U.S. National Conference on Earthquake Engineering: Frontiers of Earthquake Engineering*.

Greer, Julia R., and Jeff Th M. De Hosson. 2011. “Plasticity in Small-Sized Metallic Systems: Intrinsic versus Extrinsic Size Effect.” In *Progress in Materials Science*,.

Gurtner, Gérald, and Marc Durand. 2014. “Stiffest Elastic Networks.” *Proceedings of the Royal Society A: Mathematical, Physical and Engineering Sciences* 470(2164).

Han, Lu, and Shunai Che. 2018. “An Overview of Materials with Triply Periodic Minimal Surfaces and Related Geometry: From Biological Structures to Self-Assembled Systems.” *Advanced Materials*.

Han, Seung Chul, and Kiju Kang. 2019. “Another Stretching-Dominated Micro-Architectured Material, Shellular.” *Materials Today* xxx(xx): 1–8. https://doi.org/10.1016/j.mattod.2019.05.018.

Han, Seung Chul, Jeong Woo Lee, and Kiju Kang. 2015. “A New Type of Low Density Material: Shellular.” *Advanced Materials*.

Hashin, Z., and S. Shtrikman. 1963. “A Variational Approach to the Theory of the Elastic Behaviour of Multiphase Materials.” *Journal of the Mechanics and Physics of Solids*.

Hsieh, Meng Ting et al. 2019. “The Mechanical Response of Cellular Materials with Spinodal Topologies.” *Journal of the Mechanics and Physics of Solids* 125: 401–19. https://doi.org/10.1016/j.jmps.2019.01.002.

INGEL, ROBERT P., and DAVID LEWIS III. 1988. “Elastic Anisotropy in Zirconia Single Crystals.” *Journal of the American Ceramic Society*.

Jiang, Bin et al. 2015. “Ultralight Metal Foams.” *Scientific Reports*.

Jiang, Yanhui, and Qiming Wang. 2016. “Highly-Stretchable 3D-Architected Mechanical Metamaterials.” *Scientific Reports* 6(May): 1–11. http://dx.doi.org/10.1038/srep34147.

Jin, Bo, En Mei Jin, Kyung Hee Park, and Hal Bon Gu. 2008. “Electrochemical Properties of LiFePO4-Multiwalled Carbon Nanotubes Composite Cathode Materials for Lithium Polymer Battery.” *Electrochemistry Communications*.

Karcher, Hermann, and Konrad Polthier. 1996. “Construction of Triply Periodic Minimal Surfaces.” *Philosophical Transactions of the Royal Society A: Mathematical, Physical and Engineering Sciences* 354(1715): 2077–2104.

Kim, Byungkyu, Deok Ho Kim, Jaehoon Jung, and Jong Oh Park. 2005. “A Biomimetic Undulatory Tadpole Robot Using Ionic Polymer-Metal Composite Actuators.” *Smart Materials and Structures*.

Kobayashi, H., B. Kresling, and J. F.V. Vincent. 1998. “The Geometry of Unfolding Tree Leaves.” *Proceedings of the Royal Society B: Biological Sciences* 265(1391): 147–54.

Krödel, Sebastian, and Chiara Daraio. 2016. “Microlattice Metamaterials for Tailoring Ultrasonic Transmission with Elastoacoustic Hybridization.” *Physical Review Applied* 6(6): 1–9.

Kshetrimayum, Rakhesh S. 2004. “A Brief Intro to Metamaterials.” *IEEE Potentials*.

Lakes, Roderic. 1987. “Foam Structures with a Negative Poisson’s Ratio.” *Science*.

———. 1993. “Materials with Structural Hierarchy.” *Nature*.

Launey, Maximilien E., Markus J. Buehler, and Robert O. Ritchie. 2010. “On the Mechanistic Origins of Toughness in Bone.” *Annual Review of Materials Research*.

Lebée, Arthur. 2015. “From Folds to Structures, a Review.” *International Journal of Space Structures* 30(2): 55–74.

Lee, Bruce P., P.B. Messersmith, J.N. Israelachvili, and J.H. Waite. 2011. “Mussel-Inspired Adhesives and Coatings.” *Annual Review of Materials Research*.

Lee, Haeshin, Shara M. Dellatore, William M. Miller, and Phillip B. Messersmith. 2007. “Mussel-Inspired Surface Chemistry for Multifunctional Coatings.” *Science*.

Lee, Jae Hwang, Jonathan P. Singer, and Edwin L. Thomas. 2012. “Micro-/Nanostructured Mechanical Metamaterials.” *Advanced Materials*.

Lee, Yi Seul et al. 2016. “A Remote-Controlled Generation of Gold@polydopamine (Core@shell) Nanoparticles via Physical-Chemical Stimuli of Polydopamine/Gold Composites.” *Scientific Reports*.

Lemma, Enrico Domenico et al. 2017. “Mechanical Properties Tunability of Three-Dimensional Polymeric Structures in Two-Photon Lithography.” *IEEE Transactions on Nanotechnology* 16(1): 23–31.

Li, Ben et al. 2009. “Ultrathin and Stable Active Layer of Dense Composite Membrane Enabled by Poly(Dopamine).” *Langmuir*.

Li, Jensen et al. 2009. “Experimental Demonstration of an Acoustic Magnifying Hyperlens.” *Nature Materials*.

Li, Suzhi et al. 2016. “The Evolving Quality of Frictional Contact with Graphene.” *Nature*.

Liu, Zhengyou et al. 2000. “Locally Resonant Sonic Materials.” *Science* 289(5485): 1734 LP – 1736. http://science.sciencemag.org/content/289/5485/1734.abstract.

Masood, Syed H. 1996. “Intelligent Rapid Prototyping with Fused Deposition Modelling.” *Rapid Prototyping Journal*.

Maxwell, J. Clerk. 1864. “ XLV. On Reciprocal Figures and Diagrams of Forces .” *The London, Edinburgh, and Dublin Philosophical Magazine and Journal of Science*.

Meza, Lucas R. et al. 2015. “Resilient 3D Hierarchical Architected Metamaterials.” *Proceedings of the National Academy of Sciences of the United States of America* 112(37): 11502–7.

———. 2017. “Reexamining the Mechanical Property Space of Three-Dimensional Lattice Architectures.” *Acta Materialia* 140: 424–32. https://doi.org/10.1016/j.actamat.2017.08.052.

Meza, Lucas R., Satyajit Das, and Julia R. Greer. 2014. “Strong, Lightweight, and Recoverable Three-Dimensional Ceramic Nanolattices.” *Science* 345(6202): 1322–26.

Meza, Lucas R., and Julia R. Greer. 2014. “Mechanical Characterization of Hollow Ceramic Nanolattices.” *Journal of Materials Science*.

Mieszala, Maxime et al. 2017. “Micromechanics of Amorphous Metal/Polymer Hybrid Structures with 3D Cellular Architectures: Size Effects, Buckling Behavior, and Energy Absorption Capability.” *Small* 13(8): 1–13.

Milton, Graeme W., and Andrej V. Cherkaev. 1995. “Which Elasticity Tensors Are Realizable?” *Journal of Engineering Materials and Technology, Transactions of the ASME*.

Moner-Girona, M. et al. 2002. “Micromechanical Properties of Carbon-Silica Aerogel Composites.” *Applied Physics A: Materials Science and Processing* 74(1): 119–22.

Moutos, Franklin T., Lisa E. Freed, and Farshid Guilak. 2007. “A Biomimetic Three-Dimensional Woven Composite Scaffold for Functional Tissue Engineering of Cartilage.” *Nature Materials*.

Munch, E. et al. 2008. “Tough, Bio-Inspired Hybrid Materials.” *Science*.

Muth, Joseph T. et al. 2017. “Architected Cellular Ceramics with Tailored Stiffness via Direct Foam Writing.” *Proceedings of the National Academy of Sciences of the United States of America* 114(8): 1832–37.

Norman, A. D., K. A. Seffen, and S. D. Guest. 2008. “Multistable Corrugated Shells.” *Proceedings of the Royal Society A: Mathematical, Physical and Engineering Sciences*.

———. 2009. “Morphing of Curved Corrugated Shells.” *International Journal of Solids and Structures* 46(7–8): 1624–33. http://dx.doi.org/10.1016/j.ijsolstr.2008.12.009.

Ou, Junfei et al. 2011. “Mechanical Property and Corrosion Resistance of Zirconia/Polydopamine Nanocomposite Multilayer Films Fabricated via a Novel Non-Electrostatic Layer-by-Layer Assembly Technique.” *Surface and Interface Analysis*.

Parnell, Charlette M. et al. 2016. “Polydopamine-Coated Manganese Complex/Graphene Nanocomposite for Enhanced Electrocatalytic Activity Towards Oxygen Reduction.” *Scientific Reports*.

Plateau, J. 1873. “Experimental and Theoretical Statics of Liquids Subject to Molecular Forces Only.” *English*: 1–427. http://scholar.google.com/scholar?hl=en&btnG=Search&q=intitle:EXPERIMENTAL+AND+THEORETICAL+STATICS+OF+LIQUIDS+subject+to+molecular+forces+only#0%5Cnhttp://scholar.google.com/scholar?hl=en&btnG=Search&q=intitle:Experimental+and+theoretical+statics+of+liqui.

Poco, J. F., J. H. Satcher, and L. W. Hrubesh. 2001. “Synthesis of Alumina Aerogel.” *Journal of Non-Crystalline Solids* 285(1–3): 57–63.

Portela, Carlos M., Julia R. Greer, and Dennis M. Kochmann. 2018. “Impact of Node Geometry on the Effective Stiffness of Non-Slender Three-Dimensional Truss Lattice Architectures.” *Extreme Mechanics Letters*.

Ramamurthy, P. C. et al. 2003. “Polyaniline/Single-Walled Carbon Nanotube Composite Electronic Device.” In *2003 International Semiconductor Device Research Symposium, ISDRS 2003 - Proceedings,*.

Restrepo, S. et al. 2017. “Mechanical Properties of Ceramic Structures Based on Triply Periodic Minimal Surface (TPMS) Processed by 3D Printing.” *Journal of Physics: Conference Series* 935(1).

Schaedler, T. A. et al. 2011a. “Ultralight Metallic Microlattices.” *Science*.

———. 2011b. “Ultralight Metallic Microlattices.” *Science* 334(6058): 962–65.

Schaedler, Tobias A., and William B. Carter. 2016. “Architected Cellular Materials.” *Annual Review of Materials Research* 46(1): 187–210.

Schenk, Mark, and Simon D. Guest. 2013. “Geometry of Miura-Folded Metamaterials.” *Proceedings of the National Academy of Sciences of the United States of America* 110(9): 3276–81.

Schoen, Alan H. 1970. “Infinite Periodic Minimal Surfaces without Self-Intersections.” *Nasa Technical Note D-5541*.

———. 2012. “Reflections Concerning Triply-Periodic Minimal Surfaces.” *Interface Focus* 2(5): 658–68.

Seffen, K. A. 2012. “Compliant Shell Mechanisms.” *Philosophical Transactions of the Royal Society A: Mathematical, Physical and Engineering Sciences* 370(1965): 2010–26.

Shan, Sicong et al. 2015. “Multistable Architected Materials for Trapping Elastic Strain Energy.” *Advanced Materials*.

Silverberg, Jesse L. et al. 2014. “Using Origami Design Principles to Fold Reprogrammable Mechanical Metamaterials.” *Science*.

Smith, D. R., J. B. Pendry, and M. C.K. Wiltshire. 2004. “Metamaterials and Negative Refractive Index.” *Science*.

Speck, Thomas, and Ingo Burgert. 2011. “Plant Stems: Functional Design and Mechanics.” *Annual Review of Materials Research*.

Sullivan, Tarah N., Bin Wang, Horacio D. Espinosa, and Marc A. Meyers. 2017. “Extreme Lightweight Structures: Avian Feathers and Bones.” *Materials Today* 20(7): 377–91. http://dx.doi.org/10.1016/j.mattod.2017.02.004.

Surjadi, James Utama et al. 2019. “Mechanical Metamaterials and Their Engineering Applications.” *Advanced Engineering Materials*.

Tancogne-Dejean, Thomas et al. 2018. “3D Plate-Lattices: An Emerging Class of Low-Density Metamaterial Exhibiting Optimal Isotropic Stiffness.” *Advanced Materials*.

Tancogne-Dejean, Thomas, and Dirk Mohr. 2018a. “Elastically-Isotropic Truss Lattice Materials of Reduced Plastic Anisotropy.” *International Journal of Solids and Structures* 138: 24–39. https://doi.org/10.1016/j.ijsolstr.2017.12.025.

———. 2018b. “Stiffness and Specific Energy Absorption of Additively-Manufactured Metallic BCC Metamaterials Composed of Tapered Beams.” *International Journal of Mechanical Sciences* 141: 101–16.

Tang, Zhiyong, Nicholas A. Kotov, Sergei Magonov, and Birol Ozturk. 2003. “Nanostructured Artificial Nacre.” *Nature Materials*.

Truby, Ryan L., and Jennifer A. Lewis. 2016. “Printing Soft Matter in Three Dimensions.” *Nature*.

Valdevit, Lorenzo et al. 2013. “Compressive Strength of Hollow Microlattices: Experimental Characterization, Modeling, and Optimal Design.” *Journal of Materials Research* 28(17): 2461–73.

Veedu, Vinod P. et al. 2006. “Multifunctional Composites Using Reinforced Laminae with Carbon-Nanotube Forests.” *Nature Materials*.

Wegst, Ulrike G.K. et al. 2015. “Bioinspired Structural Materials.” *Nature Materials* 14(1): 23–36.

Worsley, Marcus A. et al. 2009. “Mechanically Robust and Electrically Conductive Carbon Nanotube Foams.” *Applied Physics Letters*.

Wortman, J. J., and R. A. Evans. 1965. “Young’s Modulus, Shear Modulus, and Poisson’s Ratio in Silicon and Germanium.” *Journal of Applied Physics* 36(1): 153–56.

Xia, Y., M. I. Friswell, and E. I Saavedra Flores. 2012. “Equivalent Models of Corrugated Panels.” *International Journal of Solids and Structures* 49(13): 1453–62. http://dx.doi.org/10.1016/j.ijsolstr.2012.02.023.

Xu, Xiang et al. 2019. “Double-Negative-Index Ceramic Aerogels for Thermal Superinsulation.” *Science*.

Yap, C. Y. et al. 2015. “Review of Selective Laser Melting: Materials and Applications.” *Applied Physics Reviews*.

Yu, Aiping et al. 2007. “Graphite Nanoplatelet-Epoxy Composite Thermal Interface Materials.” *Journal of Physical Chemistry C*.

Zadpoor, Amir A. 2016. “Mechanical Meta-Materials.” *Materials Horizons*.

Zhai, Zirui, Yong Wang, and Hanqing Jiang. 2018. “Origami-Inspired, on-Demand Deployable and Collapsible Mechanical Metamaterials with Tunable Stiffness.” *Proceedings of the National Academy of Sciences of the United States of America*.

Zhang, Qiangqiang et al. 2016. “Hyperbolically Patterned 3D Graphene Metamaterial with Negative Poisson’s Ratio and Superelasticity.” *Advanced Materials*.

———. 2017. “Flyweight, Superelastic, Electrically Conductive, and Flame-Retardant 3D Multi-Nanolayer Graphene/Ceramic Metamaterial.” *Advanced Materials*.

Zhang, Xuan et al. 2018. “Three-Dimensional High-Entropy Alloy-Polymer Composite Nanolattices That Overcome the Strength-Recoverability Trade-Off.” *Nano Letters* 18(7): 4247–56.

Zhang, Xuan, Andrey Vyatskikh, et al. 2019. “Lightweight, Flaw-Tolerant, and Ultrastrong Nanoarchitected Carbon.” *Proceedings of the National Academy of Sciences of the United States of America* 116(14): 6665–72.

Zhang, Xuan, Lei Zhong, et al. 2019. “Theoretical Strength and Rubber-like Behaviour in Micro-Sized Pyrolytic Carbon.” *Nature Nanotechnology*.

Zheng, Xiaoyu et al. 2014. “Ultralight, Ultrastiff Mechanical Metamaterials.” *Science* 344(6190): 1373–77.

———. 2016. “Multiscale Metallic Metamaterials.” *Nature Materials* 15(10): 1100–1106.

Zhu, Cheng et al. 2015. “Highly Compressible 3D Periodic Graphene Aerogel Microlattices.” *Nature Communications*.

Zigoneanu, Lucian, Bogdan Ioan Popa, and Steven A. Cummer. 2014. “Three-Dimensional Broadband Omnidirectional Acoustic Ground Cloak.” *Nature Materials*.

PUBLICATIONS

1. Deng, B. and Cheng, G. J. Pulsed Laser Modulated Shock Transition from Liquid Metal Nanoparticles to Mechanically and Thermally Robust Solid-Liquid Patterns. *Advanced Materials* **2019**, 31, 1807811.
2. Deng, B.; Xu, R.; Wang, X.; An, L.; Zhao, K. and Cheng, G. J. Roll to Roll Manufacturing of Fast Charging, Mechanically Robust 0D/2D Nanolayered Si-Graphene Anode with Well-Interfaced and Defect Engineered Structures. *Energy Storage Materials* **2019**, https://doi.org/10.1016/j.ensm.2019.07.019.
3. Deng, B.; Xu, R.; Zhao, K.; Lu, Y.; Ganguli, S. and Cheng, G. J. Composite Bending-Dominated Hollow Nanolattices: A Stiff, Cyclable Mechanical Metamaterial. *Materials Today* **2018**, 21, 467-474.
4. Deng, B.; Bruzzaniti, A. and Cheng, G. J. Enhancement of Osteoblast Activity on Nanostructured NiTi/Hydroxyapatite Coatings on Additive Manufactured NiTi Metal Implants by Nanosecond Pulsed Laser Sintering. *International Journal of Nanomedicine* **2018**, 13, 8217-8230.
5. Xu, X.; Zhang, Q.; Hao, M.; Hu, Y.; Lin, Z.; Peng, L.; Wang, T.; Ren, X.; Wang, C.; Zhao, Z.; Wan, C.; Fei, H.; Wang, L.; Zhu, J.; Sun, H.; Chen, W.; Du, T.; Deng, B.; Cheng, G.J.; Shakir, I.; Dames, C.; Fisher, T.S.; Zhang, X.; Li, H.; Huang, Y. and Duan, X. Double-Negative-Index Ceramic Aerogels for Thermal Superinsulation. *Science* **2018**, 363,723-727.
6. Qiu, G.; Nian, Q.; Motlag, M.; Jin, S.; Deng, B.; Deng, Y.; Charnas, A. R.; Ye, P. D. and Cheng, G. J. Ultrafast Laser-Shock-Induced Confined Metaphase Transformation for Direct Writing of Black Phosphorus Thin Films. *Advanced Materials* **2018**, 30, 1704405.
7. Liu, S.; Yuen, M. C.; White, E. L.; Boley, J. W.; Deng, B.; Cheng, G. J.; Kramer-Bottiglio, R. Laser Sintering of Liquid Metal Nanoparticles for Scalable Manufacturing of Soft and Flexible Electronics. *ACS Applied Materials & Interfaces* **2018**, 10, 28232-28241.
8. Hu, Y.; Zhang, F.; Titze, M.; Deng, B.; Li, H. and Cheng, G. J. Straining Effects in MoS_2 Monolayer on Nanostructured Substrates: Temperature-Dependent Photoluminescence and Exciton Dynamics. *Nanoscale* **2018**, 10, 5717-5724.
9. Nian, Q.; Gao, L.; Hu, Y.; Deng, B.; Tang, J. and Cheng, G. J. Graphene/PbS-Quantum Dots/Graphene Sandwich Structures Enabled by Laser Shock Imprinting for High Performance Photodetectors**.** *ACS Applied Materials & Interfaces* **2017**, 9, 44715-44723.
10. Zhang, Q.; Lin, D.; Deng, B.; Xu, X.; Nian, Q.; Jin, S.; Leedy, K. D.; Li, H. and Cheng, G. J. Flyweight, Superelastic, Electrically Conductive, and Flame-Retardant 3D Multi-Nanolayer Graphene/Ceramic Metamaterial. *Advanced Materials* **2017**, 29, 1605506.
11. Martinez, D. A.; Gutierrez, L.; Cai, C.; Deng, B.; Ye, C.; Zhang, M. Y.; Cheng, H.; Ni, H. and Cheng, G. J. In Vitro Osteoblast Gene Expression and Differentiation Atop of Titanium Blocks Laser Coated with Multilayer Biphasic Calcium Phosphate/Titanium Nanocomposites. *Biomedical Physics & Engineering Express* **2017**, 3, 025022.
12. Nian, Q.; Saei, M.; Hu, Y.; Deng, B.; Jin, S. and Cheng, G. J. Additive Roll Printing Activated Cold Welding of 2D Crystals and 1D Nanowires Layers for Flexible Transparent Conductor and Planer Energy Storage. *Extreme Mechanics Letters* **2016**, 9, 531-545.

13. Jin, S.; Ziabari, A.; Koh, Y. R.; Saei, M.; Wang, X.; Deng, B.; Hu, Y.; Bahk, J.-H.; Shakouri, A. and Cheng, G. J. Enhanced Thermoelectric Performance of P-type $Bi_xSb_{2-x}Te_3$ Nanowires with Pulsed Laser Assisted Electrochemical Deposition. *Extreme Mechanics Letters* **2016**, 9, 386-396.
14. Hu, Y.; Li, J.; Tian, J.; Xuan, Y.; Deng, B.; McNear, K. L.; Lim, D. G.; Chen, Y.; Yang, C. and Cheng, G. J. Parallel Nanoshaping of Brittle Semiconductor Nanowires for Strained Electronics. *Nano letters* **2016**, 16, 7536-7544.
15. Hu, Y.; Kumar, P.; Xuan, Y.; Deng, B.; Qi, M. and Cheng, G. J. Controlled and Stabilized Light–Matter Interaction in Graphene: Plasmonic Film with Large-Scale 10-nm Lithography. *Advanced Optical Materials* **2016**, 4, 1811-1823.
16. Hu, Y.; Xuan, Y.; Wang, X.; Deng, B.; Saei, M.; Jin, S.; Irudayaraj, J. and Cheng, G. J. Superplastic Formation of Metal Nanostructure Arrays with Ultrafine Gaps. *Advanced Materials* **2016**, 28, 9152-9162.
17. Nian, Q.; Saei, M.; Xu, Y.; Sabyasachi, G.; Deng, B.; Chen, Y. P. and Cheng, G. J. Crystalline Nanojoining Silver Nanowire Percolated Networks on Flexible Substrate. *ACS Nano* **2015**, 9, 10018-10031.
18. Liu, Z.; Deng, B.; Cheng, G. J.; Deng, H. and Mukherjee, P. P. Mesoscale Elucidation of Laser-Assisted Chemical Deposition of Sn Nanostructured Electrodes. *Journal of Applied Physics* **2015**, 117, 214301.
19. Lin, D.; Nian, Q.; Deng, B.; Jin, S.; Hu, Y.; Wang, W. and Cheng, G. J. Three-Dimensional Printing of Complex Structures: Man Made or toward Nature? *ACS Nano* **2014**, 8, 9710-9715.
20. Liu, Z.; Cao, Z.; Deng, B.; Wang, Y.; Shao, J.; Kumar, P.; Liu, C. R.; Wei, B. and Cheng, G. J. Ultrafast and Scalable Laser Liquid Synthesis of Tin Oxide Nanotubes and Its Application in Lithium Ion Batteries. *Nanoscale* **2014**, 6, 5853-5858.
21. Lin, D.; Deng, B.; Sassman, S. A.; Hu, Y.; Suslov, S. and Cheng, G. J. Magnetic Field Assisted Growth of Highly Dense α-Fe_2O_3 Single Crystal Nanosheets and Their Application in Water Treatment. *RSC Advances* **2014**, 4, 18621-18626.